

DESIGN AND PHYSICO-CHEMICAL
CHARACTERIZATION OF NANOWIRES
AND MULTICOMPONENT METAL
OXIDE FILMS WITH TAILORED MESO-
STRUCTURE AND CRYSTALLINITY

DISSERTATION

Zur Erlangung des akademischen Grades

„doctor rerum naturalium“

- Dr. rer. nat. -

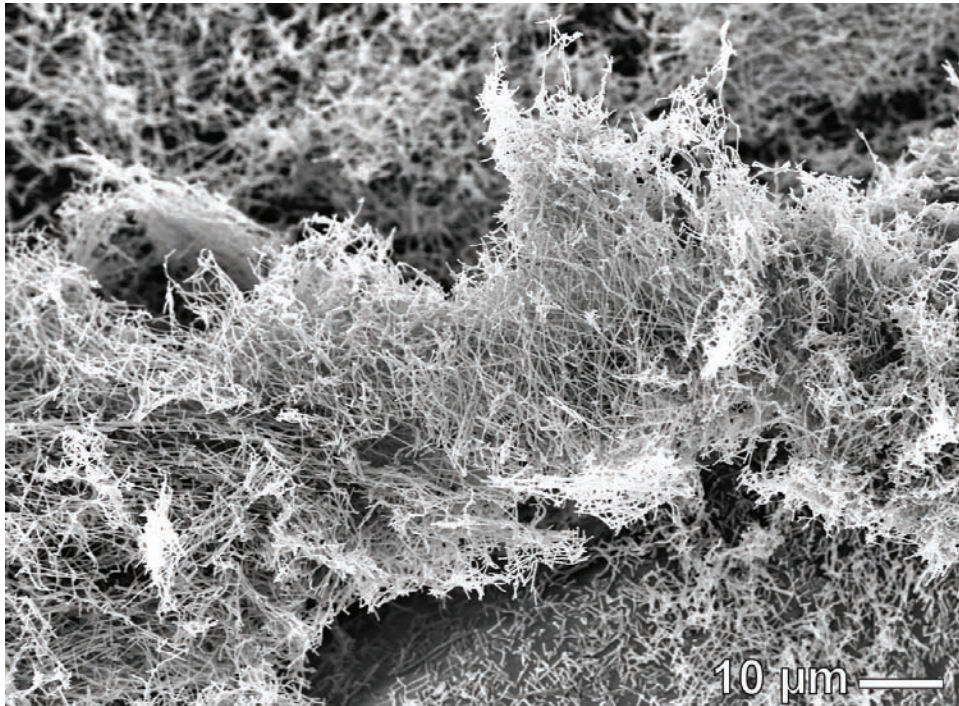
Im Fachbereich Biologie und Chemie

der Justus-Liebig-Universität Gießen

von

M.Sc. Rainer Ostermann

Gießen, im November 2010



"Nanowaves": SEM image of a mat of RuO₂ nanotubes

“Brick walls are there for a reason. The brick walls are not there to keep us out. The brick walls are there to show how badly we want something. Because the brick walls are there to stop the people who don't want something badly enough. They are there to keep out the *other* people.”

Randy Pausch, *The Last Lecture*



Dean / Dekan

Reviewer / Gutachter Prof. Dr. Bernd Michael Smarsly

Reviewer / Gutachter Prof. Dr. Herbert Over

submitted / eingereicht:

The present thesis was prepared in the period of 1.8.2007 – 30.6.2010 at the Institute of Physical Chemistry of Justus-Liebig-University Giessen under the supervision and guidance of Prof. Dr. Bernd Michael Smarsly.

I declare:

The present thesis was prepared by myself and without illicit help from others. Any citations being included literally or by adaptation from the literature or personal communications, have been marked appropriately. The principles of best practice in academia, as documented in the respective charter of the Justus-Liebig-University have been applied in all investigations constituting this thesis.

Die vorliegende Arbeit wurden in der Zeit vom 1.8.2007 – 30.6.2010 am Physikalisch-Chemischen Institut der Justus-Liebig-Universität Gießen bei Prof. Dr. Bernd Michael Smarsly durchgeführt.

Ich erkläre:

Ich habe die vorgelegte Dissertation selbständig und ohne unerlaubte fremde Hilfe und nur mit den Hilfen angefertigt, die ich in der Dissertation angegeben habe. Alle Textstellen, die wörtlich oder sinngemäß aus veröffentlichten Schriften entnommen sind, und alle Angaben, die auf mündlichen Auskünften beruhen, sind als solche kenntlich gemacht. Bei den von mir durchgeführten und in der Dissertation erwähnten Untersuchungen habe ich die Grundsätze guter wissenschaftlicher Praxis eingehalten, wie sie in der „Satzung der Justus-Liebig-Universität Gießen zur Sicherung guter wissenschaftlicher Praxis“ niedergelegt sind.

Abstract¹

Nanostructured metal oxides and metals are already of significant importance for diverse applications, e.g. in catalysis or as electrode materials. Yet in many cases more progress could be achieved by combining the materials' properties with a more suitable morphology than the commonly used thin films or nanopowders.

During my PhD I used electrospinning as a versatile approach to generate nanofibers of metals and metal oxides with the ultimate goal of creating multi-component materials, such as oxide electrodes with nanofibrous conduction paths.

As main challenges, several useful oxides (e.g. RuO₂, transparent conducting oxides) and MOFs (metal organic frameworks) had not been available as nanofibers and if any, there were only a few complicated methods to control the fiber's morphology.

In addition to preparing novel compact fibers, I studied the mechanisms of fiber formation and could thus develop new and straight-forward approaches to synthesize porous and hollow nanofibers with increased surface areas.

Moreover, I demonstrated the first examples of using fiber mats of metal oxides and metals to prepare model catalysts and highly efficient porous electrodes for sensors or fuel cells. I further integrated these electrodes into multi-component coatings for application in solar cells or in transparent conducting polymer films.

¹ Short version, see Chapter 5 for a detailed summary.

TABLE OF CONTENTS

1.	INTRODUCTION	1
1.1	MOTIVATION	1
1.2	ONE-DIMENSIONAL NANOSTRUCTURES	3
1.3	ELECTROSPINNING	5
1.4	ELECTROSPINNING OXIDE SYSTEMS	9
2.	CONDUCTING NANOFIBERS	10
2.1	CONCEPT OF POROUS ELECTRODES	10
2.2	ITO NANOWIRES.....	13
2.3	EXCURSION: INDIUM AVAILABILITY	17
2.4	COMPARISON OF ITO TO OTHER TCO MATERIALS.....	18
2.5	ELECTROSPINNING PREFORMED ATO NANOPARTICLES	20
2.6	ELECTRODEPOSITION ON ATO FIBER MATS	23
2.7	CONCLUSION FOR THE ATO-DSSC	27
2.8	TRANSPARENT CONDUCTING POLYMER FILMS	28
2.9	METAL NANOWIRES.....	31
2.10	APPLICATIONS OF METAL NANOFIBERS	34
3.	POROUS NANOFIBERS	37
3.1	CONCEPT OF POROUS NANOFIBERS.....	37
3.2	PHASE SEPARATION VS. SOLIDIFICATION.....	40
3.3	NANOPARTICULAR FIBERS	42
3.4	INFLUENCE OF NANOPARTICLE SIZE	44
3.5	UV SYNTHESIS, PHOTOCATALYSIS AND TiO ₂ (B).....	49
3.6	CATALYTIC THREE-COMPONENT SYSTEMS TiO ₂ :RU AND Pd	53
3.7	HYBRID MOF FIBERS	56
4.	NOVEL SOL-GEL NANOFIBERS	64
4.1	THE PURPOSE OF SOL-GEL NANOFIBERS	64
4.2	ELECTROSPUN RuO ₂ FOR HETEROGENEOUS MODEL CATALYSIS	65
4.3	HOLLOW NANOTUBES	69
4.4	EXTENSION TO OTHER OXIDES AND FIRST MECHANISTIC INSIGHTS	73
4.5	RELEVANT LITERATURE AND PROPOSED MECHANISM	76
4.6	CRYSTAL PHASE CONTROL IN TiO ₂ :Ru NANOFIBERS	81

5.	SUMMARY AND CONCLUSION	85
5.1	SUMMARY.....	85
5.2	OUTLOOK.....	87
6.	APPENDICES	88
6.1	EXPERIMENTAL DETAILS	88
6.1.1	<i>Chemicals</i>	88
6.1.2	<i>Characterization techniques.....</i>	90
6.1.3	<i>Electrospinning setup</i>	93
6.1.4	<i>ITO nanofibers</i>	94
6.1.5	<i>ATO nanoparticle synthesis and ATO nanofibers</i>	95
6.1.6	<i>FTO, AZO and IZO nanofibers</i>	96
6.1.7	<i>Spray pyrolysis of ATO and FTO.....</i>	98
6.1.8	<i>Comparison of the TCO materials</i>	99
6.1.9	<i>Pt and Pd nanofibers</i>	101
6.1.10	<i>Electrodeposition of Prussian Blue and TiO₂.....</i>	102
6.1.11	<i>TiO₂ nanoparticle synthesis.....</i>	103
6.1.12	<i>TiO₂ nanofibers</i>	104
6.1.13	<i>UV treatment of TiO₂ nanofibers</i>	104
6.1.14	<i>TiO₂(B) nanoparticles and nanofibers</i>	105
6.1.15	<i>SiO₂ nanofibers.....</i>	106
6.1.16	<i>ZIF-8 nanoparticles and nanofibers</i>	108
6.1.17	<i>RuO₂ nanotubes and Ru_xTi_{1-x}O₂ nanofibers</i>	110
6.1.18	<i>Fe₂O₃ nanofibers and nanotubes</i>	111
6.1.19	<i>NiO and Co₂O₃ nanotubes.....</i>	112
6.2	ABBREVIATIONS AND GLOSSARY	113
6.3	REFERENCES	114
6.4	TABLE OF FIGURES.....	125
6.5	TABLES	130
6.6	INDEX.....	131
6.7	ACKNOWLEDGEMENTS.....	133
6.8	CURRICULUM VITAE	134
6.9	LIST OF PUBLICATIONS	138

Chapter 1 – Introduction

1.1 Motivation

“There’s plenty of room at the bottom” was the title of a lecture in which Richard Feynman envisioned and discussed the ramifications of manipulating matter on the atomic level [1]. This theoretical lecture held on December 29th, 1959, is often considered to be the inception of nanotechnology. By definition the size of nanomaterials is below 100 nanometers in at least one dimension. Thereby the realm of these materials ranges from thin films over nanowires to nanoparticles.

Although such materials occur in nature and have been produced synthetically for many years, the techniques of fabrication and characterization have only recently progressed to a point that invites scientists from various backgrounds to work within the interdisciplinary field of nanotechnology. Combining the latest advances from microelectronics, microscopy, colloidal and supramolecular chemistry and ultimately biology, offers an unprecedented opportunity to understand and manipulate the world just beyond the atomic and molecular level.

The properties of nanomaterials have been found to differ significantly from their bulk counterparts, as surfaces and interfaces become more and more important with decreasing size of the

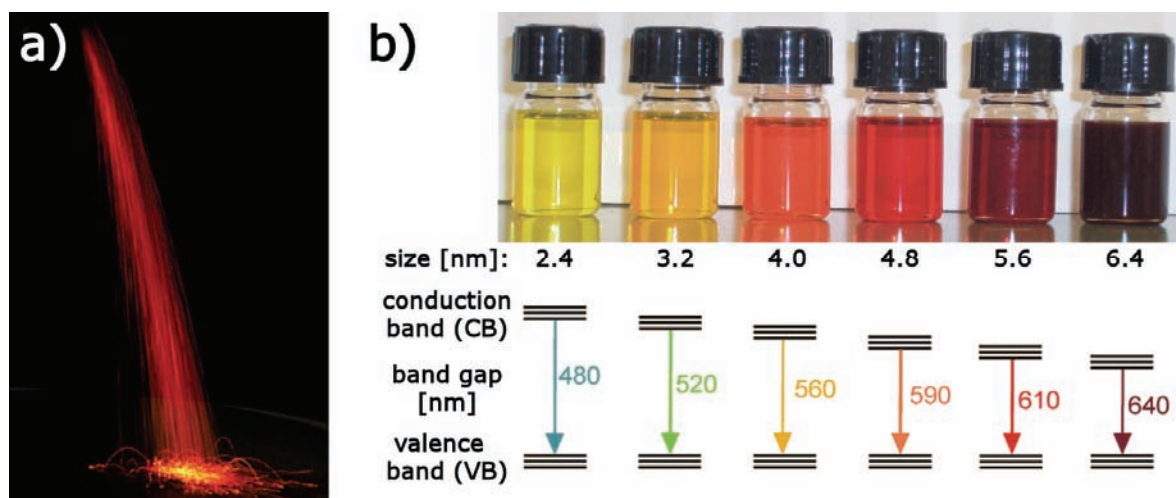


Figure 1-1: Examples of the size-dependent properties of nanomaterials [2]:
 a) Spontaneous combustion of nanometric, pyrophoric iron in air
 b) CdSe quantum dots: The particle size determines the band gap between valence and conduction bands and thereby the color

material, until finally even the electronic structure is affected. An increase in surface area leads to a higher chemical reactivity, such that finely powdered metal ignites spontaneously as shown in Figure 1-1 a) for sub-micrometric iron produced from FeC_2O_4 .

Another example can be found in semi-conductors like CdSe whose band gap is inversely proportional to the size of these so-called quantum dots [2].

In addition to showing size-induced phenomena, different nanomaterials can be combined to design more complex architectures with characteristics surpassing their individual properties².

The curiosity to find and characterize these synergies is the motivation for this work that will focus on nanowires and nanofibers³ as one building block for nanoscale architectures and will seek to integrate the fibers into those architectures.

² Although synthetic examples of useful complex architectures are still rare, many systems in biology, such as enzymes, viruses and even cells, are built from nanoscale components and the assembly clearly surpasses the functionality of its constituents. In fact, a living cell – as the building block of life - would be impossible without its nanoscale architectures of proteins, phospholipids, DNA and RNA.

³ In the following, nanowires and nanofibers will be used synonymously.

1.2 One-Dimensional Nanostructures

Compared to isotropic nanoparticles and two-dimensional thin films, one-dimensional nanostructures such as nanofibers and nanowires are much more anisotropic, i.e. the aspect ratio of length to diameter can attain very high values.

This anisotropy leads to interesting morphologies and properties, such as an extremely low packing density in mats and fabrics of tortuous fibers. Obviously, this system possesses a very low resistance to fluid flow that can be adjusted by the packing density of the fibers (see Figure 1-2). Additionally, the diameter of the fibers and filaments can be varied from millimeter to nanometer scale to further adjust the porosity of the resulting mats that are very suitable for filtration applications. By using nanofibers the separation range can be extended to ultra- and nanofiltration, allowing to filter out nanometric objects like viruses [3].

Although less obvious in filtration, the mechanical properties of fiber mats are also quite unique, combining the high strength in the axial direction of each fiber with the overall flexibility of the mats. In fact, nanofibers are widely used for composite fiber reinforcements [4], e.g. carbon fibers in epoxy resins, but also electrospun nanofibers significantly improve the mechanical properties as well. For instance, the addition of 4 wt% of nylon nanofibers to an epoxy resin increases the Young's modulus from 2.5 to 91 MPa [5].

In addition to improved mechanical properties, nanocomposites of nanofibers can also offer interesting electrical properties. In order to obtain electrical conductivity in a nanocomposite consisting of conducting and nonconducting phases, a certain volume fraction of the conducting phase must be present to allow the formation of a continuous network. This so-called percolation threshold critically depends on the dimensionality of the conducting phase, i.e. the shape and aspect ratio of its building blocks. For spherical particles up to 30 vol% of the conductor are required to attain percolation and thus conductivity. In contrast, well-distributed,

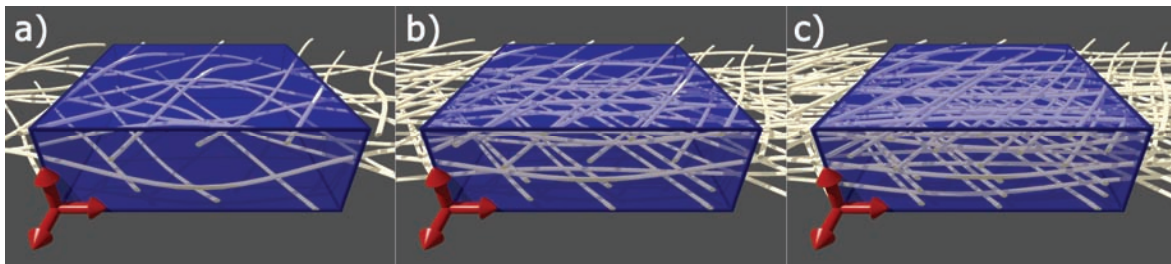


Figure 1-2: Packing density of curled fibers as a function of their tortuosity: The fibers are curled with a certain amplitude in the y direction, decreasing this amplitude (from a to c) results in more densely packed fiber mats (the blue box contains a constant volume).

long nanowires with a high aspect ratio can reduce the percolation threshold to well below 1 vol%. For example, the percolation threshold was found to be as low as $2.3 \cdot 10^{-3}$ wt% for carbon nanotubes (CNT) highly dispersed in epoxy resin, whereas entangled carbon nanotubes or carbon black required much higher filler content to allow electrical conductivity (see Figure 1-3) [6].

In summary, one-dimensional nanostructures are currently of great interest and there has been extensive research into various “top-down” and “bottom-up” methods to create these nanostructures. In the next section electrospinning will be introduced as versatile technique to synthesize nanofibers of various materials.

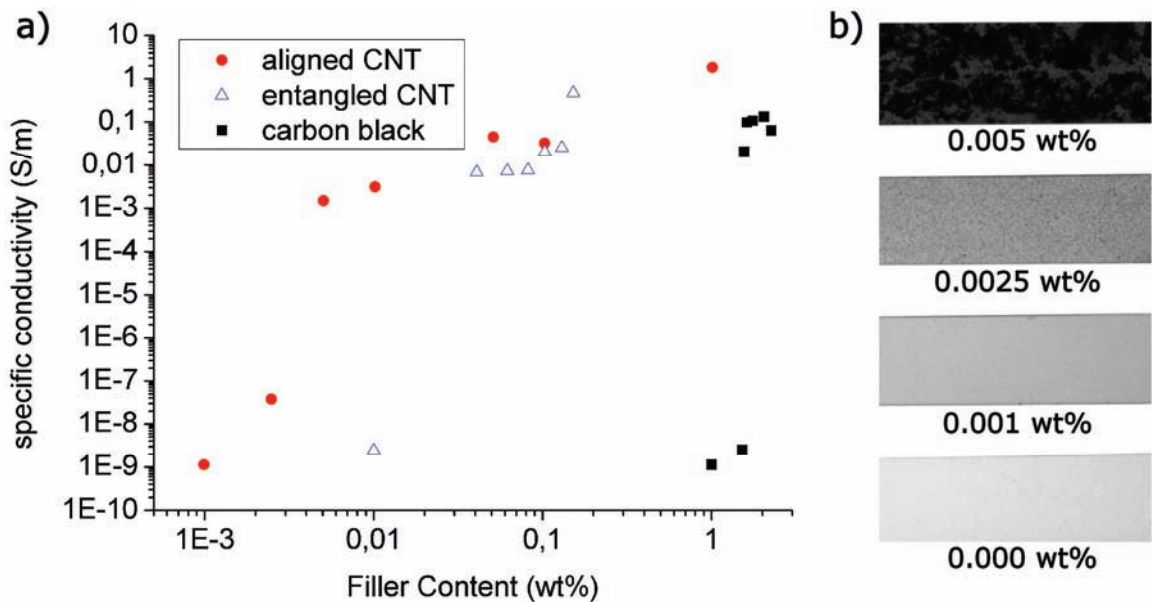


Figure 1-3: a) Electrical conductivity of epoxy composites with aligned or entangled carbon nanotubes or carbon black as conducting filler
b) Digital images of aligned CNT-epoxy composites with different loadings of carbon nanotubes (CNT) (adapted from [6])

1.3 Electrospinning

The origins of electrospinning date back to patents issued to J. Cooley [7] and A. Formhals [8], [9] in 1899 and 1929, respectively. In the 1960s Taylor provided a theoretical background [10], but it was not until the 1990s that electrospinning finally received broader attention of the scientific community through the work of D. Reneker and A. Yarin [11]. Since 2000 the groups of Y. Xia [12], J. Wendorff and A. Greiner [3] contributed significantly to the further development of the technique.

Electrostatic spinning, commonly called electrospinning, is a facile method that can create large quantities of nanofibers. As a top-down method, electrospinning is dependent on the viscoelastic properties of a solution or melt and not on chemical reactivity, thereby allowing to generate nanofibers from a wide variety of materials.

The principle of electrospinning is illustrated in Figure 1-4:

A viscous fluid is pumped through an orifice and an electric field is applied between this spinning tip and a ground target. Beyond a certain applied potential, the surface tension of the fluid is overcome and an electrified jet is ejected from the spinning tip forming the so-called Taylor cone.[13]

As the jet is accelerated towards the target, the fluid's viscosity increases and the charges move

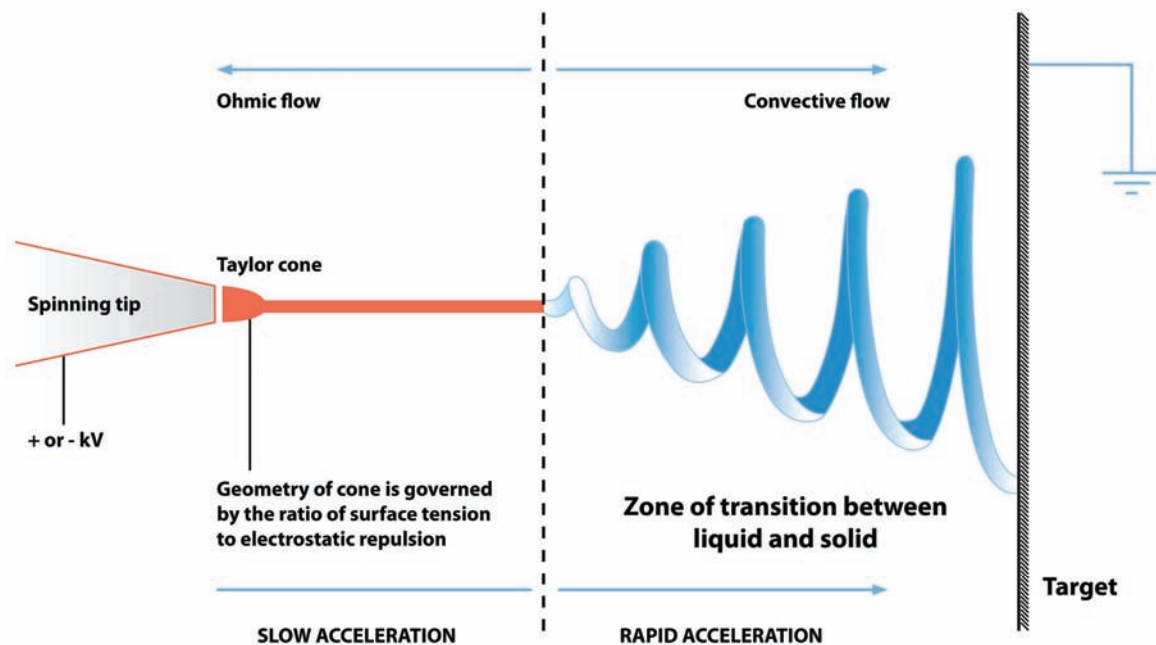


Figure 1-4: The formation of nanofibers via the electrospinning process [13]

to the surface of the jet. In case of a polymeric solution the solvent evaporates, whereas for a polymer melt the temperature decreases. However, as charges build up on the surface of the emerging fiber, a slight perturbation can displace a segment of the fiber that then experiences repulsive electrostatic forces from the up- and downward parts of the fiber.

As depicted in Figure 1-5 the resultant force points away from the fiber's axis and leads to the so-called bending instability [11]. This additional stretching force is the major contribution to the elongation of the fiber and thereby significantly reduces its diameter. In fact, several generations of bending instabilities can develop before the fiber solidifies completely, whereby a diameter of a few nanometers can be attained.

In summary, Coulomb forces are used to generate and elongate nanofibers, making the principle of electrospinning rather straightforward. However, the spinning process and its details are much more complicated and governed by many parameters, such as the fluid's viscosity and conductivity, the feed rate and the applied electric potential, the distance between the spinning tip and the collector.

Solution's properties

For electrospinning of polymeric solutions, the concentration and the molecular weight of the polymer are of great importance, as the solution's viscosity is mainly due to the entanglement of polymer chains. Without a sufficient viscosity, the electrified jet would break up and electro-spraying would be observed instead of electrospinning.

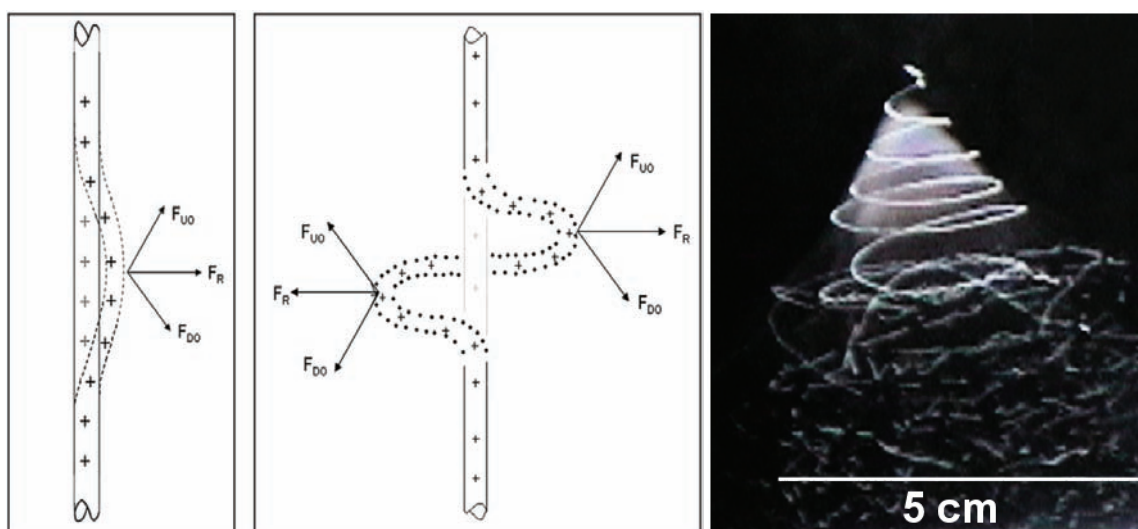


Figure 1-5: Scheme of a bending instability leading to thinning and elongation of the nanofiber and a stroboscopic picture showing several generations of bending instabilities that develop during the electrospinning process [11]

In general, a higher concentration or a higher molecular weight of the polymer results in a thicker diameter of the fibers [14].

Similarly, a more volatile solvent leads to faster solidification and thicker diameters. In general, the volatility must be a compromise between allowing a timely solidification of the fiber before the jet reaches the collector and the clogging of the needle when the Taylor cone solidifies. Moreover, the solvent should be a good solvent for the polymer and all additives, and the surface tension and conductivity should not be too high, as a high conductivity can lead to short-circuits between the tip and the collector.

If the surface tension and conductivity of the solution are too high, beaded fibers might result, in particular if the solution's viscosity is low [15]. However, especially surfactants can always be added to lower the surface tension and improve the homogeneity of the fibers.

Process parameters

Stable electrospinning occurs when the feed rate matches the rate of fiber production and the applied electric field exerts a force that can overcome the surface tension of the spinning solution, but is balanced by its viscosity.

The detailed influence of the spinning parameters is quite complex, although it is generally accepted that higher feed rates lead to thicker fibers and a higher electric field is assumed to have the opposite effect.

Higher temperatures accelerate the drying of the electrospinning jet and result in thicker fibers, whereas solvent vapor in the atmosphere can delay the solidification. The relative humidity is

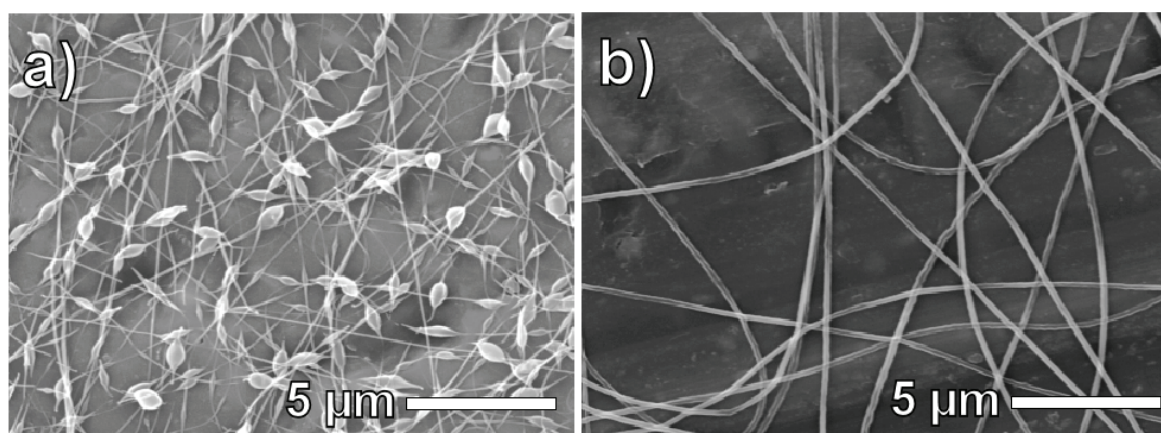


Figure 1-6: Scanning electron microscope (SEM) image of beaded and smooth nanofibers of PEO (polyethylene oxide) electrospun from aqueous solutions of low charge density and a) low (2 wt% PEO) and b) high (4 wt% PEO) viscosity [15]

especially important for water soluble polymers that cannot be spun beyond a certain humidity, as the jet does not solidify and the wet fibers coalesce on the collector.

The humidity and spinning solvents play an important role in determining the surface morphology of the fibers, as inclusion of non-solvents for the polymer into the emerging fibers can create some porosity (see Figure 1-7 a). On the other hand, rapid evaporation of the solvent can result in the formation of a solid skin on the spinning jet, with the following collapse of such partially hollow tubes leading to flat ribbons (see Figure 1-7 b) [16]. Note that the diameter of these ribbons is typically several micrometers, in contrast to the hollow nanotubes presented in chapter 4.

In addition to the aspects relevant for this thesis, one finds several further contributions in the literature that have elucidated the fundamentals of electrospinning and demonstrated its potential applications, with excellent reviews providing an overview and the necessary references [3], [11], [12]. The topics therein range from alignment of nanofibers, multi-spinneret systems, moving collector assemblies to coaxial spinning techniques. Many applications have been envisioned and demonstrated, such as nanofiltration, photocatalysis, bone and tissue engineering and drug release.

In the following section, the literature on oxide nanofibers relevant to this thesis will be summarized.

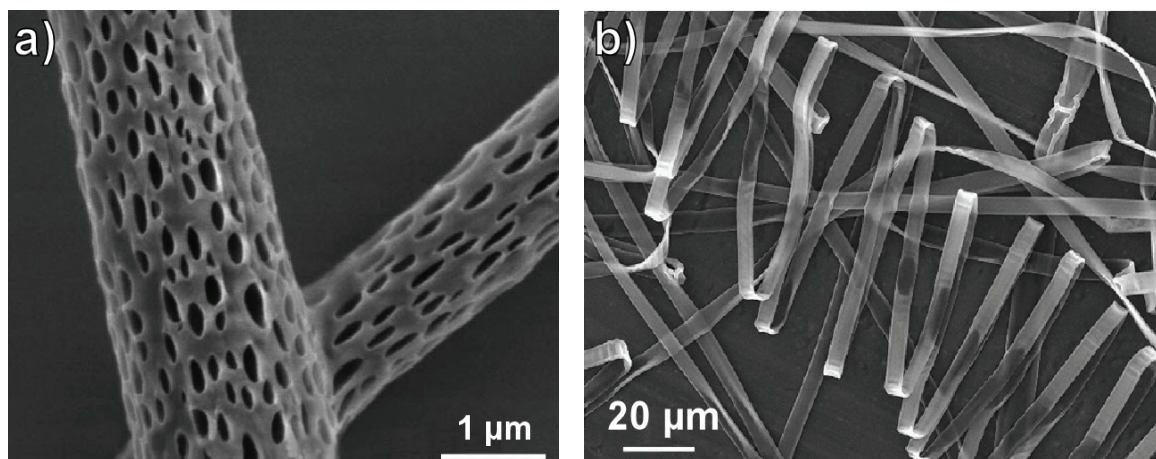


Figure 1-7: a) Porous PLLA nanofibers electrospun from a solvent mixture ($\text{CH}_2\text{Cl}_2/\text{MeOH}$) resulting in polymer-rich and polymer-poor sections [3]

b) Flat ribbons from collapsed hollow electrospinning jets of poly(etherimide) (PEI) spun from hexafluoro-2-propanol [16]

1.4 Electrospinning Oxide Systems

The first oxide nanotubes were obtained by coating sol-gel-derived TiO_2 onto polymeric nanofibers to produce hollow tubes [17]. Soon afterwards it was found that sol-gel derived fibers could easily be produced by addition of the respective precursors to the electrospinning solution. Alkoxides of (transition) metal cations were added to suitable carrier polymer solutions and after electrospinning composite fibers, a thermal treatment removed the polymer and resulted in oxide nanofibers. Starting with TiO_2 [18], many binary metal oxides were electrospun [19] and tested for a range of applications, such as sensing [20], photocatalysis [21], photovoltaics [22], or electrochemistry [23].

The ease of preparation of sol-gel derived nanofibers further led to the preparation of nanofibers of ternary oxides like BaTiO_3 [24] and hierarchical systems like V_2O_5 nanorods on TiO_2 fibers [25].

However, after the focus had long been solely on the synthesis and characterization of nanofibers from various materials, in the past few years the interest has begun to center more on complex systems that should benefit particularly from the fibrous morphology.

Chapter 2 – Conducting Nanofibers

2.1 Concept of Porous Electrodes

TCO (transparent conducting oxide) materials are widely used in optoelectronic applications as transparent electrodes, commonly as thin, compact films deposited on glass or quartz substrates [26], [27]. These TCO layers of 200-300 nm thickness possess sheet resistances typically below $20 \Omega/\square$ and transparencies above 85% in the visible range, making them suitable as two dimensional electrodes for electrochromic devices [28] and solar cells [29].

For ordinary TCO electrodes, typical deposition techniques are CVD and PVD (chemical and physical vapor deposition), including spray pyrolysis, PLD (pulsed laser deposition) and magnetron sputtering, resulting in compact layers [26].

As proposed by Zaban et al. [30] and shown in Figure 2-1, a three-dimensional TCO electrode theoretically offers advantages for electron collection in DSSCs (dye sensitized solar cells), due to a higher electrode surface area and a shorter electron diffusion pathway to the back electrode, limiting recombination losses. The practical realization of such DSSCs with TiO_2 on indium tin oxide (ITO) nanopowders [31] or nanowires generated by laser-ablation [32] showed only low conversion efficiency, probably as a consequence of the low amount of TiO_2 deposited on the porous electrode.

Porous electrodes can also be produced via sol-gel processing with suitable polymer templates, as demonstrated for mesoporous and macroporous ITO [33-35].

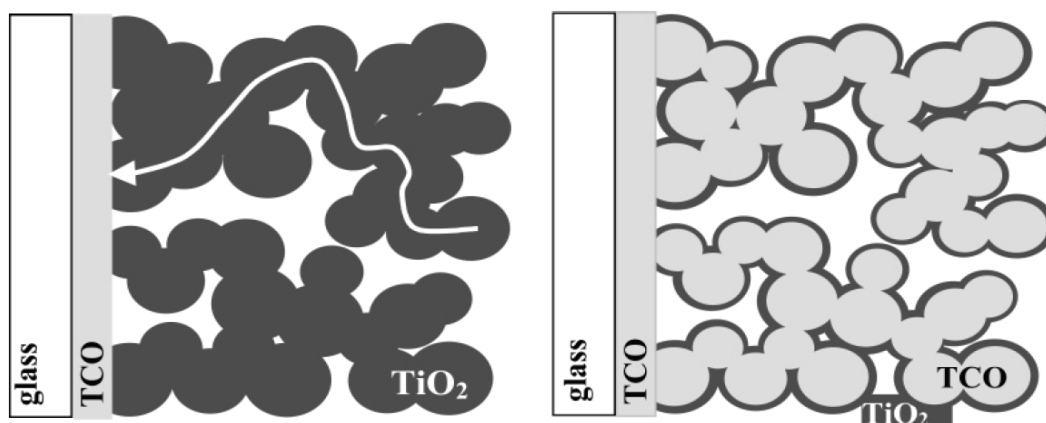


Figure 2-1: Flat and extended current collector for DSSC [5]

While providing a high surface area, such mesoporous TCO films with pore sizes of 5-15 nm have a low overall porosity of only 30-35%. Thereby these films possess high interfacial areas and are only suitable for surface functionalization, especially with a monolayer of redox-active molecules like ferrocene.

To build a solar cell or a rechargeable battery, it is necessary to add more material to the electrode. However, depositing another oxide inside a mesoporous film is not straight-forward, as a blocking of the pores might occur. Macroporous films with a minimum pore size of 0.5-1.5 μm would be more suitable in this respect, but their interfacial area is rather low⁴.

An alternative concept to endow TCOs with porosity is the generation of densely packed nanofibers. The high aspect ratio of the fibers offers conducting pathways and the porosity can be adjusted through the packing density.

Figure 2-2c sketches an optimized electrode with conducting nanowires extending into a porous semi-conducting material. Ideally, the volume fractions of nanowires, semi-conductor and pores are adjusted to optimize the electrode's performance. For comparison a non-porous electrode with high resistance to diffusion and electronic transport is shown (Figure 2-2a). Whereas the porous electrode only lowers the resistance to diffusion (Figure 2-2b), the nanowires also improve the electronic properties, thus clearly enhancing the electrode.

As mentioned above, the experimental realization of a three-dimensional electrode for DSSCs showed only low conversion efficiency, until recently an elaborate approach based on a poly-

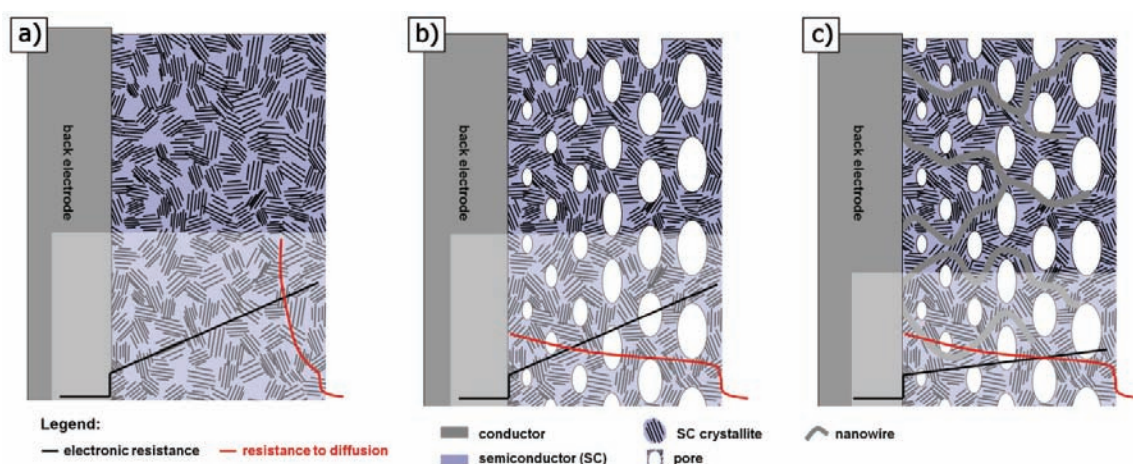


Figure 2-2: Comparison of resistance to electronic transport and diffusion for different electrode geometries: a) compact, b) porous and c) porous with nanowires

⁴ The surface area increases roughly by a factor of π when adding a layer spherical pores to planar surface (i.e. $4\pi r^2$ compared to $4r^2$). However, one macropore with a radius of 1 μm possesses the approximately the same thickness as a stack of 100 layers of mesopores with a radius of 10 nm.

carbonate template for the ITO nanowires was reported with a DSSC efficiency of 4% [36], thus validating Zaban's concept and my approach of using conducting nanowires. One promising method to produce these nanowires is electrospinning and the results will be discussed in the remainder of this chapter, before evaluating the concept of porous electrodes in solar cells and other applications.

2.2 ITO Nanowires

The most straight-forward approach to produce fibrous electrodes is to use ITO nanofibers made from a carrier polymer and sol-gel precursors similar to those used in mesoporous films [33]. However, the commonly used acidic solutions and chloride or nitrate salts led to a high conductivity in the electrospinning solution and thereby to poor spinning behavior.

By using “uncharged” precursors with complexing anions like acetylacetonates this problem could be effectively circumvented, but the recipe needed to be further adapted with acetone as co-solvent for the $\text{In}(\text{acac})_3$. This approach worked well for ITO, as the acetylacetonate was sufficiently reactive during calcination and completely transformed into the oxide⁵.

Another important issue was the shrinkage of 10-15% of the fibers during calcination, as the fiber mat tended to peel off the substrate that did not contract. As can be seen in Figure 2-3, applying a thin film of the carrier polymer via dip-coating effectively reduced this problem, as the polymer melted during calcination and thereby reduced the stress between nanofibers and substrate. The fiber mat was floating on the polymer melt and only interacted with the substrate after the polymer was decomposed.

Figure 2-4 shows the SEM image of nanofibers as a non-woven mat deposited on a silicon wafer. The next step towards the composite electrode was to coat this fiber mat with a thick meso-

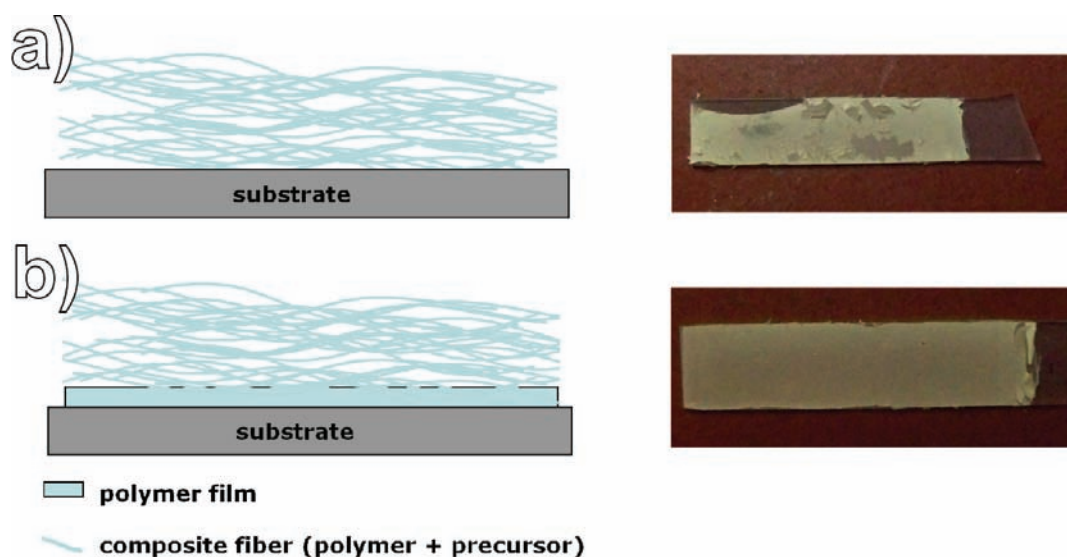


Figure 2-3: Scheme before and digital image after calcination of a) ITO nanofibers directly on the substrate and b) with a thin layer of the carrier polymer to reduce stress during calcination

⁵ As will be shown in chapter 4, many other acetylacetonates tended to sublime, but fortunately a more general approach was found by preparing DMF complexes of the precursor salts.

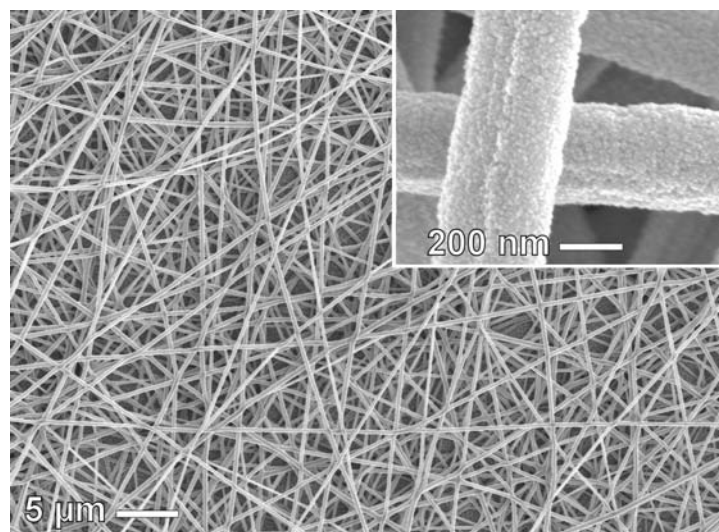


Figure 2-4: SEM image of an ITO nanofiber mat

porous TiO_2 layer. However, the ITO nanofibers dissolved in the acidic sol-gel solutions typically employed for the preparation of mesoporous TiO_2 . Therefore, a nanoparticle-based approach was developed by using preformed TiO_2 nanoparticles with the block-copolymer PIB3000 (poly(isobutylene)-block-poly(ethylene oxide)) as template. After some initial work by myself, this part of the project was further developed by C. Reitz during his bachelor's thesis under my supervision.

These first results are summarized in Figure 2-5 and show that the ITO nanofibers actually did not improve the DSSC's performance. It is apparent from the corresponding SEM image that the nanofibers were not embedded nicely in the porous TiO_2 matrix that still contained many cracks, especially around the fibers. This can be explained by the shrinkage of the TiO_2 film during drying and calcination.

Parameter	DSSC with fibers	DSSC without fibers
J_{sc} [A/cm^2]	$-2,52 \cdot 10^{-3}$	$-3,07 \cdot 10^{-3}$
U_{oc} [V]	0,770	0,808
J_{MPP} [A/cm^2]	$-1,56 \cdot 10^{-3}$	$-1,97 \cdot 10^{-3}$
U_{MPP} [V]	0,530	0,505
FF [%]	42,78	39,67
η [%]	0,83	0,99

Figure 2-5: DSSC performance and SEM image of the first electrode composed of ITO nanofibers and mesoporous TiO_2

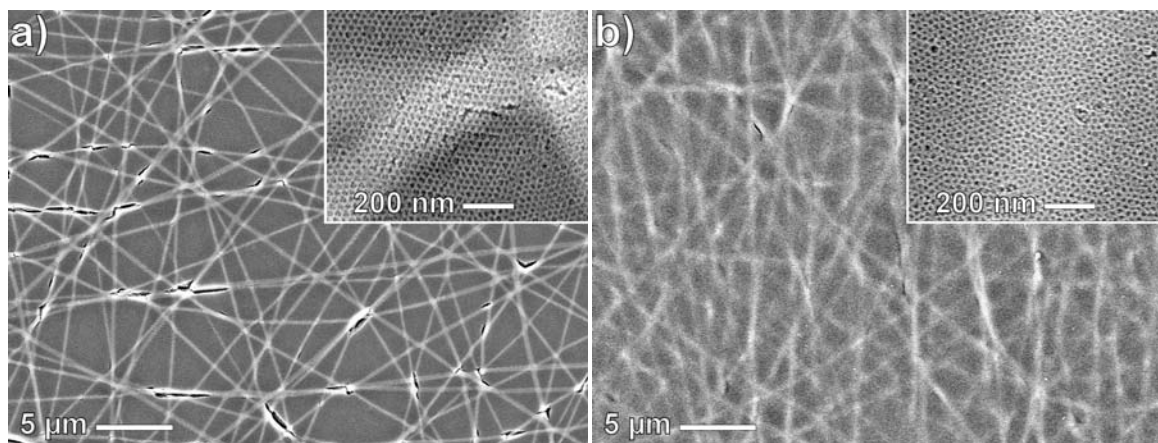


Figure 2-6: SEM image of ITO nanofiber mat coated a) once and b) twice with mesoporous TiO₂ from nanoparticles

After the bachelor's thesis, the preparation of the TiO₂ nanoparticle dispersions could be improved significantly by C. Weidmann. Using nanoparticles prepared according to his procedure, well-organized mesoporous TiO₂ films could be obtained. In order to optimize the electrode, a second layer of mesoporous TiO₂ was applied after stabilizing without template removal at 300°C. As can be seen from the SEM images in Figure 2-6, there were fewer cracks in the first layer and these cracks were closed in the second layer.

Unfortunately, these films were prepared after the bachelor's thesis and the corresponding collaboration⁶.

The possibly improved ITO-TiO₂ system was not tested as electrode in a DSSC, as in the meantime, similar results were published and the ATO system was developed. Furthermore, a closer inspection revealed that the contact between ITO nanofibers and TiO₂ matrix was still poor (see Figure 2-7) and therefore an alternative approach by electrodepositing the TiO₂ was followed.

⁶ Our collaborators from the University of Hannover are attempting to build DSSC electrodes by electrodeposition of ZnO onto our ITO fibers, but so far no substantial improvements of the solar cell performance were observed and therefore those results are not included here.

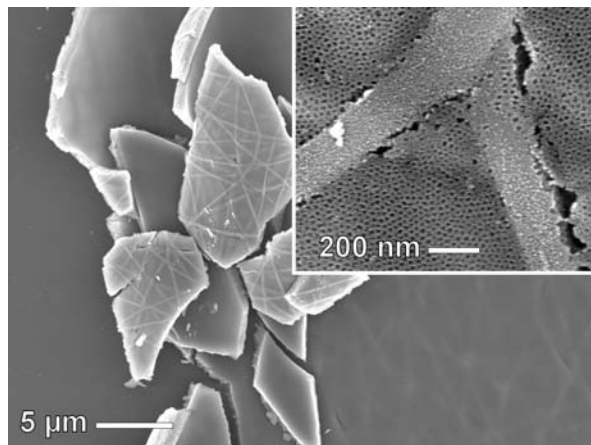


Figure 2-7: SEM image of ITO nanofiber mat coated twice with mesoporous TiO_2 , but scratched off the substrate to reveal the poor contact between ITO fibers and TiO_2 matrix

2.3 Excursion: Indium Availability

The availability of indium is another issue with using ITO as transparent conducting oxide. Historically, ITO was the first TCO material and therefore its processing is quite mature. However, due to the ever-growing demand for indium in transparent electronics and photovoltaics, there have been concerns about the long-term availability of indium, resulting in an increase in price from 60 to over 1000 \$/kg indium (see Figure 2-8). This increase can be understood from the fact that indium is a by-product in tin, lead and copper mining, thus production and availability of indium were determined largely by tin and copper production. At the peak of indium price in 2005, the efficiency of indium extraction was improved and “recycling”⁷ was established leading to a decrease in indium price that further dropped in 2008/09 when new large deposits were reported in Saxony (Germany) and China. Recently, with the beginning of large-scale production of CIGS (Copper Indium Gallium Selenide) solar cells, the price of indium has been increasing again. Therefore it is highly desirable to find suitable low-cost replacements.

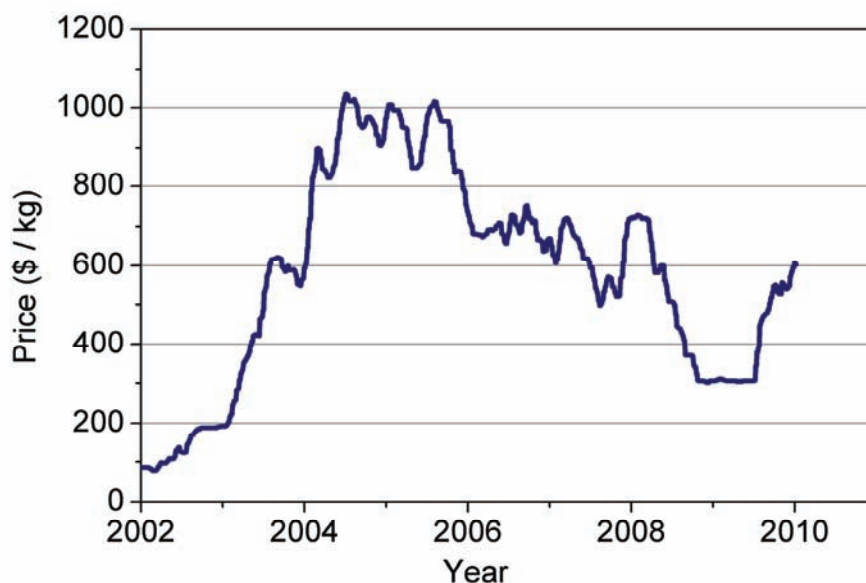


Figure 2-8: Development of the price of indium (99.99% purity, data from London Metal Exchange as of May, 2010)

⁷ In conventional processing of indium for ITO thin films, i.e. sputtering and CVD, only 30% of the material is deposited on the substrate. In most reports, “recycling” therefore refers to the recovery of the remaining indium from the processing equipment.

2.4 Comparison of ITO to Other TCO Materials

ITO is still widely used as TCO material, but alternatives such as ATO or FTO (antimony or fluorine doped tin oxide) and AZO or IZO (aluminum or indium doped zinc oxide) are becoming more and more important. In addition to higher availability and lower prices of the corresponding metals (see Table 2-1), the tin oxide based TCOs also offer better chemical stability making them more suitable for processing in acids and at high temperature⁸.

Table 2-1: Comparison of various TCO materials⁹

Name	Composition	Resistivity $\Omega \cdot \text{cm}$	Transparency	Price* \$/kg
ITO	$\text{In}_2\text{O}_3:\text{Sn}(10\%)$	$7.2 \cdot 10^{-5}$	90-95%	600
AZO	$\text{ZnO}:\text{Al}(2\%)$	$8.5 \cdot 10^{-5}$	85-95%	2
FTO	$\text{SnO}_2:\text{F}(5\%)$	$5.0 \cdot 10^{-4}$	85-90%	15
ATO	$\text{SnO}_2:\text{Sb}(7\%)$	$1.1 \cdot 10^{-3}$	80-85%	15

* Bulk prices as of May, 2010 from London Metal Exchange (purity 99.9%)

As shown in chapter 2.2, mesoporous films or nanofibers of ITO (tin doped indium oxide) can be conveniently prepared by sol-gel methods from molecular precursors, as by thermally annealing the mixture crystallizes as transparent conducting ITO, i.e. a solid solution of tin in indium oxide of the cubic bixbyite structure.

This sol-gel and annealing approach fails for other ternary or doped oxides, i.e. the conductivity is orders of magnitude lower than for films prepared by sputtering or spray pyrolysis¹⁰. The latter are vapor deposition techniques and possess the advantage of rapidly solidifying the TCO material in the desired crystalline and conducting phase on the substrate, whereas solidification and crystallization are rather slow for the sol-gel process. Although a detailed analysis is out of the scope of this project, the loss in conductivity can be explained by the imperfect doping and phase segregation of the formed oxide. In the case of doping with cations the different rates of hydrolysis and condensation and differences in lattice energies prevent the formation of the

⁸ ITO can be easily etched by diluted HCl in presence of Zn metal or HNO_3 [37] and at elevated temperature indium migrates into other metal oxides, e.g. TiO_2 or ZnO in dye-sensitized solar cells[28].

⁹ Data from several sources: [38],[39],[40]

¹⁰ At the beginning of this PhD project, various TCO films (including ITO, ATO, FTO, AZO) were prepared by sol-gel methods and spray pyrolysis according to the literature. While spray pyrolysis always yielded well-conducting (i.e. the conductivity was at most one order of magnitude lower than reported in the literature) and transparent (only AZO films were a little hazy) films, the only well-conducting sol-gel coatings were ITO.

desired solid solution¹¹. Similarly, it is difficult to incorporate anions like F⁻ homogeneously into the solid, as they form volatile HF.

Although it is not possible to generate thin films and nanofibers of most conducting oxides directly via sol-gel methods, there are several works that demonstrated the synthesis of TCO nanoparticles. Especially cation-doped TCO materials can be easily obtained by rapid preparation techniques like precipitation or flame pyrolysis. Therefore, it would be highly desirable to separate the preparation of the TCO materials into two steps:

- Synthesis of nanoparticles with controlled stoichiometry and crystallinity
- Preparation of the final material as thin films or nanofibers

The main challenge in this approach is to obtain a stable dispersion of the nanoparticles that can be further processed. Techniques like flame pyrolysis generate nanocrystalline materials of the desired composition, yet particle agglomeration usually limits the further use of these materials.

By using precipitation methods however, it is possible to obtain redispersible TCO nanoparticles. For example, Goebbert et al. demonstrated the synthesis of ITO and ATO nanoparticles and their application for the preparation of well-conducting thin films [41].

They precipitated ethanolic solutions of the precursor chlorides in concentrated ammonia solutions containing amino acids as stabilizers. The white slurry is transferred into Teflon-lined autoclaves and treated under hydrothermal conditions to obtain crystalline nanoparticles that can be redispersed in aqueous solution.

As the ATO nanoparticles of 4-6 nm are only dispersible above pH=8, the strong base tetramethylammonium hydroxide (TMAH) needs to be added.

The results could be reproduced successfully and the obtained brownish ATO dispersion could be deposited onto glass slides to yield transparent conducting coatings with a resistivity range of $\rho = 10^{-2} - 10^{-1} \Omega \cdot \text{cm}$, a value that is only 1-2 orders of magnitude higher than for coatings prepared by spray pyrolysis. This finding can be explained by the fact that the coatings contain many grain boundaries from the nanoparticles and are in general quite porous, thereby scattering reduces electron mobility and increases resistivity.

¹¹ For a detailed comparison of various TCO materials, see chapter 6.1.8.

2.5 Electrospinning Preformed ATO Nanoparticles

Although the ATO dispersions seem suitable for electrospinning and stable spinning solutions could be prepared with PVP (polyvinylpyrrolidone) as carrier polymer, only poor spinning was possible, as the charge density and conductivity was too high due to the high TMAH content and water as the solvent.

As seen for the ITO nanowires [see chapter 2.2], uncharged precursors or nanoparticles and volatile non-aqueous solvents usually work best.

However, it was observed that shorter hydrothermal treatment resulted in less crystalline nanoparticles that were more readily dispersed with less TMAH. Additionally, Et_2NH (diethylamine) could be used to replace TMAH and obtain yellowish solutions that electrospun well and could be converted into conducting nanofibers by calcination.

The electrospinning process yielded composite polymer-inorganic nanofibers with an average diameter of 400-500 nm as a non-woven mat. Upon calcination the spinning polymer was completely removed and purely inorganic, polycrystalline nanofibers with diameters of 200-300 nm and cassiterite structure were obtained (see Figure 2-9).

A systematic investigation further revealed that the fibers could also be produced from “amorphous” ATO colloids without hydrothermal treatment and that the conductivity of the resulting fibers was actually higher than if crystalline nanoparticles were used. This finding showed that the composition was already fixed during the precipitation step and later hydro-

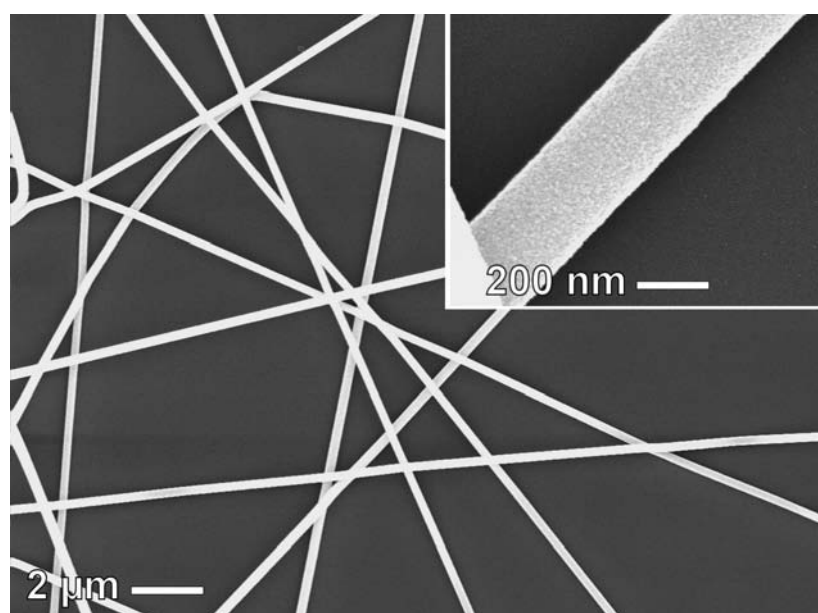
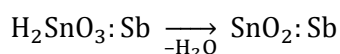


Figure 2-9: SEM image of ATO nanofibers prepared from nanoparticles

thermal or thermal treatment only affected the degree of crystallinity.

XRD (X-Ray Diffraction) analysis further showed that the nanoparticles were already partially crystalline after washing and centrifugation, although the degree of crystallinity could be increased by (hydro)thermal treatment (see Figure 2-10). In fact, the colloidal particles should initially be amorphous after precipitation as antimony-doped “stannic acid”, i.e. a hydrated form of doped tin dioxide that can be converted to doped tin dioxide:



The dehydration and crystallization was accompanied by a change in the dispersion’s color from light yellowish to dark brownish¹². Obviously, it took place during hydrothermal or thermal treatment at high temperature. However, it was also observed that the dehydration slowly occurred even at room temperature or during prolonged centrifugation.

As shown in Table 2-2, fibers from amorphous particles can sinter together more easily and they possess higher conductivities than those fibers from crystalline particles. In general, the nanofibers shrink upon thermal treatment and thereby the resulting fibers become denser. In contrast, the shrinkage of thin films that are stretched on a substrate results in some porosity and ultimately in cracks to compensate for the mechanical stress. As an important extension of the

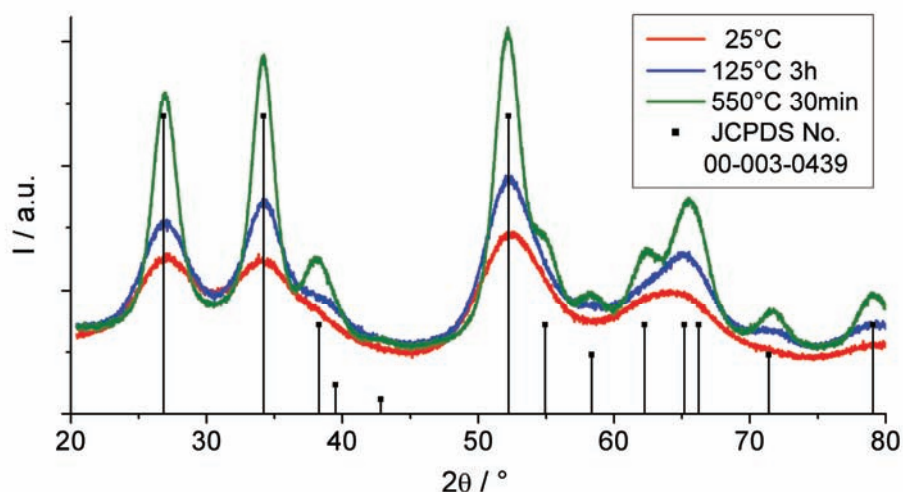


Figure 2-10: XRD of nanoparticles as-prepared (25°C), after hydrothermal treatment (125°C for 3 h) and thermal treatment (550°C for 30 min). With cassiterite (SnO_2) reference pattern from the JCPDS (Joint Committee of Powder Diffraction Standards) database.

¹² Actually, not only the slurry, but also the clear nanoparticle dispersion turned crystalline, i.e. from yellow to brownish, upon solvothermal treatment. After calcination the color of ATO is dark blue.

results from Goebbert et al. for thin films, it could be demonstrated that the use of amorphous particles always leads to higher conductivity in both films and fibers, as the amorphous particles could sinter together more easily.

The fact that fully crystalline particles can produce porous fibers will be exploited in chapter 3.

Table 2-2: Influence of particle crystallinity on conductivity of fibers and films

Preparation of particles [§]	Type	Resistance [#] k Ω /cm	Resistivity* $\Omega \cdot \text{cm}$
25°C	Fiber mat	2-3	
125°C 3 h	Fiber mat	8-10	
150°C 3 h	Fiber mat	13-16	
25°C	Thin film		$2.5 \cdot 10^{-2}$
125°C 3 h	Thin film		$1.1 \cdot 10^{-1}$

[§] that is followed by calcination at 550°C

[#] see text for details

* evaluated for films with a thickness of 180 nm on glass slides

A literature review showed that the amino acid was not essential, as tin dioxide colloidal nanoparticles are intrinsically stable above pH = 9 due to their zeta potential [42]. Moreover, the addition of erbium was reported to increase the conductivity of thin films [43], but a significant effect was not found in the fibers.

Single fibers possessed a resistivity below 1 $\text{Ohm} \cdot \text{cm}^{13}$. More relevant is the bulk resistance of the fiber mats, as it determines the usefulness as an electrode. The resistance of a fiber mat was evaluated macroscopically by 2-point measurements on glass substrates to be about 2-3 k Ω /cm for a thickness of approximately 1.5 μm .

The optimized recipe yielded nanofiber mats that were free-standing and could be deposited on glass or TCO-coated glass substrates to serve as electrodes. The packing density could be adjusted by (hot) pressing or applying a drop of non-solvent¹⁴ to contract the fiber mats by capillary action. Thereby, fiber mats with a macroscopic resistance of 500 Ω /cm and below could be obtained.

¹³ Measured in collaboration with BASF SE.

¹⁴ For example, hexane or cyclohexane.

2.6 Electrodeposition on ATO Fiber Mats¹⁵

The nanofibers with diameters of 200-300 nm showed sufficiently low bulk resistances ($\sim 1\text{-}5\text{ k}\Omega/\text{cm}$) to be used as 3D electrodes for the electrodeposition of electrochromic Prussian Blue (iron hexacyanoferrate, see Figure 2-11) and various metal oxides (Fe_2O_3 , TiO_2 and ZnO , see below).

Whereas the deposition of Prussian Blue (PB) served as a model system to prove that electrodeposition was possible, a more useful system was expected from the TiO_2 on ATO. In contrast to the ITO nanofibers that were not sufficiently stable in acid solution, the ATO fibers could be employed in anodic electrodeposition of TiO_2 from TiCl_3 . The advantage of anodic deposition is the controlled manner in which the oxide is formed by oxidation of Ti(III) to Ti(IV) ¹⁶ only on the conductor. Actually, the TiO_2 forms as mostly crystalline rutile (whereas for cathodic current OH^- is generated from O_2 and leads to amorphous oxides/hydroxides around the electrode). The addition of surfactants like SDS (sodium dodecylsulfate) or BTB (bromothymol blue) allows the generation of porous titania [46], [47].

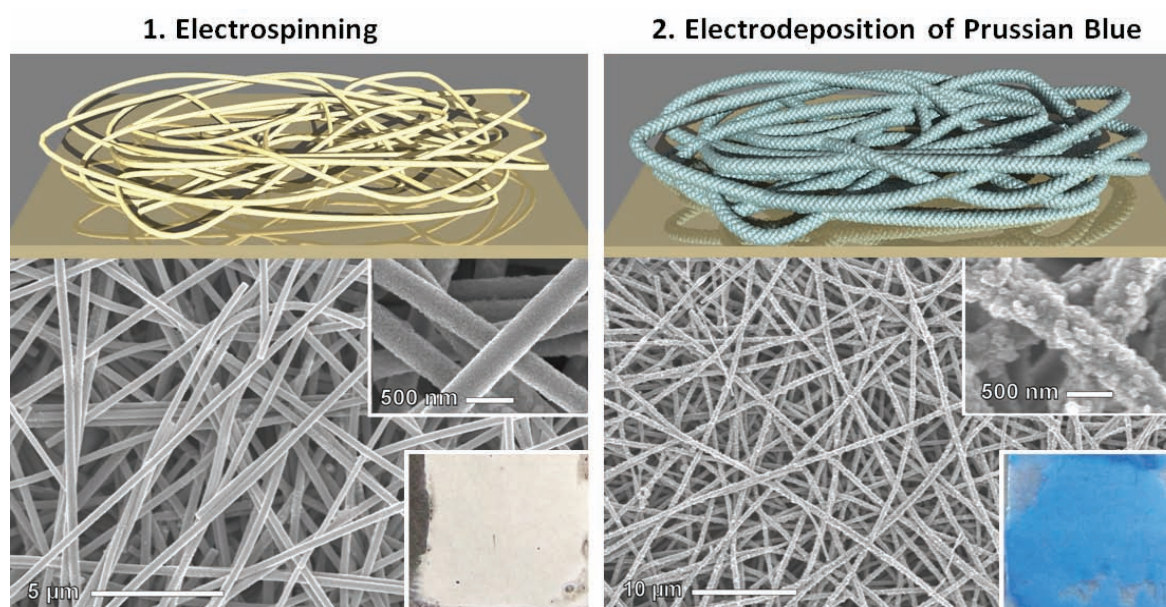


Figure 2-11: ATO nanofiber electrode before (left) and after (right) PB electrodeposition: Scheme, SEMs and digital photograph of fiber mat used as electrode (lower inset)

¹⁵ These results have been partially published [44].

¹⁶ At a given pH and temperature, Ti(IV) is much less stable in solution and forms hydroxides that readily transform into TiO_2 [45].

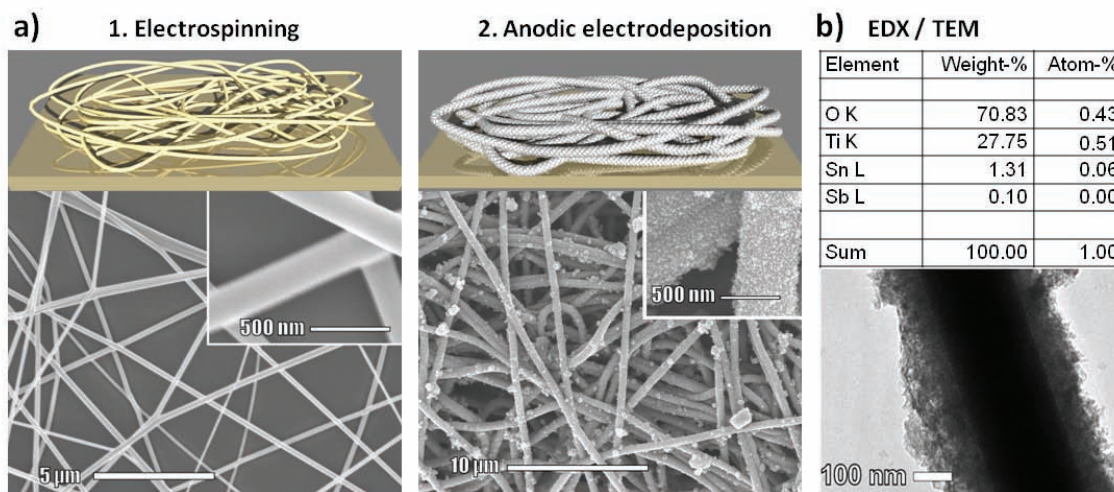


Figure 2-12: a) Scheme and SEM of ATO nanofibers before and after electrodeposition of TiO_2 from TiCl_3
 b) EDX analysis of the composition and TEM image of ATO fibers covered with TiO_2

However, as-prepared the nanofiber mats adhered poorly to the FTO substrates¹⁷ and tend to peel off during electrodeposition of TiO_2 . Therefore, a thin layer of ATO was applied by spray pyrolysis to improve mechanical and electrical contact to the substrate.

Using anodic electrodeposition both flat substrates and nanofibers could be uniformly coated with a titania layer (see Figure 2-12). Typically, the deposition current was 0.25 mA/cm^2 on flat electrodes and 3-4 times higher on nanofibrous electrodes due to their higher surface area.

However, when the thickness of the titania layer exceeded 500 nm on flat substrates cracks appeared and the film tended to peel off, thus severely limiting light absorption and the solar cell efficiency. In contrast, a deposition of 500 nm of TiO_2 on each nanofiber in a thick fiber mat resulted in an overall titania thickness of several microns. Consequently, the dye-sensitized solar cells based on our nanofibrous ATO electrodes generated a much higher photocurrent than similarly prepared solar cells on flat FTO substrates.

As shown in Figure 2-13, conversion efficiencies of 1.5% have already been observed without any optimization, still allowing for further improvements, for example by using other dyes and laminated cell assembly¹⁸.

¹⁷ A flat FTO substrate was always used as back contact instead of a glass slide to avoid a high internal resistance.

¹⁸ In the setup used at the physics department of JLU Giessen, the distance between the electrodes was several millimeters, while the state-of-the-art is $50 \mu\text{m}$ and below.

Optimizations and further experiments, including electrodeposition of other metal oxides like zinc oxide, are currently carried out by our collaborators and might substantially improve the solar cell performance. Solar cells based on nanofibers and nanorods of TiO_2 and ZnO have already been demonstrated [48], [49].

The photoelectrochemical performance of the studied systems is summarized in Table 2-3. The presence of ATO nanofibers in the electrode significantly increased the short circuit photocurrent, decreased the open circuit voltage and the fill factor. As a net consequence, the observed cell efficiency was clearly enhanced.

Table 2-3: Comparison of photoelectrochemical measurements: Thickness of the TiO_2 layer, short-circuit current, open-circuit voltage, fill factor and conversion efficiency.

System	d [μm]	J_{SC} [mA/cm^2]	V_{OC} [V]	FF [%]	η [%]
edepot ¹ TiO_2 on FTO	0.4 [#]	0.9	0.77	49	0.36
edepot ¹ TiO_2 on ATO nanofibers	0.4 [#]	3.9	0.56	33	0.74
edepot ¹ TiO_2 on ATO nanofibers with add. spray pyrolysis	0.4 ^{#,*}	6.8	0.58	38	1.49

¹ electrodeposited

[#] thickness of TiO_2 layer on flat films or the individual nanofibers, the overall thickness for the nanofibrous electrodes is 2-2.5 μm

^{*} possibly up to 0.5 μm due to lower series resistance

The increased photocurrent was probably caused by an increased amount and overall surface

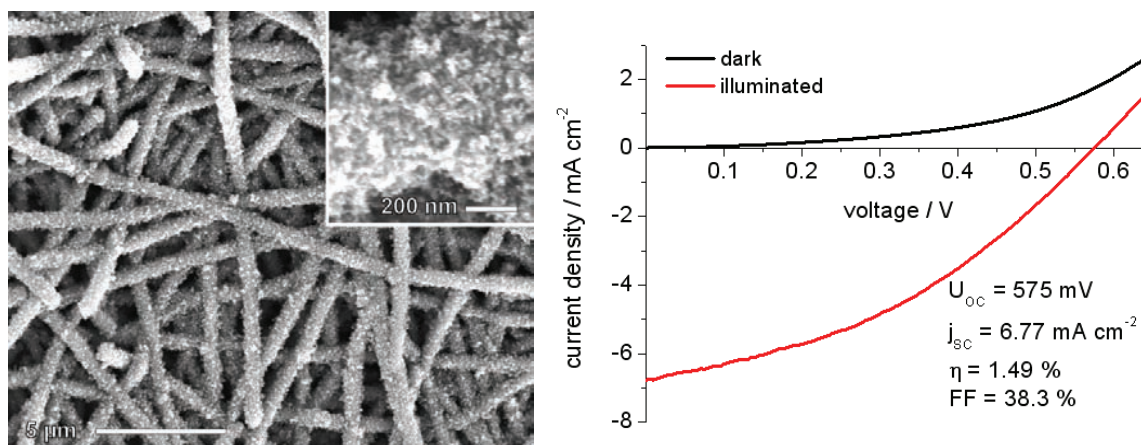


Figure 2-13: SEM image of ATO nanofibers covered with TiO_2 and results from DSSC photoelectrochemical measurement

area of the TiO_2 coating on the ATO fiber network and the resulting higher sensitizer content. The larger effective surface area of the electrode in turn led to increased recombination reactions with the electrolyte both from uncovered ATO parts and the TiO_2 surface especially since it was not blocked by coadsorbates in the present study. To further enhance the solar cell performance and limit the recombination losses, it would be necessary to form a continuous blocking layer of non-porous TiO_2 over the entire electrode including the nanofibers. Atomic layer deposition or other gas phase techniques might be more suitable for uniform oxide deposition, but for this study we limited our approach to the electrodeposition of TiO_2 without surfactants, resulting in denser, but unfortunately not completely dense layers.

The increased recombination was reflected in a decreased fill factor (lowered shunt resistance) and a decreased photovoltage under open circuit. Additional sources of recombination might also lie in a possible mismatch between the conduction bands of FTO-ATO and ATO- TiO_2 or in dead ends of electronic conduction in isolated ATO fibers, i.e. fibers without contact to the FTO back electrode. The deposition of a thin ATO layer by spray pyrolysis led to a clear improvement of the cell efficiency caused by a significantly increased photocurrent and a slightly increased fill factor. This observation may be attributed to an improvement of the conductivity through the nanofiber network and to the underlying FTO electrode.

2.7 Conclusion for the ATO-DSSC

A literature review indicates that TiO_2 might not be the best choice as semiconducting oxide for our model system, as especially under illumination¹⁹ its electronic transport suffices for DSSC applications [52], [53], thus reducing the need for additional conducting pathways like the ATO nanofibers that might prove more useful in less conducting oxides like ZrO_2 .

Although there is some advantage in the electron collection due to the presence of the ATO nanofibers, it was decided not to investigate the DSSC systems any further, as it was already shown that the main bottleneck in DSSCs is not electron transport in the nanocrystalline TiO_2 , but the mass transport in the electrolyte [54].

In fact, the simple model for electron transport in DSSC by diffusion is insufficient and needs to be extended further than modeling the long-range electron transport as a series of trapping/detrapping events [55]. The apparent diffusion coefficient of the electrons is orders of magnitude lower than expected for electrons in crystalline solids and rather in the range of the diffusion coefficient of the electrolyte. Furthermore, it was shown that a layer of 50 μm TiO_2 offers a more efficient collection of the electrons injected at the outermost part than thinner films [56]. In general, thicker TiO_2 films produce higher photocurrents than their thinner homologues. Therefore, it is more suitable to regard the nanocrystalline TiO_2 films as three-dimensional electrodes and their conductivity to result from a self-doping process that is initiated by illumination and supported by charge compensation through the electrolyte [54].

In conclusion, TiO_2 and other nanocrystalline metal oxides might not be the most suitable system for the ATO nanofibers and they should rather be employed where improvement of electronic conductivity is necessary, i.e. in insulators to form conducting hybrids.

¹⁹ While being low in the dark, the conductivity of TiO_2 increases 2-4 orders of magnitude under illumination and is further increased through electron injection from the dye molecules [50], [51].

2.8 Transparent Conducting Polymer Films

A far more promising application of the TCO nanofibers could be found by embedding them in a polymer matrix. In such a nanocomposite, electrical conductivity can be obtained above a certain volume fraction of the conducting phase allowing the formation of a continuous network in the insulating phase. This so-called percolation threshold critically depends on the dimensionality of the conducting phase, i.e. the shape and aspect ratio of its building blocks. In this respect, well-distributed, long nanowires with a high aspect ratio can reduce the percolation threshold to well below 1 vol% [57].

The following Figure 2-14 from the literature [58] shows the percolation threshold of the conductivity of composites made of epoxy resin and CVD-grown multi-wall carbon nanotubes (MWCNT) and carbon black, i.e. an increase of several orders of magnitude in conductivity at a certain concentration of the conducting phase inside the epoxy matrix.

Two facts merit special attention in Figure 2-14:

- The percolation threshold critically depends on the nature of the conducting phase, i.e. one-dimensional nanotubes outperform particulate carbon black, and on how well the conducting phase is distributed in the matrix²⁰.
- The transparency of the composite is greatly lowered by the incorporation of MWCNT leading to a non-transparent epoxy before the onset of conductivity.

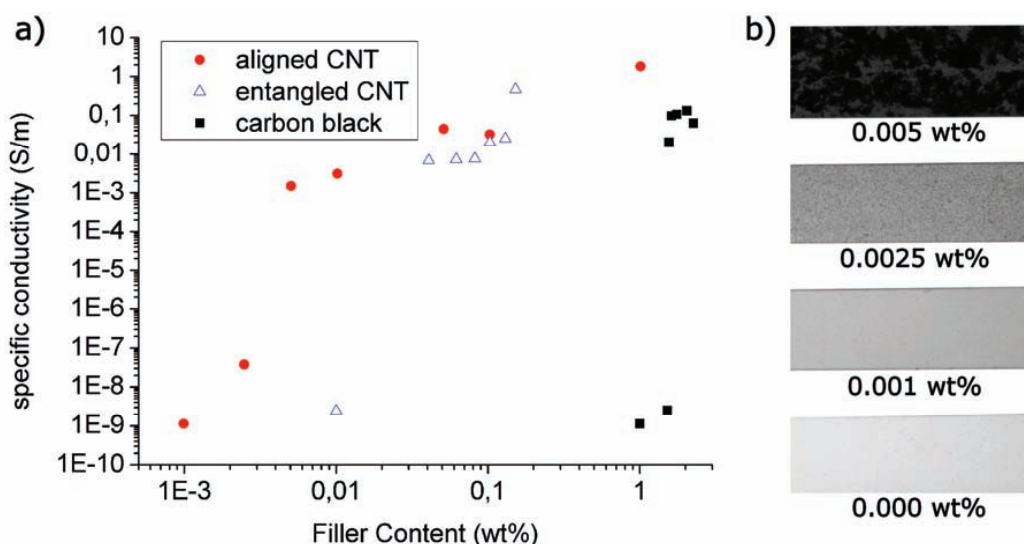


Figure 2-14: a) Electrical conductivity of epoxy composites with aligned or entangled carbon nanotubes or carbon black as conducting filler
b) Digital images of the aligned CNT-epoxy composites with different loadings of carbon nanotubes (CNT) (adapt. from [58])

²⁰ Insufficient singularization, i.e. the occurrence of bundles instead of individual fibers, often requires a much higher concentration of nanotubes than expected from their high aspect ratio [57].

Accordingly, it is possible to produce conducting composites from insulating polymers or resins by adding a low weight fraction of conducting nanowires. However, using carbon nanotubes only non-transparent composites can be obtained.

Thus, the transparent conducting oxides might be a viable route to create conducting polymer films. The ATO nanofiber mats could indeed be incorporated into insulating polymers like polystyrene or polyvinylpyrrolidone to yield conductive or at least antistatic (depending on the fiber concentration and film's thickness) composites.

In fact, the nanofibers usually appear grayish-white due to light scattering at the fiber-air interface, but within the polymer matrix, the transparency is similar to the pure polymer film, as the refractive index of the polymer is higher than the one of air (see Table 2-4).

Table 2-4: Refractive indices n_D (at 589 nm and 0°C)

System	n_D	Ref.
air	1.00027	[59]
polystyrene	1.5582	[60]
SnO ₂	1.953-1.998	[59]

Although it was not easy to redisperse the nanofiber mats as individual nanofibers in polymer melts or solutions, it was possible to infiltrate the free-standing mats with a polymer solution.

This process could be further improved by hot pressing the nanofiber mat into thin polymer films to yield the composite shown in the Figure 2-15.

A resistance in the range of 10-1000 k Ω /cm was measured by 2-point probe, depending on the relative thickness of the ATO mat and the polymer film²¹. Flat electrodes were used to measure a resistance of 100-1000 k Ω through the films with an approximate thickness of 50 μ m.

²¹ Obviously, the nanofibers can be contacted directly by forcing small electrodes into the composite, thus it was possible to show that the nanofiber mat retained its full conductivity inside the polymer matrix (a resistance of 1-10 k Ω /cm was measured).



Figure 2-15: Digital photograph of ATO nanofiber mats a) in air and b) inside PS, c) of ATO-PS film with a laser microscope and d) the setup for the conductivity measurement

In conclusion, these hybrids take advantage of the nanofibers' conductivity and transparency while offsetting their fragility and therefore represent an interesting new type of antistatic and transparent polymer film.

In general, as demonstrated for the polymer-CNT or polymer-TCO composites, it seems more viable to use the nanofibers in matrices with a specific conductivity that is orders of magnitude lower than the nanofibers' conductivity. Accordingly, conducting oxides might not always represent the best material for the conductive pathways. Whenever transparency is not required metals might be an alternative that offers a lower specific resistivity. Their use in form of nano-wires will be discussed in the next section.

2.9 Metal Nanowires

The specific resistivity of metals is three orders of magnitude lower than of the transparent conducting oxides or carbon and low-purity carbon nanotubes (see Table 2-5). Accordingly, metal nanowires should be beneficial where high conductivity is necessary and might prove useful as three-dimensional electrode in applications like lithium batteries.

Table 2-5: Specific Resistivities ρ at 20°C

Material	$\rho / \Omega \cdot \text{m}$	Ref.	Material	$\rho / \Omega \cdot \text{m}$	Ref.
Silver	$1.59 \cdot 10^{-8}$	[61]	ITO*2	$8.5 \cdot 10^{-7}$	[40]
Copper	$1.68 \cdot 10^{-8}$	[61]	FTO*2	$5.5 \cdot 10^{-6}$	[62]
Nickel	$6.99 \cdot 10^{-8}$	[61]	ITO#	$2 \cdot 10^{-5}$	[38]
Platinum	$1.06 \cdot 10^{-7}$	[61]	FTO#	$5 \cdot 10^{-5}$	[38]
Carbon	$3.5 \cdot 10^{-5}$	[61]	ATO#	$1.0 \cdot 10^{-5}$	[38]
CNT*1	$1.0 \cdot 10^{-6}$	[63]	RuO ₂	$3.5 \cdot 10^{-7}$	[64]

*1 lowest values ever reported for metallic fullerene single-wall nanotubes

*2 lowest values reported from Pulsed Laser Deposition (PLD)

values from spray pyrolysis

There have been several attempts to metalize nanofibers [65] or to incorporate metal nanoparticles [66], but also to produce metallic nanowires directly via electrospinning. Copper, iron and nickel nanofibers have been reported [67-69] and a low resistivity of $1.2 \cdot 10^{-6} \Omega \cdot \text{m}$ was measured by contacting a free-standing single Cu fiber with a tip of a micromanipulator. While these local measurements prove that the fibers mostly consist of metal, no macroscopic resistance was reported and no device was prepared. Instead most of the literature focuses on the anisotropy of the magnetic properties of the fibers [69], [67], [68]. Testing the nickel and copper nanowires provided by the authors [67], it was apparent that the average length of the fibers was only a few micrometers and that they were very sensitive to oxidation, thereby losing their conductivity²². As chemical and thermal treatments are necessary for the preparation of most composite structures, nanowires of these metals are not applicable to such structures.

In contrast, noble metals like gold or platinum are known for their excellent thermal and chemical stability and especially Pt is a widely used electrode material. Recently, there has been a report on the electrospinning of Pt nanofibers [73] from PVP and the authors propose to use the

²² In fact, there have been numerous reports of nanofibers made from the oxides of copper, iron and nickel [70], [71] and recently first devices were fabricated based on p-conducting CuO [72].

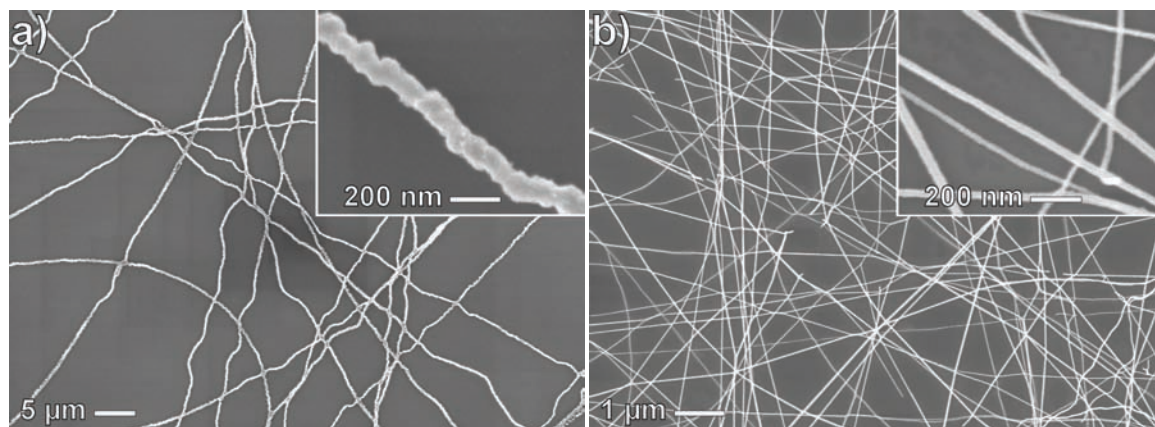


Figure 2-16: SEM images of a) Pd and b) Pt nanofibers electrospun from PVP after polymer removal at 450°C

fibers in fuel cells. However, Pt fibers are also of potential interest as electrodes in novel biosensors.

A similar electrospinning approach was independently developed for Pd and Pt, starting from nitrates as precursor (see Figure 2-16), with the details of the preparation and characterization given in the experimental part of this work.

Whereas the Pd fibers needed to be reduced under H_2/N_2 after polymer removal, the platinum wires were stable up to 650°C and the polymer could be conveniently removed under air.

As expected, the Pt nanowire mats were highly conductive while being grayish to semi-transparent depending on the amounts of nanowires (see Figure 2-17).

To further prove the macroscopic conductivity, Prussian Blue was deposited on the fiber mats and could be cycled electrochemically. However, due to their small diameter, the Pt fibers deformed easily and all fibers lay flat on the substrate, resembling a thin film with holes rather than a non-woven mat. Only the latter represents a three-dimensional electrode that might be

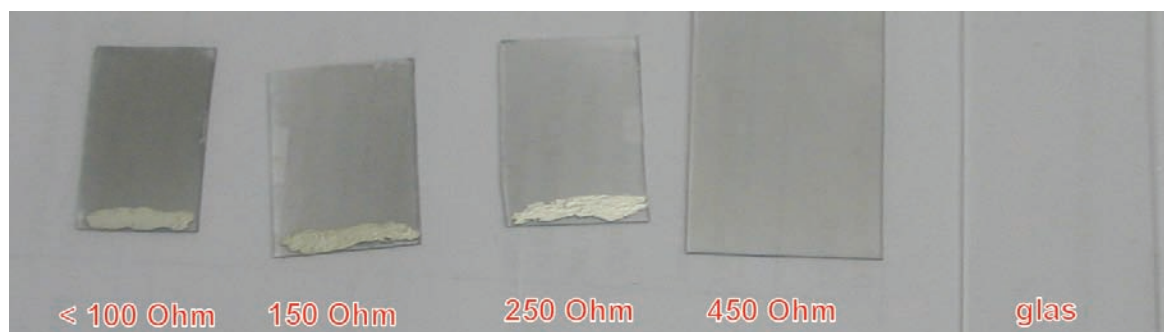


Figure 2-17: Digital image of Pt nanofiber mats of different thickness deposited on glass slides (resistance in Ohm/cm)

beneficial to many electrochemical applications. A co-spinning approach [74] was employed to simultaneously spin two different solutions and mix the resulting nanofibers of SiO_2 and Pt on a rotating collector. As can be clearly seen in Figure 2-18, the thick SiO_2 fibers were the structural element to span a tortuous network into which the thin Pt wires were embedded. Therefore, the resulting mat was a three-dimensional electrode that combined the good mechanical stability of the SiO_2 fibers and the high conductivity of the Pt wires.

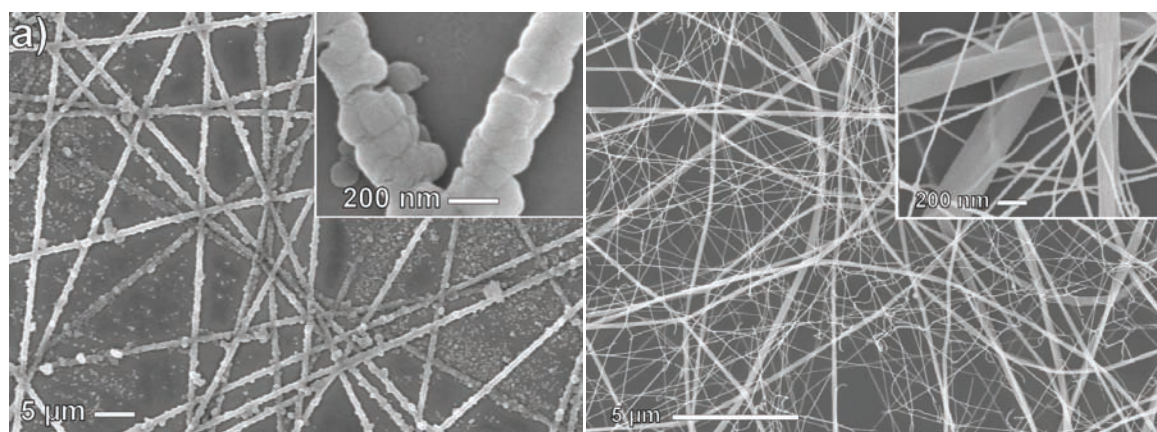


Figure 2-18: SEM images of a) Prussian Blue deposited on Pt nanofibers and b) Pt nanofibers co-spun with thicker SiO_2 nanofibers

2.10 Applications of Metal Nanofibers

A three-dimensional electrode can provide facilitated mass transport while increasing significantly the electroactive surface area. Investigations into this direction are currently carried out by our collaborators from LCPME Nancy. On quasi-two-dimensional Pt fiber mats, they could already demonstrate the electro-assisted sol-gel deposition of SiO_2 for the enzyme encapsulation of glucose oxidase. In this system, the Pt fibers are sensitive to hydrogen peroxide released during enzymatic oxidation of glucose and the modified electrode shows good catalytic activity and was found to be sensitive to changes in the glucose concentration of the solution (see Figure 2-19). Interestingly, the response of the modified electrode depends strongly on the film thickness that can be tuned by electrodeposition time, with the best response being observed when the SiO_2 film thickness is similar to the diameter of the individual Pt nanofibers. This finding is under further investigation and can most likely be explained by an optimum between the amount of enzyme and the distance to the Pt fibers. Moreover, there might be some mass transport limitations that should be absent in a three-dimensional system. For the first measurements, only Pt nanofibers were used that tended to form a single layer on the substrate (i.e. a mat without any significant thickness perpendicular to the substrate, see Figure 2-16).

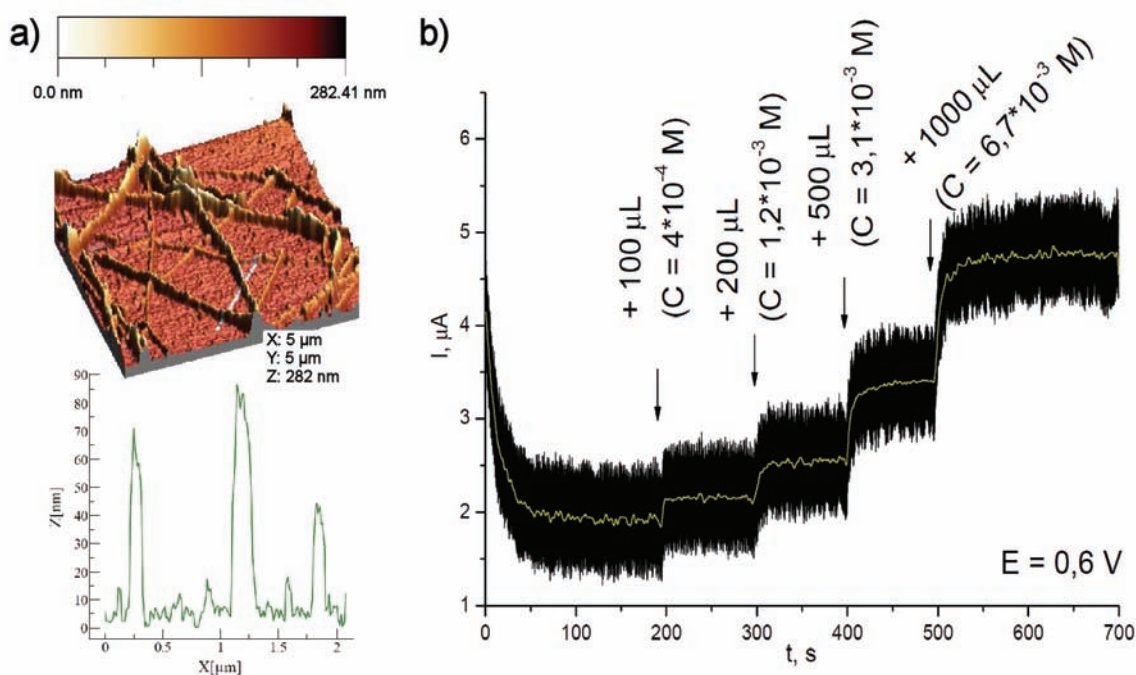


Figure 2-19: Pt-nanofibers-on-glas-electrode onto which the enzyme glucose oxidase has been electrodeposited in silica:
 a) AFM image with the corresponding height profile (along the white line)
 b) Typical response as electrocatalytic sensor to increasing amounts of glucose
 (These measurements were conducted by M.Etienne, LCPME Nancy)

Another system, where the nanofibers proved useful, is YSZ (Yttria stabilized Zirconia). As oxide ion conductor with applications in SOFC (solid oxide fuel cells), YSZ is usually contacted via a rather thick, porous Pt coating that represents a trade-off between sufficient conductivity and a low diffusion barrier to oxygen. In this respect, the nanofiber mat requires only a fraction of the amount of Pt and adheres better to oxide substrate.

More importantly, due to the quasi-one-dimensional nature of the Pt nanofibers, there is almost no interfacial area between YSZ and Pt and the only interface is the triple phase boundary (TPB) of YSZ, Pt and the gas phase. In first experiments an electrode was produced from Pt nanowires on YSZ and the first results already showed that the exchange current is significantly increased compared to an YSZ electrode with Pt paste (see Figure 2-20).

Unfortunately, due to their low diameter, the nanowires were not stable at high temperatures and started to coalesce into nanoparticles above 600°C (see Figure 2-21). As the SOFC performance is limited by slow O^{2-} diffusion at low temperature, it is desirable to use temperatures beyond 500°C and if possible up to 900°C. Obviously, the nanowires are not suitable for this application, but wires with a higher diameter might be able to withstand 700-750°C, because the melting point of Pt is significantly higher (1768°C).

In any case, the nanowires could be of interest for fundamental studies, as they provide a facile way to control the size of the interface area between YSZ and Pt and the size of the TPB. It was shown that the insertion and extraction of oxygen only takes place at the TPB and it was proposed that an additional interface of YSZ and Pt only creates irreversible artifacts resulting from

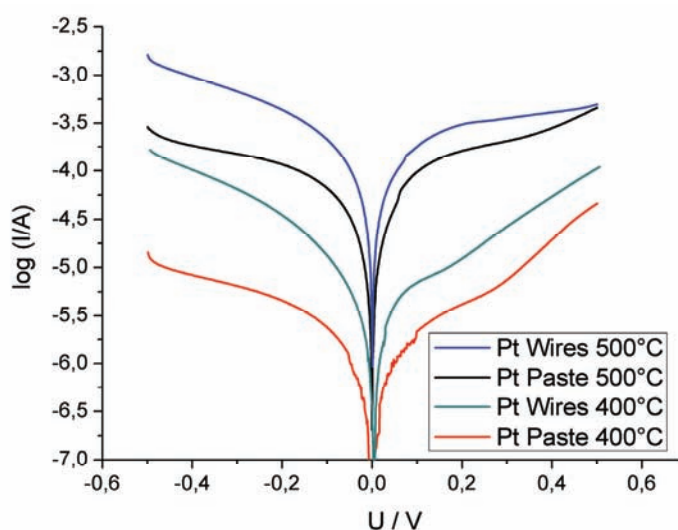


Figure 2-20: Comparison of the performance of YSZ electrodes in a solid oxide fuel cell (SOFC) made with commercial Pt paste or electrospun Pt nanowires at 400 and 500°C
(These measurements were done by H.Poepke, AG Janek, JLU Giessen)

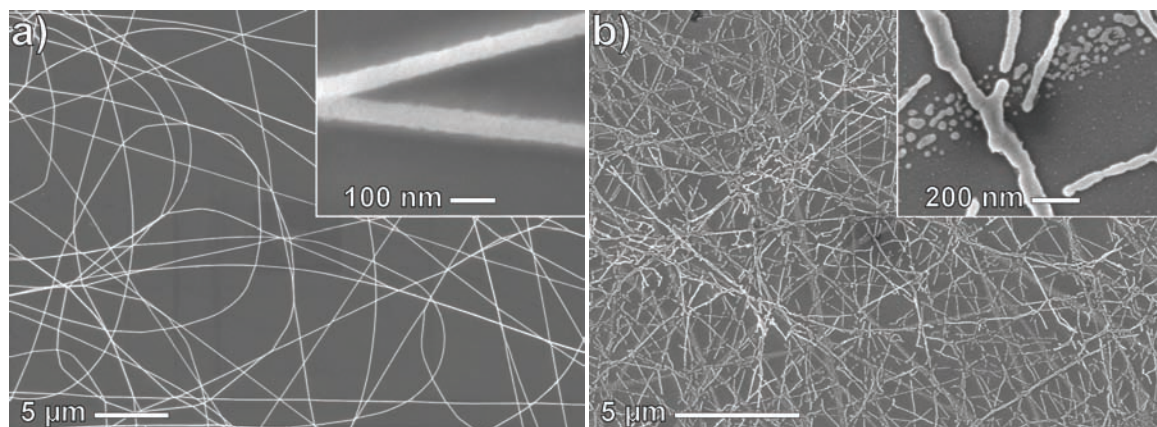


Figure 2-21: Pt nanowires on YSZ a) as-prepared and b) after 5 h at 600°C

its interfacial capacitance in the experiments.

Thus, by reducing the interface area between YSZ and Pt, less artifacts should be observed and the electrode might become completely reversible for the thin Pt wires.

In conclusion, Pt nanofibers are very promising as electrode material due to their high conductivity, as well as their chemical and thermal (currently up to 600°C) stability.

Chapter 3 – Porous Nanofibers

3.1 Concept of Porous Nanofibers

Porous metal oxides have proven invaluable for many applications including sensing and catalysis [75], [76], yet further fields like charge storage and microelectronics [77] are currently emerging especially for ordered mesoporous materials. Most commonly, hard and soft templating approaches are employed to generate the desired porosity in thin films and powders [75].

Over the last decade, there has been considerable progress in the sol-gel synthesis of mesoporous materials, especially in soft templating based on block copolymers [78], [79]. After consolidation of the oxide framework, the template can be removed by extraction or simply by calcination to produce the porous oxide. With a diameter of the mesopores ranging from 2 - 50 nm, these materials possess specific surface areas of 200 – 1000 m²/g depending on the porosity and the material's bulk density. Yet they offer better accessibility than microporous zeolites with diffusion-limited transport [80], [81], in particular when combined with macropores to form bimodal pore systems. Due to the ease in synthesis from lyotropic phases of spherical (and cylindrical) micelles and in characterization by small angle scattering techniques, there have been many works on ordered mesoporous systems. Although ordered porosity is dispensable for most applications, such systems facilitated the study of fundamental questions, such as accessibility and pore filling as a function of pore geometry and connectivity [82], [83].

The ideal pore system is hierarchical, i.e. a combination of macroporous transport pathways with meso- and microporosity to enlarge the surface area. An important example can be found in monolithic silica columns that are useful for numerous applications, especially in chromatography [84], [85]. These monoliths are conveniently synthesized by spinodal demixing and offer a bicontinuous porosity over several length scales.

Another approach to obtain hierarchical porosity would be to assemble micro- and mesoporous building blocks like porous nanofibers into macroporous structures. Electrospinning actually produces nanofibers assembled into non-woven mats with open porosity and excellent accessibility. However, the specific surface area of smooth fibers is rather low, typically 5-15 m²/g for polymer fibers and 10-40 m²/g for metal oxides depending on the diameter of the fibers. For pure polymer nanofibers many procedures have been proposed to tune the morphology of the fibers, but a significant increase in surface area was never reported (see chapter 3.6 for a detailed discussion).

As mentioned above, metal oxides can be templated by self-assembly of surfactants and block copolymers into a lyotropic two-phase system consisting of the hydrophobic template and the hydrophilic metal oxide/hydroxide gel. Upon aging a sol-gel process leads to solidification of the inorganic matrix from which organics can then be removed [78].

Transferring this templating procedure to prepare porous nanofibers would allow realizing the hierarchical system depicted in Figure 3-1 with porosity over several length scales. In this hierarchical pore system, the micro- and mesoporosity offers a high surface area, while the fibers are sufficiently separated in the non-woven mat to enhance transport by diffusion or even convection. In suitable flow conditions²³, forced convection should be possible between the fibers and thereby their diameter represents the maximum diffusion pathway. Accordingly, by tuning the fiber diameter and packing density, both diffusive and convective transport regimes can be controlled.

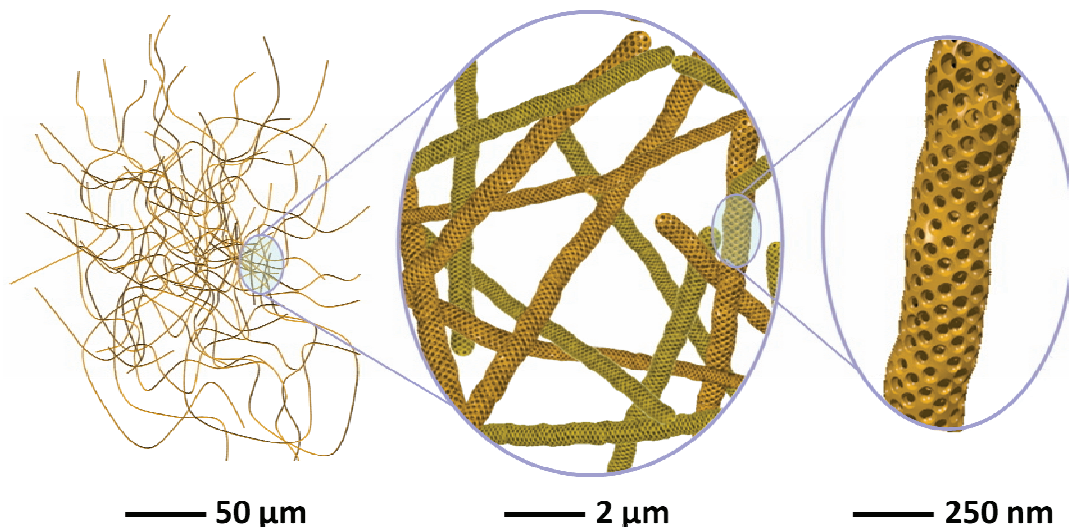


Figure 3-1: Hierarchical structure of porous nanofibers offering high surface area and good accessibility

²³ Empirically Darcy's law describes laminar flow through porous bodies, with the permeability K given by:

$$K = \frac{Q \cdot \eta \cdot l}{\Delta p \cdot A} \text{ with } Q: \text{ flow rate, } \eta: \text{ dynamical viscosity of the fluid, } l: \text{ length of porous medium, } \Delta p: \text{ pressure difference, } A: \text{ area of porous medium}$$

The unit of K is m^2 , i.e. the permeability is approximately proportional to the square of the pore dimension (in case of a tube (Hagen-Poiseuille): $K \sim r^2$). This means that forced convection is possible for sufficiently high pressure and especially for big pores [86].

Unfortunately, the practical realization of templated fibers is not as straight-forward as adopting thin film templating procedures. Although the necessary sol-gel processes should also occur in nanofibers, the presence of the carrier polymer largely affects the self-assembly of the template and prevents the formation of the lyotropic phase. Accordingly, no mesoporosity develops when adding block copolymer templates to electrospinning solutions containing sol-gel precursor and carrier polymer. The latter is usually required to increase the solution's viscosity and thereby prevents break-up of the electrospinning jet, but it has been demonstrated that electrospinning is also possible from sufficiently aged sol-gel solutions with an appropriate viscosity. Although the fibers are less uniform without any carrier polymer, conventional templating with block copolymers is possible for these solutions and mesoporous nanofibers from TiO_2 have been obtained as proof of principle [21], [87]. However, the spinning solutions are quite unstable due to their continued increase in viscosity and can only be used for 20-30 minutes before gelation occurs.

Therefore, it is desirable to find other procedures to prepare porous nanofibers. An elegant approach would be to employ the spinning polymer as template, i.e. by using a precursor that phase separates from spinning polymer upon or after fiber formation. Using dispersions of amorphous and crystalline nanoparticles, a demixing from the carrier polymer could be obtained and will be discussed in following sections.

Another approach to incorporate highly porous nanoparticles into polymer fibers to obtain a porous hybrid will conclude this chapter. Further attempts to stabilize transient morphologies in polymer systems through sol-gel processes will be presented in chapter 4.

3.2 Phase Separation vs. Solidification

As mentioned in the previous section, phase separation is a powerful means to prepare porous materials over several length scales. Nakanishi et al. developed and elucidated a versatile approach in which the sol-gel process of an alkoxy silane solution drives its spinodal decomposition while “freezing” the resulting co-continuous structure [88], [89]. Solution composition, reaction conditions and additives like polymers and surfactants allow tuning the micro- and macro-porosity. Controlling the rates of sol-gel hydrolysis and gelation relative to the phase separation into solvent-rich and solvent-poor phases, is the key to obtain the desired structures. With SiO_2 still being the most studied system, the procedures could recently be extended to TiO_2 and other metal oxides [85], [89].

Obviously, it would be desirable to control the morphology of nanofibers via such phase separation processes. However, electrospinning occurs on a much faster time scale than sol-gel processes of SiO_2 and a molecular precursor would simply evaporate during fiber formation. Therefore, pre-aged SiO_2 solutions were tested with PVP (see Figure 3-2a) and PEO as spinning polymer, but no porosity was observed²⁴. The emerging inorganic does not phase separate enough from the polymer or the solvent, or the inorganic network is not sufficiently stable and simply shrinks during the rapid solvent evaporation. The situation resembles the case of a too slow sol-gel process in monolithic silicas leading to the collapse of the structure. For monoliths, this can be prevented by an increase in temperature that accelerates the network formation and slows down the phase separation [89].

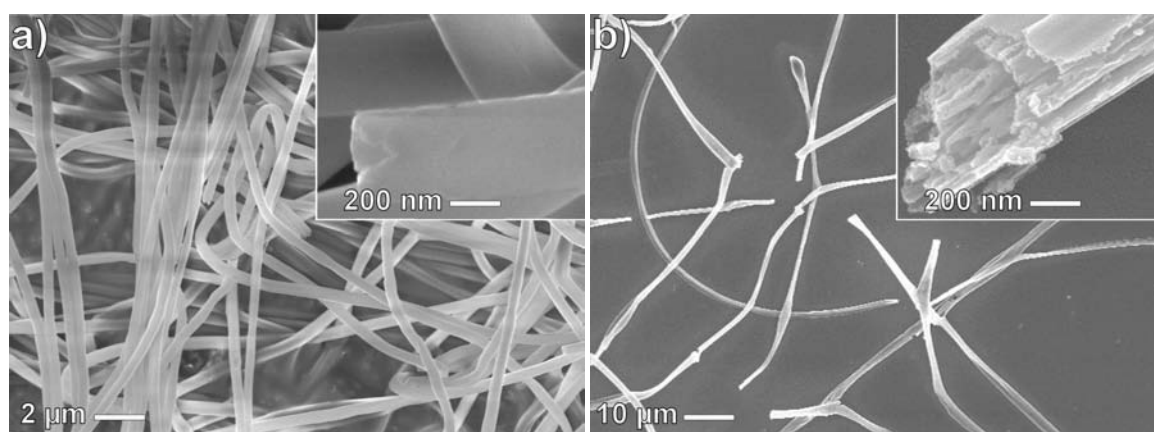


Figure 3-2: SEM images of a) non-porous SiO_2 fibers from PVP and b) templated TiO_2 fibers from PVP-PS after calcination

²⁴ Yet the obtained amorphous SiO_2 nanofibers were not brittle and possess excellent mechanical properties, making them very useful to stabilize crystalline, but brittle ATO or TiO_2 nanofiber mats on substrates.

In electrospinning, more reactive precursors or metals would lead to a faster sol-gel process, but as reported in the literature not even sol-gel-derived TiO₂ nanofibers show any appreciable internal morphology [90].

Hence, it is reasonable to assume that during electrospinning, solvent evaporation is too fast to allow for significant phase separations²⁵. Accordingly, the predominant process is solidification, in agreement with reports from coaxial electrospinning. There, a solid sheath can be formed around a liquid core, preserving the interface between two immiscible liquids, i.e. the two already existing phases.

Adding polystyrene (PS) as an immiscible second polymer to a sol-gel TiO₂/PVP solution leads to a two-phase system. In fact, electrospinning of such an emulsion²⁶ is possible and results in fibers with a smooth surface, as the gelation of the TiO₂ occurs predominantly at the surface. Inside the fibers there are PVP and PS domains. The sol-gel precursor is only present in the PVP domains, whereas the PS acts as template to generate channel-like structures inside the fibers, as shown in Figure 3-2b after calcination.

Although porous and hollow fibers can be obtained in this way [91], the spinning solution is a rather unstable turbid emulsion and the quality of the electrospinning is poor, resulting in break-up and inhomogeneous diameter of the fibers.

In conclusion, phase separation is not observed during the rapid process of electrospinning and only two-phase systems lead to porous morphologies. Due to fast solvent evaporation, the fibers quickly solidify and “freeze” in the present composition. Sol-gel processes cannot be completed and while amorphous hydroxides may form at the surface, most of the precursor remains inside the fibers until calcination removes the polymer and densifies the inorganic to obtain compact fibers.

This conclusion is in agreement with the results from the ATO nanoparticles: Amorphous stannic acid allowed generating compact, well-conducting fibers, whereas fully crystalline nanoparticles lead to more porous, less conducting nanofibers. Accordingly, the use of crystalline nanoparticles will be explored in the next section.

²⁵ As discussed in the introduction [see chapter 1.3], the porosity generated by the condensation of ambient humidity does not represent a phase separation.

²⁶ See chapter 4.3 for a discussion of emulsion electrospinning.

3.3 Nanoparticulate Fibers

For most crystalline nanoparticles, the crystal faces have similar energies and it is therefore reasonable to assume that nanoparticles approximately possess a spherical shape. From geometric considerations, it can be shown that densely-packed spheres only occupy 74% of the available volume, generating sufficient pore volume between themselves. Within the nanofibers the spinning polymer will probably serve as an additional template and even if some sintering might reduce the porosity, a porosity of 25-35% might be obtained.

Accordingly, the main challenge is to prepare crystalline nanoparticles that form stable dispersions compatible with the carrier polymer, but that are sufficiently reactive to be sintered together. As shown in Figure 3-3, the solution should be "isotropic", i.e. a perfect solution of the polymer and a perfect dispersion of the particles. Thereby, electrospinning produces hybrid fibers from which the carrier polymer can be removed to yield nanoporous fibers. The polymer mainly serves as the template for the fibrous morphology; the porosity is generated by particle agglomeration.

In contrast, the sol-gel precursors are miscible with the polymer and will produce compact nanofibers, as crystallization only occurs during or after polymer removal. Thus, the polymer cannot act as template for porosity.

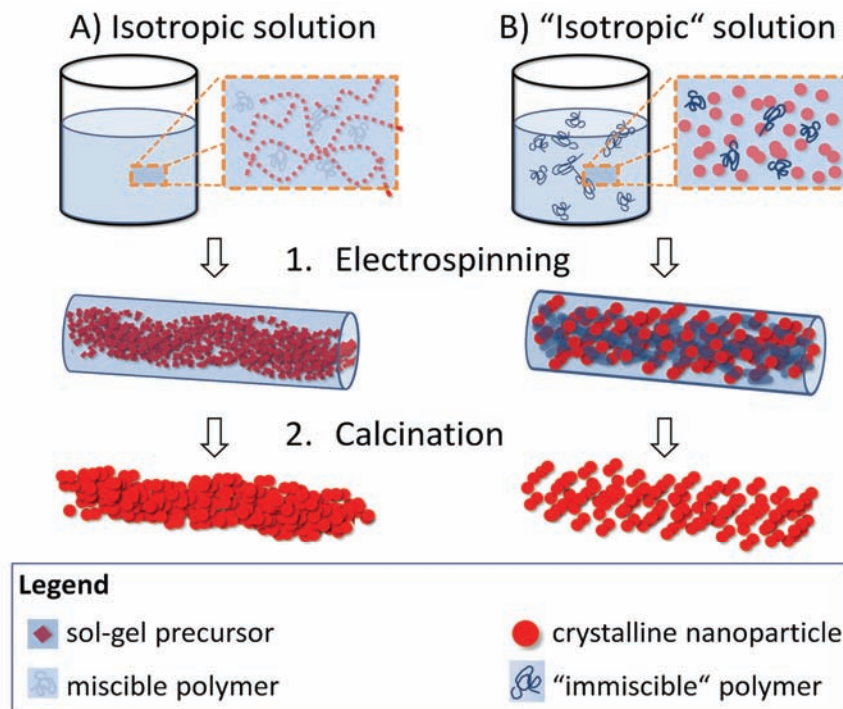
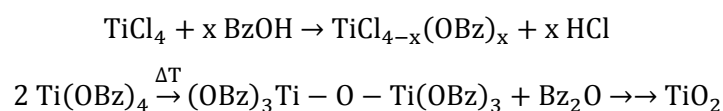


Figure 3-3: Schematic pathways to compact and porous nanofibers using de-mixing of polymer and preformed nanoparticles

Nanoparticle dispersions of various metal oxides can be prepared by non-aqueous routes, for example using metal chlorides as precursor and benzyl alcohol (BzOH) as solvent and oxygen source as proposed by Niederberger et al. [92], [93]. The acid-catalyzed mechanism for TiO₂ can in a simplified version be described as follows:



In order to obtain crystalline nanoparticles, the reaction has to be carried out above 80°C for several hours. After the reaction is complete, diethylether is added to precipitate the nanoparticles that can be redispersed in water or alcohol.

A modified approach with ethanol (EtOH) as co-solvent and 1,3-Propanediol as chelating stabilizer to decrease reactivity led to nanoparticles that were more easily dispersible in methanol (MeOH). Some water improved the dispersibility of the nanoparticles, but led to the slow gelation of the solutions, as in fact the nanoparticles remained largely amorphous due to the ligand (see Figure 3-4). By raising the temperature to 110°C, the synthesis yielded crystalline particles²⁷.

However, the redispersibility of the nanoparticles in MeOH decreases with crystallinity. An important finding is that in contrast to H₂O, the addition of 10-25 wt% DMF (dimethylformamide) facilitated the dispersion without any negative effect on the solution's stability or on the electrospinning. Stable dispersion of 5-10 wt% nanoparticles in MeOH-DMF could be obtained and were miscible with alcoholic solutions of typical spinning polymers like PVP, PVA (poly(vinylalcohol)) or PVB (poly(vinylbutyral)).

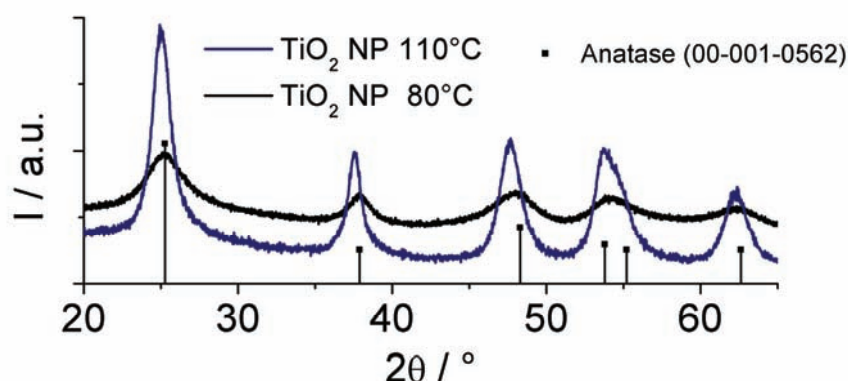


Figure 3-4: XRD analysis of TiO₂ nanoparticles as synthesized at 80°C and 110°C (the background has not been subtracted)

²⁷ Although all experiments were performed by myself, the synthesis protocol for the nanoparticles was mainly developed by C. Weidmann.

3.4 Influence of Nanoparticle Size

The nanoparticle dispersions can be electrospun from solution with PVP as carrier polymer. If the model in Figure 3-3 is correct, the porosity of the nanofibers should depend on particle size and crystallinity. Smaller nanoparticles should lead to a higher surface area, such a dependence was already shown for silica where monodisperse nanoparticles of different sizes are commercially available [94]. In fact, colloidal SiO_2 nanoparticles can be prepared easily by the Stober method [95] in which particle size can be controlled by the ratio of reagents and simply adding more precursor leads to bigger particles [96]. The size control of colloidal TiO_2 is more difficult, due to crystallization and particle agglomeration²⁸. Nevertheless, TiO_2 colloids of four different sizes could be obtained and the resulting nanofibers were compared with regard to morphology and porosity.

The TiO_2 particles synthesized at 80°C in benzyl alcohol are still quite amorphous and behave like sol-gel precursors leading to smooth and compact fibers, whereas the particles produced at 110°C are more crystalline and a rougher surface morphology can be seen in the SEM image in Figure 3-5.

To obtain bigger nanoparticles, EtOH is replaced by toluene in the synthesis that is still carried out at 110°C [97]. Toluene does not act as a ligand and the reaction takes place much faster and needs to be stopped after 40 minutes, as later the solution turns from translucent to turbid due to particle agglomeration. As shown in Figure 3-6, the resulting nanoparticles are much bigger and already clearly visible inside the hybrid nanofiber.

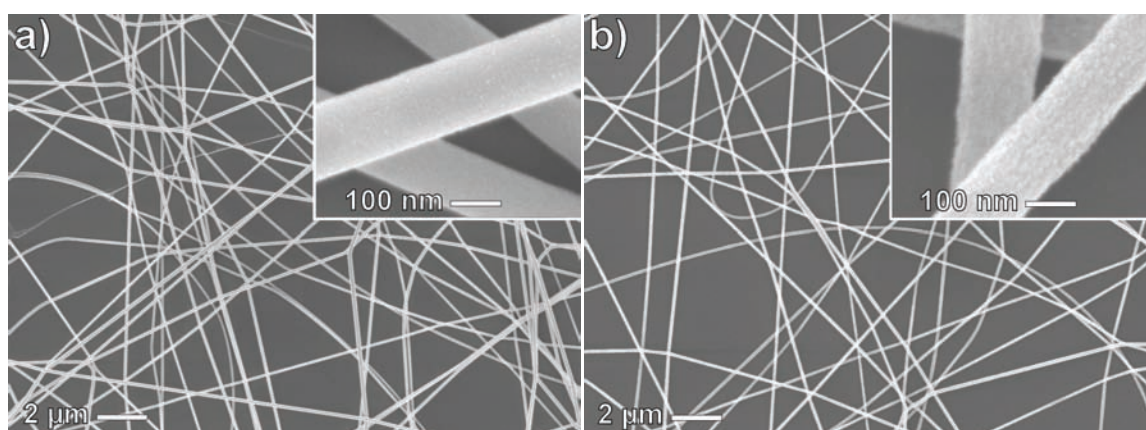


Figure 3-5: SEM images of nanofibers after calcination at 550°C of TiO_2 nanoparticles synthesized at a) 80°C and b) 110°C

²⁸ In fact, sol-gel-derived SiO_2 is fully hydrolyzed and condensed, but amorphous and behaves more like an inorganic polymer with well-controlled “polymerization” chemistry [45].

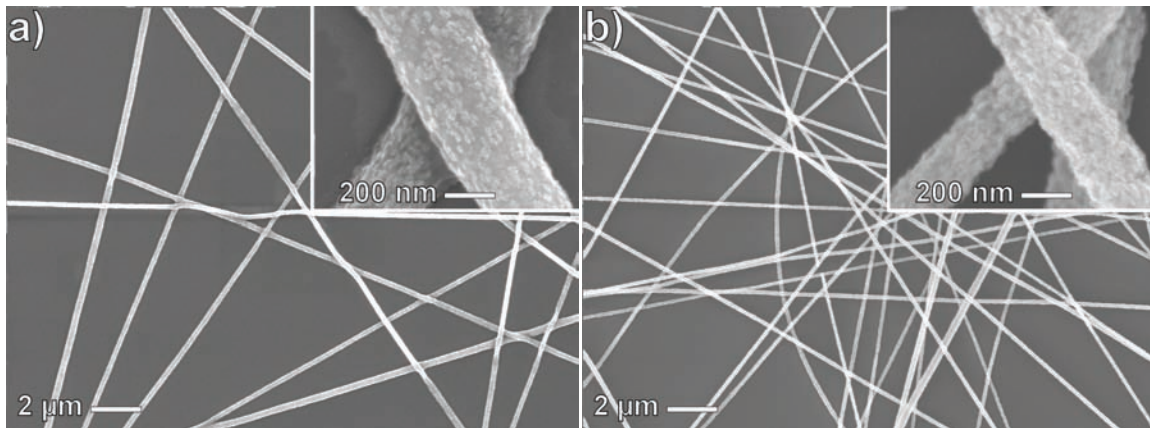


Figure 3-6: SEM images of nanofibers of TiO_2 nanoparticles synthesized in benzyl alcohol and toluene at 110°C : a) before (with PVP) and b) after calcination at 500°C

Upon calcination the diameter of the fibers is reduced and a porous fiber is obtained.

For all systems investigated, the crystalline nanoparticles are homogeneously distributed inside the hybrid PVP-nanoparticle fiber.

Similarly, nanofibers are prepared from molecular sol-gel precursors and from commercial nanoparticles with a bigger diameter of 20-30 nm (see Figure 3-7), resulting in smooth and grainy fibers respectively.

Even from the SEM images, it is already possible to see how the different sizes of the nanoparticles result in different pore sizes. To further confirm the microscopic observations, N_2 adsorption measurements were carried out and the surface area was calculated according to the BET model.

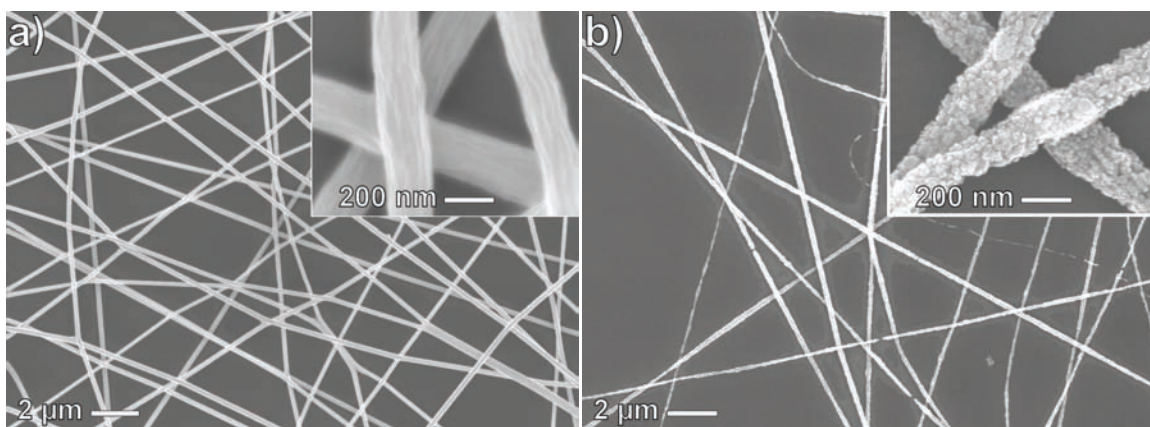


Figure 3-7: SEM images of nanofibers after calcination at 500°C : a) sol-gel-derived TiO_2 and b) commercial nanoparticles dispersion (primary particle size 20-30 nm)

Table 3-1: Surface area (according to the BET model) for nanoparticles and the resulting nanofibers

Preparation conditions	particle size [#] / nm	BET surface as-prepared / m ² g ⁻¹	BET surface [§] 500°C / m ² g ⁻¹	BET fibers 500°C / m ² g ⁻¹
sol-gel	n.a.	n.a.	36.7	58.5
80°C	6-9*	n.a.	69.7	57.8
110°C	10-12	240.2	127.3	133.4
110°C Tol	12-15	107.9	95.8	101.1
Aldrich	20-30	57.6	52.9	57.1

[#] as-prepared, estimated from TEM analysis * for the crystalline particle fraction

[§] prepared by heating the spinning solution to 500°C

As expected, there is a correlation between particle size and surface area (see Table 3-1), with smaller nanoparticles resulting in higher surface areas both in fibers and in particles calcined at 500°C. For the highly crystalline particles, almost no shrinkage or densification occur during calcination. In contrast, due to densification sol-gel-derived fibers are more compact and have a lower surface area. Similarly, the particles prepared at 80°C are rather amorphous and possess a low surface area after calcination.

Plotting the specific surface area for nanoparticles with bulk density from purely geometric considerations against the particle diameter underlines the influence of particle size (see Figure 3-8). The porous, particle-based nanofibers possess a slightly lower surface area, but especially for bigger particles the maximum theoretical surface area is nearly attained²⁹.

²⁹ Bulk density of 3.9 g cm⁻³ (anatase) and smooth spherical particles were assumed, thus probably underestimating the specific surface area.

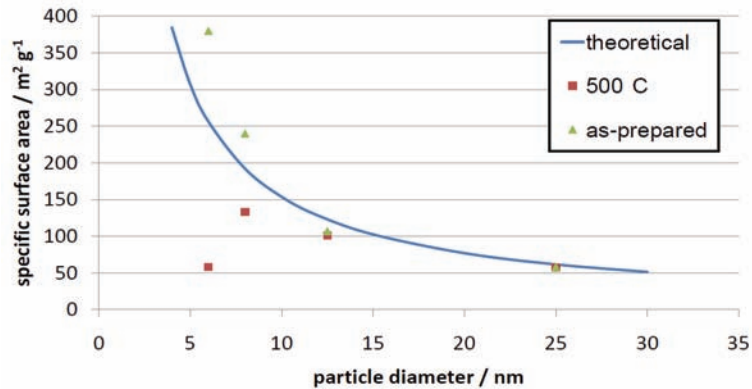


Figure 3-8: Specific surface area as function of particle diameter compared to obtained results for the nanoparticle-based fibers.

The larger BET surface area of the as-prepared particles must be interpreted with caution, as the particles were prepared at different temperatures resulting in different crystallinity and density, but also different amounts of amorphous TiO_2 and ligands.

XRD with Rietveld analysis shows that the crystallite size increases significantly upon calcination from 4 nm to 12-13 nm for the particles prepared at 80°C and 110°C (see Figure 3-9), in agreement with observations by Niederberger et al. [93]. In contrast, the bigger and more crystalline particles remain unchanged, as their crystallite size is already above 10 nm.

In conclusion, the nanoparticle-based fibers offer a well-defined hierarchical system with porosities 2-4 times higher than compact nanofibers. As such, non-woven TiO_2 mats are already of in-

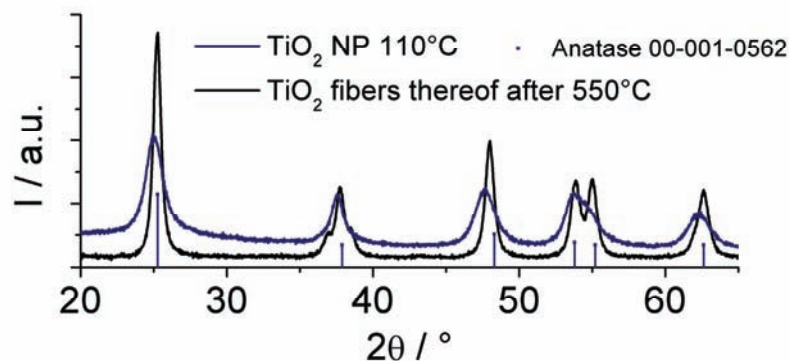


Figure 3-9: XRD analysis of TiO_2 nanoparticles as synthesized at 110°C before and after calcination at 500°C (with measured background)

terest for photocatalysis, but more importantly the crystallinity of the nanoparticles allows a new low-temperature synthesis using UV light as will be shown in the next section. Thereafter, the fiber mats will be employed as novel type of catalyst support by adding other nanoparticles or sol-gel precursors.

3.5 UV Synthesis, Photocatalysis and TiO₂(B)³⁰

Titanium dioxide is an n-type semiconducting oxide with several modifications, such as anatase, rutile and brookite occurring as minerals and some metastable forms like TiO₂(B).

Table 3-2: Modifications of TiO₂

Modification	crystal system	symmetry [#]	band gap[99]
rutile	tetragonal	P4 ₂ /mm	3.00 eV
anatase	tetragonal	I4 ₁ /amd	3.21 eV
brookite	orthorhombic	Pbca	3.13 eV
TiO ₂ (B)	monoclinic	C ₂ /m	3.05 eV

[#] data from: JCPDS PDF-2 Release 1998, International Centre for Diffraction Data

Due to its high chemical stability, TiO₂ has been extensively studied as photocatalyst³¹ after the discovery of water photolysis on rutile electrodes [100]. In general, anatase is considered to be the most photoactive crystal structure modification, although intimate mixtures of two modifications have been shown to be even more active [101].

Simplified, photocatalysis can be described as an excitation of electrons from the valence to the conduction band. The newly created hole acts as strong oxidation agent that can oxidize adsorbed organic molecules and even water. In aqueous solution the redox reaction is often mediated by hydroxyl radicals, whereas in the gas phase ozone can be generated.

A requirement for photocatalytic activity is the presence of crystalline material with a defined band structure that reduces the band gap compared to the atomic energy levels and that leads to a slow recombination of the exciton.

Many applications including air purification and removal of organic pollutants from water have been proposed for nano- and mesostructured TiO₂. However, the photocatalytic properties can also be exploited for low-temperature synthesis of TiO₂. For example, mesoporous TiO₂ for a solar cell was produced on ITO-coated polymer substrates by exposing a paste of TiO₂ nanoparticles and Ti(OiPr)₄ molecular precursor to UV radiation [102]. Thereby, ozone is generated and

³⁰ These results have been partially published [98].

³¹ Actually, the term “catalyzed photolysis” would be more appropriate than “photocatalysis”, as the reaction is only driven by light energy and catalyzed by a photoexcited semiconductor. However, the expression photocatalysis is more common and will be used here as well.

decomposes the organic ligands of the precursor. Moreover, the nanoparticles sinter together and the film is densified, as if a thermal treatment of several hundred degrees was applied.

This approach would be an elegant way to remove the spinning polymer without thermal treatment and although the relative amount of polymer is higher than in the thin films, the principle should also work for the nanofibers.

Whereas the as-spun nanoparticle-based fibers are obviously soluble in alcohols or water, an exposure to UV-C (wavelength below 280 nm) for 6 h produces inorganic, insoluble nanofibers³² (see Figure 3-10). In contrast, sol-gel derived fibers remain soluble after UV treatment.

As can be seen in the SEM images, the UV-prepared nanofibers are similarly porous to those thermally prepared. A detailed analysis is not easily possible, because the large-scale production of UV-treated fibers is not possible. When exposing a thick, free-standing mat of the fibers, only the upper layers of fibers are converted to inorganic fibers, while the UV cannot decompose the spinning polymer in the lower layers even after 30 h of treatment. Consequently, the fiber mats mostly dissolve when immersed in ethanol.

Although it is technically possible to repeatedly use only 2-3 μm thick mats, the low penetration depth of the UV is obviously a severe limitation to the UV-sintering approach.

However, for photocatalysis a mat with a thickness comparable to the penetration depth of the UV should be sufficient, as more catalyst material would not be sufficiently illuminated anyway.

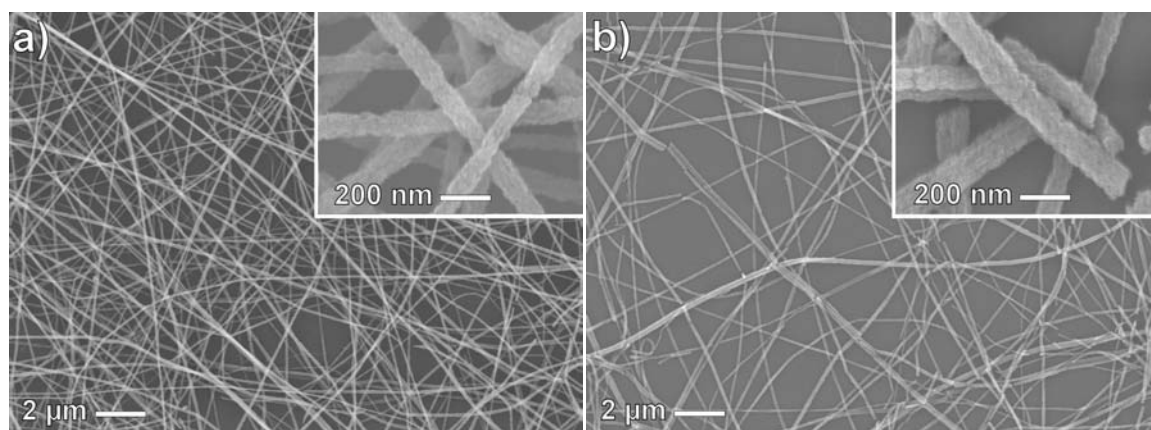


Figure 3-10: SEM images of nanofibers from PVP and TiO₂ nanoparticles synthesized at 110°C in benzyl alcohol/toluene a) after 6 h UV-C exposure and b) after additional washing with H₂O

³² The apparent breakup of several fibers after washing with water is due to the capillary forces during drying and is not observed after washing with EtOH.

After some photocatalytic tests of UV-sintered and thermally-annealed nanofiber mats, the activity was found to be similar for both and in the same range or lower than for mesoporous thin films³³. As photocatalysis of pure titania nanofibers has already been reported [103], [21] and this application is not the focus of this dissertation, no further optimizations were made.

Instead, the UV preparation technique was applied to fibers prepared from the TiO₂(B) modification that was shown to be highly active as photocatalyst [104] and that could recently be prepared as nanoparticles for the first time in ionic liquids³⁴. Their thermal conversion to anatase above 300°C is the main disadvantage of the nanoparticles of metastable TiO₂(B), making them an ideal platform for the UV preparation.

The as-prepared nanoparticles are not as well re-dispersible as the anatase particles and need to be functionalized with ethylene glycol or 1,3-propanediol to obtain stable nanoparticle dispersions without agglomerates.

As shown in Figure 3-11b, the highly crystalline nanoparticles do not sinter together well and the resultant fibers are discontinuous and particular. Close inspection reveals that the hybrid fibers of polymer and nanoparticles break down to lose particle aggregates upon polymer removal.

Therefore, 2.5 at% of Ti(OiPr)₄ relative to the TiO₂(B) are added to the spinning solution to act as a “glue” to connect the particles. Although the structure is not yet perfect, Figure 3-12b shows the significant improvement in the morphology of the resultant fibers that are continuous and develop the three-dimensional mat of free-standing fibers.

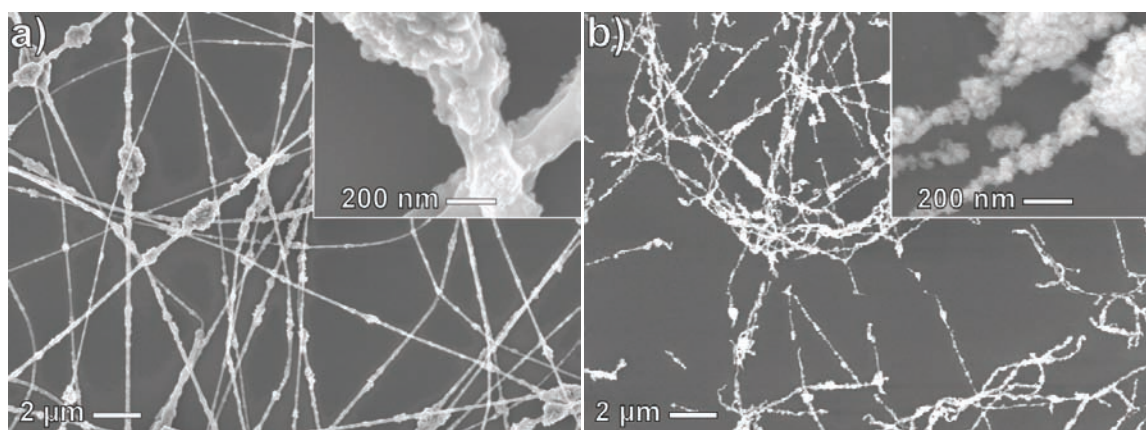


Figure 3-11: SEM images of nanofibers from TiO₂(B) nanoparticles a) as-synthesized with PVP and b) after 6 h UV-C exposure

³³ Tested by T. Lany – see corresponding M.A. thesis for details.

³⁴ The nanoparticles were kindly provided by S. Sallard.

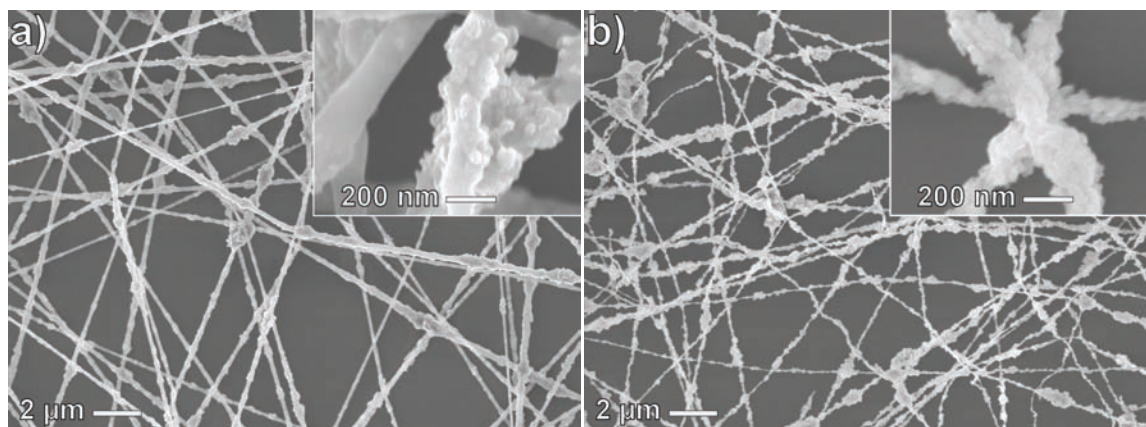


Figure 3-12: SEM images of nanofibers from TiO₂(B) nanoparticles functionalized with ethylene glycol and with additional 2.5 at% Ti(OiPr)₄ as “glue” a) with PVP b) after 2 h UV-C exposure

Moreover, the UV exposure time can be reduced to 2 h hinting at a very high photocatalytic activity. A detailed study of the photocatalysis is currently carried out³⁵.

One finding was universal to all the studies on photocatalysis: The mechanical properties of oxide nanofibers constitute a major obstacle in using them as catalyst in solutions. As the fibers are brittle, the constant liquid flow caused by the agitation ultimately breaks off small fragments that are dispersed in solution. While this might initially lead to an even better performance in photocatalysis, the fragments cannot be removed from solution easily and cause a loss of catalyst. To reduce the problem, more robust SiO₂ nanofibers³⁶ were electrospun on top of the TiO₂ fibers and allowed to evaluate photocatalytic performance.

In the next section, the nanofibers will be evaluated in gas-phase catalysis where they have been found to be perfectly stable.

³⁵ See bachelor's thesis of S. Urban for details.

³⁶ The amorphous SiO₂ nanofibers possess excellent mechanical properties.

3.6 Catalytic Three-Component Systems TiO₂:Ru and Pd

The nanoparticulate nature of the fibers does not only increase the specific surface area, but also allows mixing the nanoparticles with further components like catalytically-active metal nanoparticles. Whereas in sol-gel derived fibers the metal nanoparticles would be embedded into the compact fibers and only a fraction would be accessible, the situation in the particle-based fibers rather resembles a physical mixture of two types of nanoparticles with the catalyst being fully accessible. As the crystalline nanoparticles of the supporting oxide are only sintered together at the contact points, the metal nanoparticles are similarly bonded to the oxide or simply trapped inside the porous oxide.

Moreover, as shown in Figure 3-13 c) the nanoparticle-based fibers can serve as porous support for a thin catalyst layer in a one-step synthesis. The crystalline nanoparticles are simply the support for another oxide. For example, RuO₂ has proved to be an alternative catalyst that can replace platinum in NH₃ oxidation (Ostwald process) at lower temperature [105]. As will be shown in chapter 4, RuO₂ nanostructures like nanoparticles are more difficult to prepare, although nanofibers can be obtained by a sol-gel approach. Yet RuO₂ is not stable under the harsh reaction conditions of NH₃ and HCl oxidation (see chapter 4) and its already low specific surface area and activity are further decreased. As only a few layers of RuO₂ are required for the catalytic activity [106] and an increased stability of TiO₂-supported RuO₂ has been reported³⁷, it was attempted to coat the porous TiO₂ nanofibers with sol-gel-derived RuO₂.

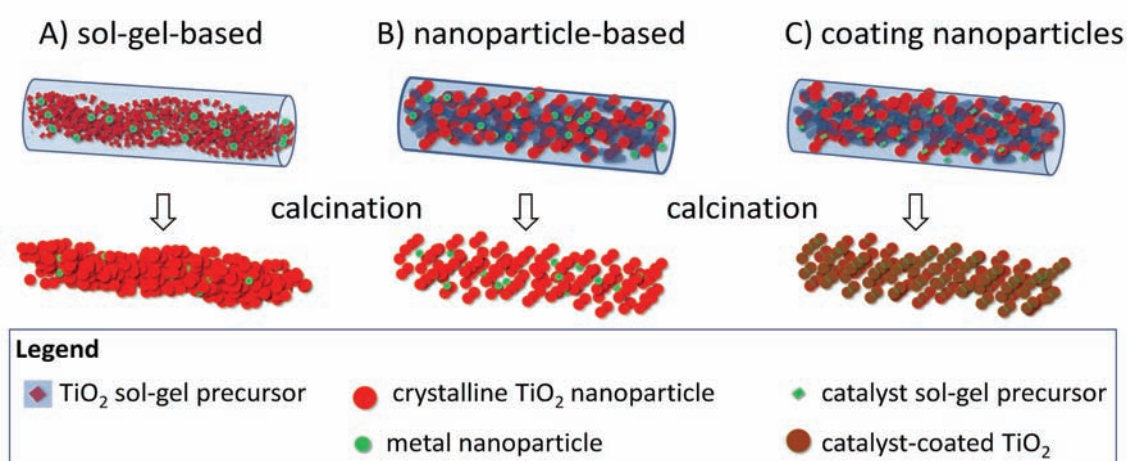


Figure 3-13: Scheme of catalytic nanofibers:

- a) sol-gel-derived compact fiber with metal nanoparticles inside
- b) nanoparticle-based porous fibers with metal nanoparticles
- c) nanoparticles surface-coated by adding a sol-gel precursor

³⁷ Sumitomo Ltd. developed a TiO₂-supported RuO₂ catalyst for the HCl oxidation.

Electrospinning allows to prepare hybrid nanofibers consisting of TiO₂ nanoparticles, a spinning polymer and the additional sol-gel precursor RuCl₃·H₂O. Upon calcination RuO₂ can form as homogeneous deposit on the TiO₂ particles or as individual nanoparticles. For oxides the first possibility is more likely and should lead to highly dispersed RuO₂ with excellent catalytic properties (see Figure 3-14).

In fact, porous RuO₂@TiO₂ fibers were obtained and as little as 1 wt% RuO₂³⁸ gave similar activities as bulk sol-gel-derived RuO₂ fibers (see Table 3-3).

Table 3-3: NH₃ to NO_x conversion at 400 °C for RuO₂ and RuO₂@TiO₂ fibers³⁹

fiber composition	mass / mg	conversion	after reduction [#]
pure RuO ₂	7.0	22%	43%
1% RuO ₂ @TiO ₂	6.4	23%	n.a.

[#] the fibers were reduced at 200°C under H₂/N₂ and reoxidized at 400°C

For a more detailed comparison of the dispersion and the reactivity, it would be necessary to quantify the surface area of the accessible RuO₂. In addition to physisorption with N₂ to obtain the total surface area, chemisorption of NH₃ or HCl that adsorb more specifically on the RuO₂

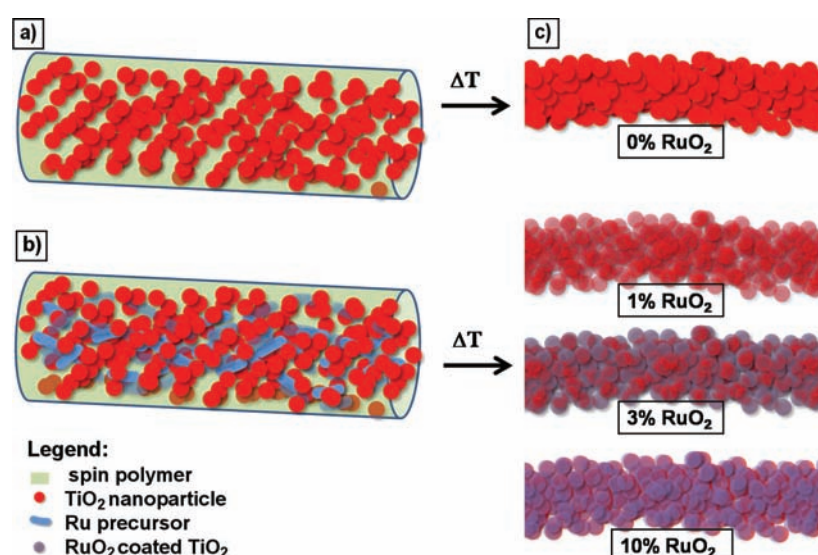


Figure 3-14: Scheme of fibers with surface-coated nanoparticles by adding of a sol-gel precursor: a,b) as-spun and c) after calcination

³⁸ Calculated from the amount of precursor used, EDX analysis confirms 0.4-0.7 wt% of Ru.

³⁹ The catalytic tests were performed by C. Kanzler and F. Hess.

could be used to characterize the catalytic material more precisely. Unfortunately, the necessary equipment for sorption measurements with corrosive gases was not yet available.

The outlined coating approach is not limited to nanofibers, but porous powders in general could be prepared similarly, either by flame pyrolysis or simply by drying with block copolymer templates and calcination. For RuO₂@TiO₂ it is possible to add a block copolymer (e.g. PEO-block-PIB) and obtain highly porous powders (BET surface of 168 m²g⁻¹ after calcination at 500°C) that should show good catalytic activity in HCl oxidation.

A further advantage of the nanofibers is their well-defined one-dimensional structure, making them an interesting system to study the stability and morphological changes of a catalyst under corrosive conditions. This special application of nanofibers as catalytic model system will be presented in chapter 4.

Returning to the nanoparticle-based fibers, another system was prepared by adding palladium nanoparticles [107] into the electrospinning solution of anatase nanoparticles (see Figure 3-15). The catalytic activity of the Pd nanoparticles is similar in fibers and mesoporous films and might be worthwhile to investigate under transport-limited reaction conditions to understand the influence of the catalyst morphology on its activity.

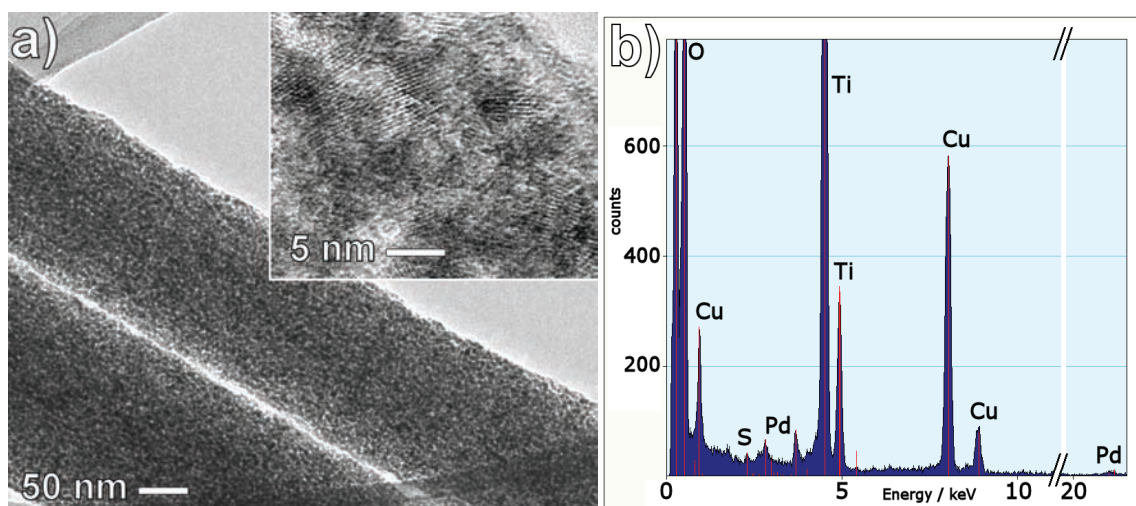


Figure 3-15: Porous TiO₂ Nanofibers prepared from nanoparticles of TiO₂ (2 h at 110°C) and Pd (1.5 wt%): a) TEM and b) EDX analysis (as the local TEM was broken, the pictures were kindly taken by E.Ortel, TU Berlin)

3.7 Hybrid MOF Fibers⁴⁰

As shown in this chapter, the use of crystalline nanoparticles as building blocks allows preparing nanofibers with interparticulate pores. The outer surface of particles becomes the internal surface of the fibers, with smaller particles leading to higher surface areas.

This approach is suitable for oxide nanofibers, as nanoparticles can be prepared from many metal oxides. However, oxide fibers are brittle and polymeric nanofibers are more appropriate for some applications like filtration, gas separation and storage. Especially for gas storage the lighter density of the polymers is favorable.

Yet in spite of various attempts, the preparation of porous polymeric nanofibers with high surface areas could not be realized so far.

Isotactic polymers like PLLA (poly-L-lactide) have been electrospun from solvent mixtures to produce porous fibers [109]. Similarly, polymer mixtures of PLLA and PVP (polyvinylpyrrolidone) have been electrospun, followed by the selective removal of one polymeric component [110], [111]. Another approach applicable to various polymers is to use a cryogenic liquid to trap some of the solvent inside the fibers, followed by an extraction of the solvent under reduced pressure to yield some porosity [112]. However, although their morphology seems quite porous, the specific surface area of such "porous" polymeric fibers is always quite low, usually in the range of 10-15 m²/g. As their surface area is only increased by a factor of 2-3 compared to the corresponding "non-porous" fibers, speaking of textured nanofibers would be more appropriate. Attempts to use inorganic templates like silica nanoparticles or GaCl₃ that can be selectively removed by etching in NaOH or dissolution in H₂O respectively, did not lead to a higher increase in surface area either [113], [114].

Only in inorganic or carbonized PAN (polyacrylonitrile) fibers sufficient microporosity can be found allowing for surface areas of up to 300 or 600 m²/g respectively [94], [115]. Highly porous polymers remain special cases with a high degree of (hyper)cross-linking like PIMs (Polymers of Intrinsic Microporosity)[116-118] and could not be prepared in form of nanofibers so far.

In contrast, metal organic frameworks (MOF) are crystalline coordination compounds that are well known for their extremely high porosity and surface areas [119]. The typical MOF structure consists of metal ions or metal ion clusters connected by rigid organic linker molecules. The synthesis is usually carried out under solvothermal conditions to enhance crystallinity.

Zeolitic imidazolate framework (ZIF) materials constitute a new subclass of MOFs that combine the properties of porous MOFs with high chemical and thermal stability [120]. Recently, Cravil-

⁴⁰ These results have been partially published [108].

lon et al. succeeded in preparing nanocrystals of a prototypical ZIF material, ZIF-8, that are 50 nm in size and have a rather narrow size distribution [121].

With a bulk density of 0.35 g/cm^3 for ZIF-8, the nanoparticles only possess a geometric (outer) surface of $4 \text{ m}^2/\text{g}$, but their total surface area can be up to $1300 \text{ m}^2/\text{g}$.

Dispersing such nanoparticles within polymeric nanofibers should dramatically increase the surface area of the composite fibers, if the nanoparticles remain accessible. As the ZIF-8 nanoparticles are prepared at room temperature and dispersion of 4 wt% in methanol can be obtained, it is possible to generate hybrid PVP-ZIF-8 nanofibers as free-standing mats via electrospinning. After the addition of the spinning polymer the nanoparticle dispersion becomes more stable and therefore some solvent can be evaporated under reduced pressure. One major advantage of the nanofiber mats is their “textile”-like form (see Figure 3-16), making them much easier to handle and separate than a nanopowder.

The diameter of the nanofibers could be adjusted by the polymer concentration and was found to be roughly 150-300 nm. The nanofibers can contain up to 55 wt% of ZIF-8 nanoparticles embedded in the polymeric matrix. TEM reveals a homogeneous distribution of the nanoparticles inside the fibers with a smooth polymeric surface (see Figure 3-17) and XRD confirms that the crystal structure of ZIF-8 is still intact (see Figure 3-18).



Figure 3-16: Digital photograph of a “textile” of PVP-ZIF-8 hybrid nanofibers

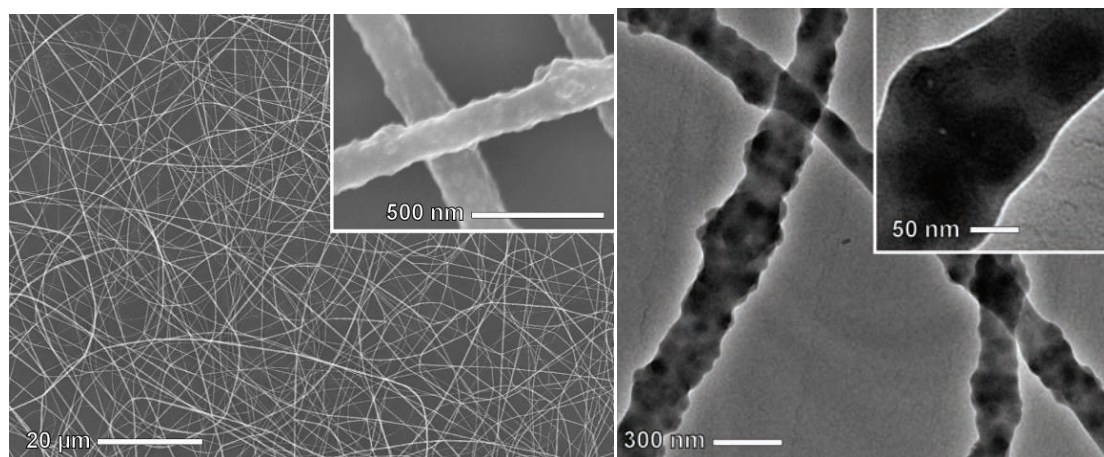


Figure 3-17: SEM (left) and TEM (right) of PVP-ZIF-8 hybrid nanofibers

From N_2 adsorption measurements with micropore analysis, the surface area according to the BET model was $962 \text{ m}^2/\text{g}$ for the pure ZIF-8, while the fibers possessed surface areas of up to $530 \text{ m}^2/\text{g}$ for a weight ratio of approx. 1:1 ZIF-8 to PVP. As can be seen in Figure 3-19, the adsorption branch for the fibers is shifted to higher pressure. The two steps on the adsorption isotherms that have been ascribed to pressure-induced adsorbate reorganization [122] are less pronounced, but still visible for the composite fibers. As can be seen from Table 3-4: Nitrogen adsorption data, for lower loadings of ZIF-8 the surface area decreased accordingly, proving the ZIF-8 nanoparticles to be fully accessible inside the polymeric nanofibers.

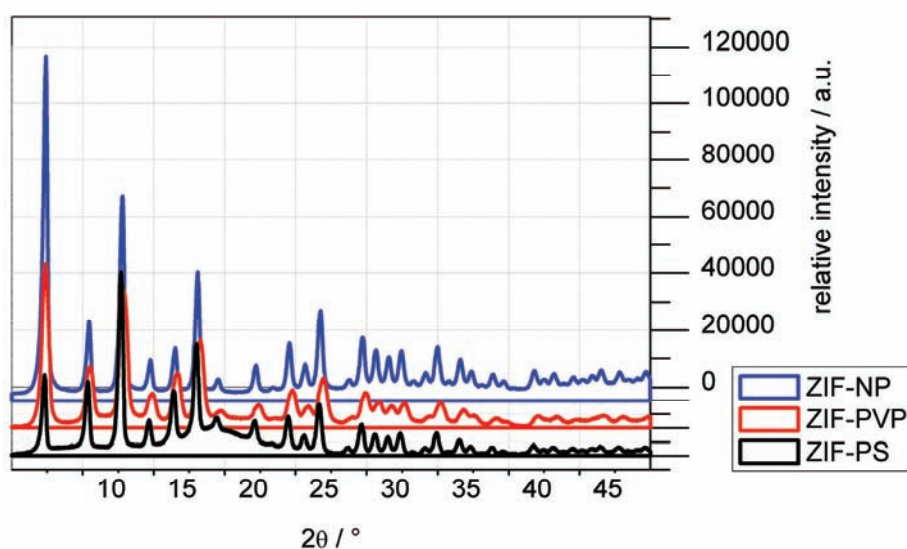


Figure 3-18: XRD of pure ZIF-8 nanoparticles and ZIF-8 inside PVP or PS

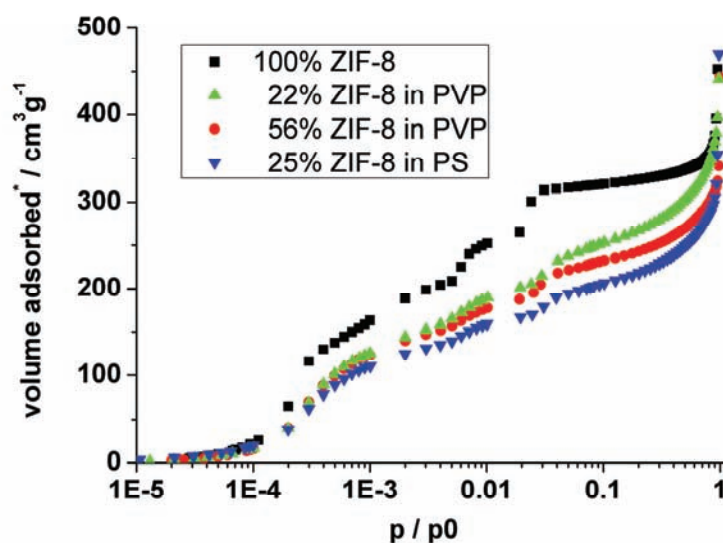


Figure 3-19: Nitrogen adsorption isotherms of ZIF-8 nanoparticles in PS and PVP (with different loadings of ZIF-8)

*for clarity, the desorption branch has been omitted and the curves have been scaled to 100% ZIF-8 content.

The results from N₂ adsorption measurements can be summarized as follows:

Table 3-4: Nitrogen adsorption data

Sample	ZIF-8 concentration ¹	micropore volume	surface area ²	ZIF-8 concentration ²
ZIF-8	100 wt%	0.4866 cm ³ /g	962 m ² /g	100 wt%
ZIF-8 in PVP	56 wt%	0.1779 cm ³ /g	530 m ² /g	55.1 wt%
ZIF-8 in PVP	22 wt%	0.0733 cm ³ /g	184 m ² /g	19.1 wt%
ZIF-8 in PS	25 wt%	0.0694 cm ³ /g	209 m ² /g	22.7 wt%
PVP only	0 wt%	< 0.0022 cm ³ /g	10 m ² /g	n/a

¹: as weighed in ²: according to the BET model

The nanofibers are stable as-prepared up to 150°C and in organic solvents, but sensitive to solvents of the polymer like alcohol or water, causing the nanofibers to coalesce with a complete loss of surface area.

Other polymers like polystyrene (PS) are insoluble in polar solvents and insensitive to humidity, therefore it would also be desirable to obtain PS-ZIF-8 nanofibers. A suitable approach was found by exchanging the solvent of the ZIF-8 dispersion from pure methanol to a mixture of THF (tetrahydrofuran), toluene and methanol with a weight ratio of 4:1:1. PS (MW = 240,000) can be dissolved in this solution at sufficient concentrations (approx. 8 wt%) for electrospinning. To increase the conductivity of the solution 0.2 wt% tetra-butylammoniumperchlorate needs to be added, before electrospinning at a flow rate of 0.65 ml/h at a voltage of 5 kV.

The resulting PS-ZIF-8 nanofibers are stable in alcohols and water and the surface area is fully accessible, even if the ZIF-8 loading up to 25 wt% is slightly lower (see Figure 3-20). Higher loadings should be possible by tuning the synthesis parameters and functionalizing the surface of the ZIF-8 nanoparticles with less polar molecules.

Moreover, polyethylene oxide (PEO) can also serve as carrier polymer, but the resulting fibers are very sensitive to humidity and temperatures above 60°C can cause fusion of the fibers leading to much lower accessibility of the MOF nanoparticles inside the fused polymer film.

This shows that it is important to choose the appropriate polymer, as polystyrene fibers offer tolerance to polar solvents and thermal stability up to 100°C, whereas PVP nanofibers are more sensitive to solvents, but stable up to 150°C. As electrospinning is possible for many polymers, it should be possible to find a suitable one.

The coalescence of the fibers by heat or solvents also demonstrates the major advantage of the hybrid nanofibers: Whereas in a bulk hybrid a thick polymer film severely limits gas adsorption in the ZIF-8 particles, in the hybrid nanofibers no loss in accessible surface area is observed.

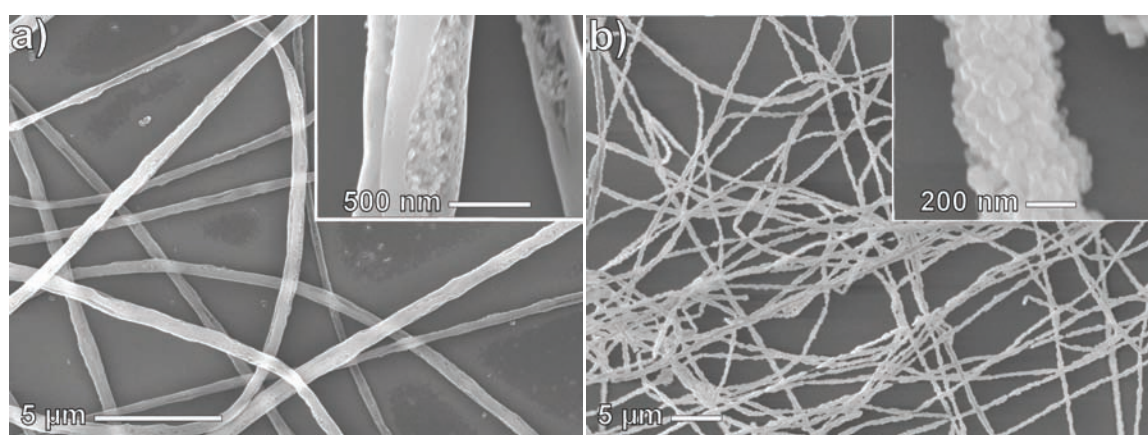


Figure 3-20: SEM of a) PS-ZIF-8 and b) PEO-ZIF-8 nanofibers

Yet the thin polymer layer that covers the particles in the fibers should constitute some diffusion barrier and therefore the kinetics of adsorption were investigated. The Autosorb-1 instrument can actually be controlled manually and a precise volume of adsorbate gas with defined pressure can be released into the evacuated sample cell. The gas is adsorbed inside the sample and the corresponding decrease in pressure is monitored and recorded with a self-programmed software tool.

Thus, as shown in Figure 3-21, the adsorption kinetics of the nanofibers could be compared to bare nano- and microparticles (hydrothermal synthesis yields particles with diameters of 2-5 μm). Due to the polymer layer, the nitrogen uptake of the fibers takes 3-4 x the time of the nanoparticles, but is still as fast as for the microparticles.

In any case, it would be desirable to conduct a more systematic study addressing the question how the morphology of the ZIF-8 (bulk, nanoparticles, nanofibers) affects the adsorption kinetics especially for more relevant adsorbates like hydrogen, carbon dioxide or monoxide. Different carrier polymers and the degree of nanoparticle coverage by the polymer should also influence the adsorption and might allow tuning the selectivity of adsorption.

As first step, the results from N_2 adsorption were corroborated by room-temperature measurements with CO_2 at higher pressures (see Figure 3-23).

Interestingly, the CO_2 adsorption kinetics of the hybrid nanofibers are much faster than those of the microparticles (see Figure 3-22). Taking into account the 10-20 times higher permeability

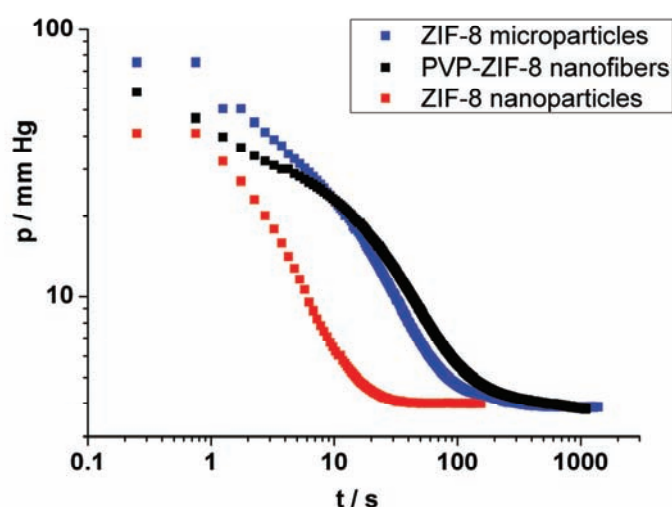


Figure 3-21: Adsorption kinetics studied as cell pressure over time

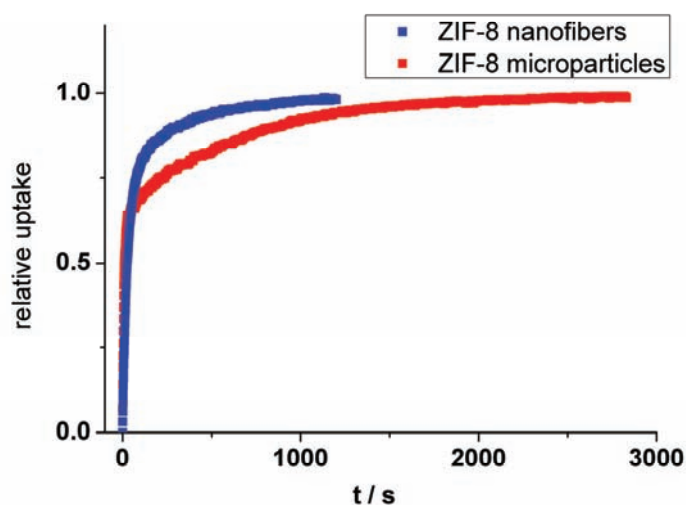


Figure 3-22: CO₂ adsorption kinetics of ZIF-8 nanoparticles in PVP and ZIF-8 microparticles

of CO₂ compared to N₂ in most polymers [123], it seems that the diffusion of CO₂ inside the microparticles is slower than through the polymeric skin of the nanofibers.

Actually, partially uncovered nanoparticles or a thinner layer of spinning polymer should result in even better kinetics. Therefore, another approach would be to exploit the positive zeta-potential of the nanoparticles to adsorb them onto fibers.

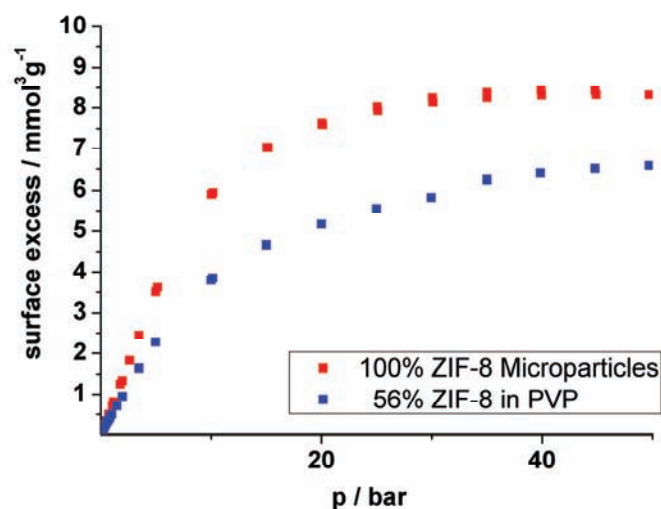


Figure 3-23: CO₂ adsorption isotherms of ZIF-8 nanoparticles in PVP and ZIF-8 microparticles

It is possible to treat nanofibers of PS (polystyrene) with conc. H_2SO_4 to functionalize the surface with sulfonate groups, thereby creating an anionic polyelectrolyte as described in the literature [124]. Using their positive surface charge, the ZIF-8 nanoparticles could then be adsorbed. However, the loading of ZIF-8 and the stability were quite low, even after a layer-by-layer adsorption by alternated immersion of the fibers in ZIF-8 dispersion and a solution of the anionic polyelectrolyte PSS (polystyrenesulfonate). Therefore, this approach was not developed further.

In conclusion, nanofibers of a metal-organic framework could be prepared for the first time by electrospinning preformed nanoparticles, thereby creating hierarchical nanofibers with extremely high surface areas and good accessibility. With the anticipated availability of other MOF materials as nanoparticles, a broad variety of MOF nanofibers should be accessible and result in various applications, for example in gas adsorption and separation. Due to their low resistance to fluid flow, the nanofiber mats could ultimately be useful to selectively adsorb specific gases, for example carbon monoxide in gas masks.

Chapter 4 – Novel Sol-Gel Nanofibers

4.1 The Purpose of Sol-Gel Nanofibers

Adding sol-gel precursors to the solution of a carrier polymer is the most straight-forward approach to obtain metal oxide nanofibers by electrospinning. Although it was shown in the last two chapters that sol-gel-derived fibers have some limitations with regard to porous or doped oxides and stability of the spinning solution, there are several advantages:

- **Simplicity:** Using a suitable solvent and carrier polymer, many oxides can be prepared from the respective alkoxides or other uncharged precursors
- **Complexes phases:** Ternary or quaternary oxides can be obtained
- **Phase control:** Assuming miscibility of precursor and polymer, homogeneous nanofibers can be produced with a “perfect” mixing of the components in a one-dimensional confinement

In this chapter, it will be further shown how co-solvents and heat treatments allow widening the range of precursors to nitrates and chlorides that are more readily available than alkoxides. Interestingly, the formation of hollow fibers can be observed and this finding is rationalized.

Moreover, electrospinning sol-gel solutions can produce complex phases like BFTO and allows for phase control in titania nanofibers, i.e. addition of 10 at% reproducibly yields rutile instead of anatase TiO_2 .

4.2 Electrospun RuO₂ for Heterogeneous Model Catalysis

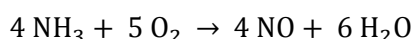
As pointed out in chapter 3, especially porous nanofibers are a suitable system for gas-phase heterogeneous catalysis, as their hierarchical structure allows efficient mass transport.

Catalysis is of paramount importance for a modern economy, as catalyzed reactions are involved in the production of 85-90 % of all chemicals, tuning the selectivity and increasing the yield of desired products [125]. By reducing the demand in energy and raw materials, catalysis contributes to both economic efficiency and ecologic sustainability of processes in the chemical industry. In addition to their use in production, catalysts are often employed to recover and recycle side-products and waste, or at least to effectively decompose toxic waste, like noxious exhaust fumes, to less harmful substances.

There are three key properties of every catalyst:

- activity, i.e. the rate of conversion
- selectivity, i.e. the yield of the desired product over all possible products
- stability, i.e. the conservation of activity over time

Whereas most fundamental studies focus on improving the activity and selectivity, the stability of a catalyst is often viewed as the deactivation over time due to the formation of coke and other residues. As the catalyst itself remains unchanged, it can be reactivated by thermal treatment for example. However, under harsh reaction conditions the catalyst itself can deteriorate or be removed. A prominent example is found in the Ostwald process, i.e. the catalytic oxidation of NH₃ to NO_x on platinum wires at 1000-1200 K [126]:

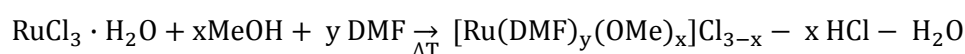


Although the Rh-stabilized Pt gauzes catalyze the reaction with great efficiency and selectivity, regular replacements of the Pt are necessary, as it is corroded with the formation of volatile PtO₂ [127]. The electrospun Pt nanofibers were briefly considered as high-surface Ostwald catalyst, but as shown in chapter 2 their nanofiber morphology is only stable up to 900 K.

A low-temperature alternative was recently reported, as single crystalline RuO₂(110) allows the selective oxidation of ammonia at 530 K under UHV (ultra high vacuum) conditions [105] and a detailed reaction mechanism has been proposed [106].

Although mechanistic studies of catalytic reactions are beyond the scope of this thesis, the use of nanofibers as one-dimensional⁴¹ model system should be interesting to bridge the gap between single-crystal surfaces and real-world powder catalysts. In contrast to RuO₂ powders, the well-defined morphology of the nanofibers (see Figure 4-1) seems well-suited to investigate the possible corrosion of the catalyst.

As there are no reports in the literature to prepare RuO₂ nanofibers by electrospinning, a novel sol-gel approach was developed. Attempts with Ru(acac)₃ as precursor failed due to the sublimation of this compound, whereas RuCl₃·H₂O leads to poor electrospinning due to the ionic character of the precursor. Finally, it was found that addition of DMF and heating the solution to 125°C lead to the formation of DMF complexes and expel some HCl gas.



Other than detecting HCl, this schematic equation or the composition of the complex has not been verified, but the formation of similar Ru-DMF complexes was already reported [128].

Surprisingly, nanotubes are reproducibly obtained from the Ru-DMF complexes with PVP (poly-

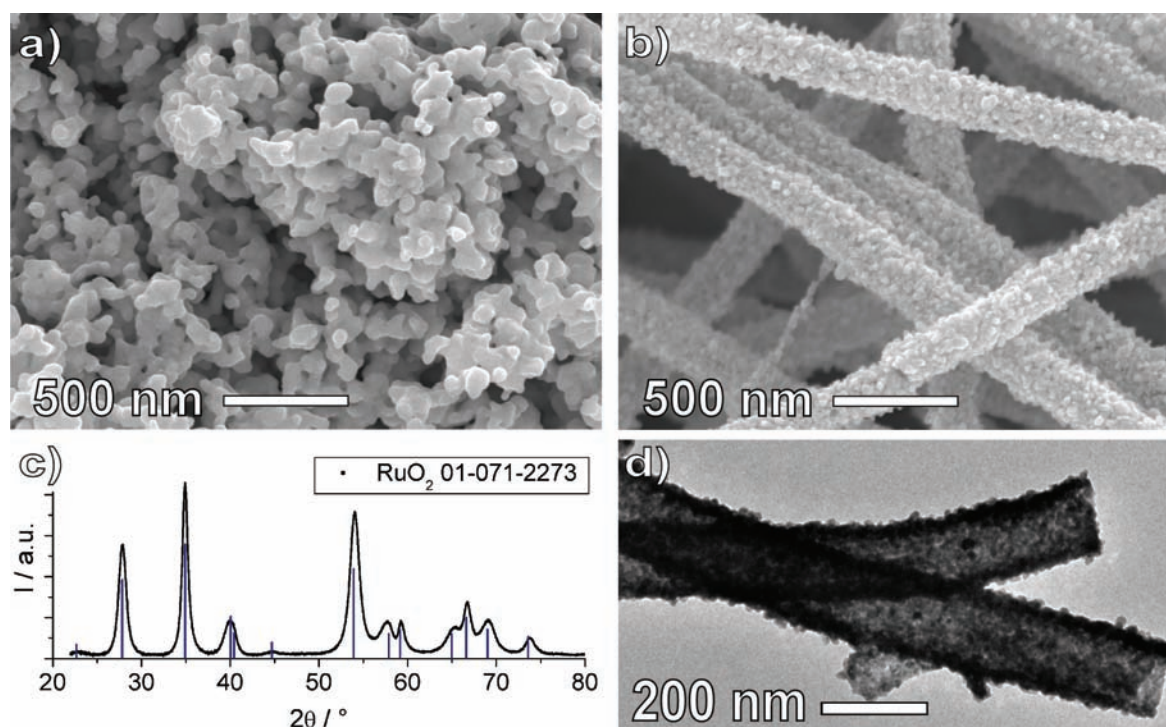


Figure 4-1: Comparison of RuO₂ a) commercial nanopowder and b) nanotubes as-prepared with corresponding c) XRD and d) TEM

⁴¹ One-dimensional refers to the meso- and macroscopic morphology, i.e. the fiber shape. For catalysis the microstructure (crystal facets, defects, etc.) is even more important, but it cannot be controlled by electrospinning. The preparation conditions (temperature, composition, etc.) might influence the microstructure and are therefore kept constant.

vinylpyrrolidone) as spinning polymer. A detailed formation mechanism and the extension to Fe₂O₃ and Co₂O₃ will be presented in the next section (see chapter 4.4).

For the model catalysis experiments in collaboration with the group of Prof. Over, these tubes present an even better system to study morphology changes.

The nanotubes were prepared at sufficiently high temperature to consist only of RuO₂ nanocrystallites sintered together to form a well-defined hollow morphology. The crystallite size is about 9 nm according to Rietveld analysis and the tubes possess a diameter of 200-250 nm with a wall thickness of 30-40 nm. The BET surface area from N₂ adsorption is 25-35 m²/g.

During the catalytic tests in the group of Prof. Over⁴², the tubes showed activity and selectivity towards ammonia oxidation similar to the commercial nanopowder.

Although detailed investigations of the catalytic behavior are beyond the scope of the thesis, it can be shown from SEM images that the nanotubes are stable at 573 K (see Figure 4-2 b) and only minor recrystallization into RuO₂ single-crystal nanoparticles occurs at 673 K. The morphological stability corresponds to stable catalytic activity.

However, in contrast to the results from the UHV study on RuO₂(110), where the selectivity towards NO_x (over N₂O and N₂) was found to be over 90% at 530 K [105], the selectivity only attains about 45% for the nanotubes (as well as the nanopowders) at 673 K. An explanation might be found in the presence of other RuO₂ facets due to the polycrystalline nature of the tubes and in the higher pressure, favoring the formation of N₂O and N₂.

Nevertheless, the nanotubes can be useful to investigate the catalyst's stability under harsh reaction conditions. This was further demonstrated by using the nanotubes as model catalyst for HCl oxidation.

Hydrogen chloride is a by-product of the chlorination of organic molecules and the recovery via electrolysis is energy-consuming. The Deacon process, i.e. the direct oxidation of HCl to Cl₂ was already demonstrated by H. Deacon in 1868 [129], but the application suffered from instability of the catalyst and technical issues with the corrosive gases. Recently, a Deacon-type process has been realized for TiO₂ supported RuO₂ [130].

⁴² The catalytic tests were performed by C. Kanzler and F. Hess.

Therefore, the catalytic activity and the stability of the RuO_2 nanotubes have been tested for HCl oxidation and already at 573 K massive recrystallization occurs. Nonetheless, the catalytic activity remains almost constant (see Figure 4-2 d), indicating that the recrystallization does not reduce the catalytically active surface area. A possible explanation might be that the stable $\text{RuO}_2(110)$ is formed predominantly. While a detailed analysis of the catalytic properties, especially at higher temperatures, is still under investigation by our collaborators, a morphological instability of pure RuO_2 in HCl oxidation could already be demonstrated. Therefore, mixed Ru-Ti oxides and supported RuO_2 will be considered in chapter 4.5.

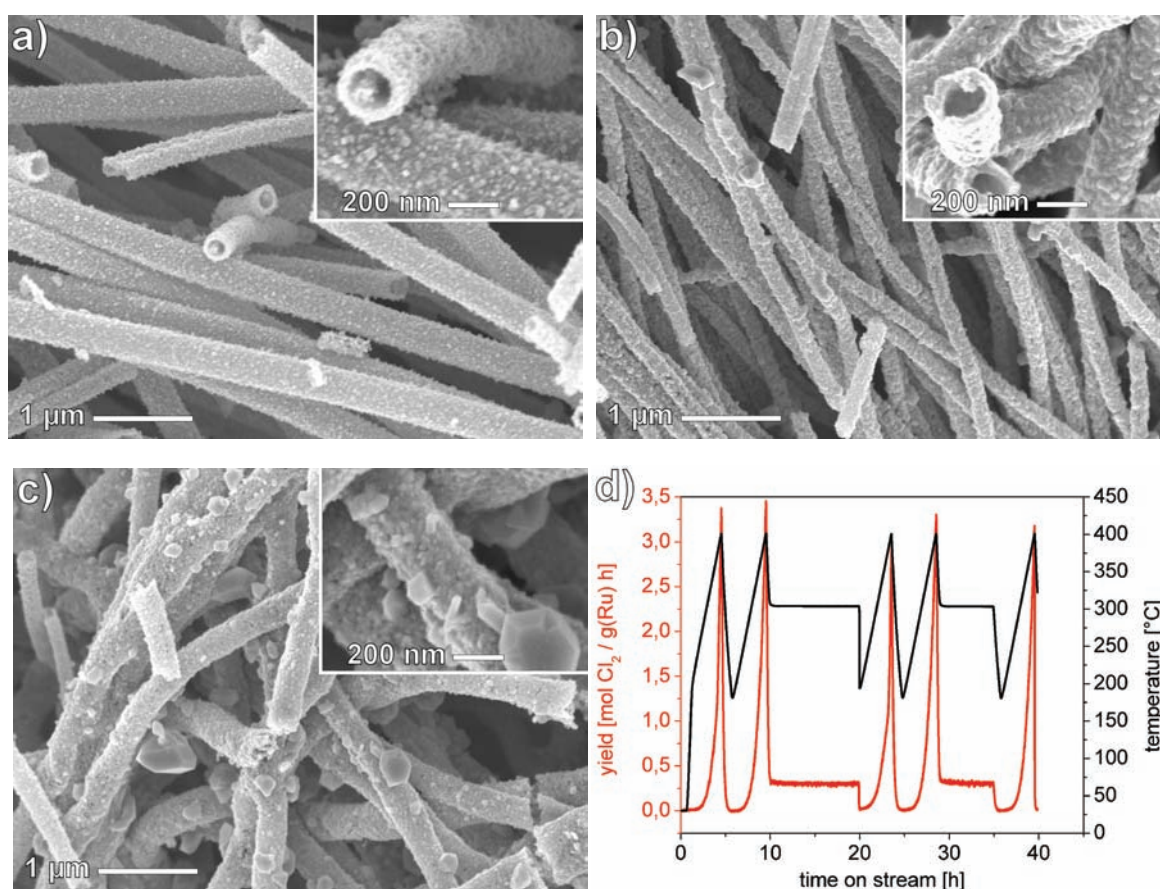


Figure 4-2: Comparison of RuO_2 nanotubes:

- as-prepared at 475°C
- after NH_3 oxidation at 673 K for 70 h
- after HCl oxidation at 573 K for 5.5 h
- yield in HCl oxidation as function of temperature

4.3 Hollow Nanotubes

The unexpected tube formation for RuO₂-PVP nanofibers has not yet been reported in the literature, although hollow nanotubes could be prepared from various metal oxides by coaxial electrospinning [131], [132]. Two immiscible spinning solutions are fed coaxially through the syringe and an inner capillary to obtain nanofibers with core-shell morphology (see Figure 4-3). After removal of the core, hollow nanotubes can be obtained [131].

However, for the preparation of RuO₂ nanotubes a single syringe is used and the solution does not contain any immiscible components. As elaborated in chapter 3.2, phase separations are unlikely to occur during the fast electrospinning process that leads to rapid solidification of the fibers. A core-shell morphology is only found, if two phases were present initially as in coaxial or in emulsion electrospinning. By using emulsions, for example two immiscible polymers in a common solvent, core-shell nanofibers can be obtained from a single syringe, as demonstrated for PMMA (Poly(methyl methacrylate)) and PAN in DMF [91]. In principle, there are already two phases present in emulsion electrospinning, a continuous phase with the polymer and the dispersed droplets of the second phase (typically with diameters of a few micrometers). During the electrospinning process the emulsion is subjected to high shear forces in the Taylor cone and in the emerging fiber that result in a core-shell morphology (see Figure 4-4).

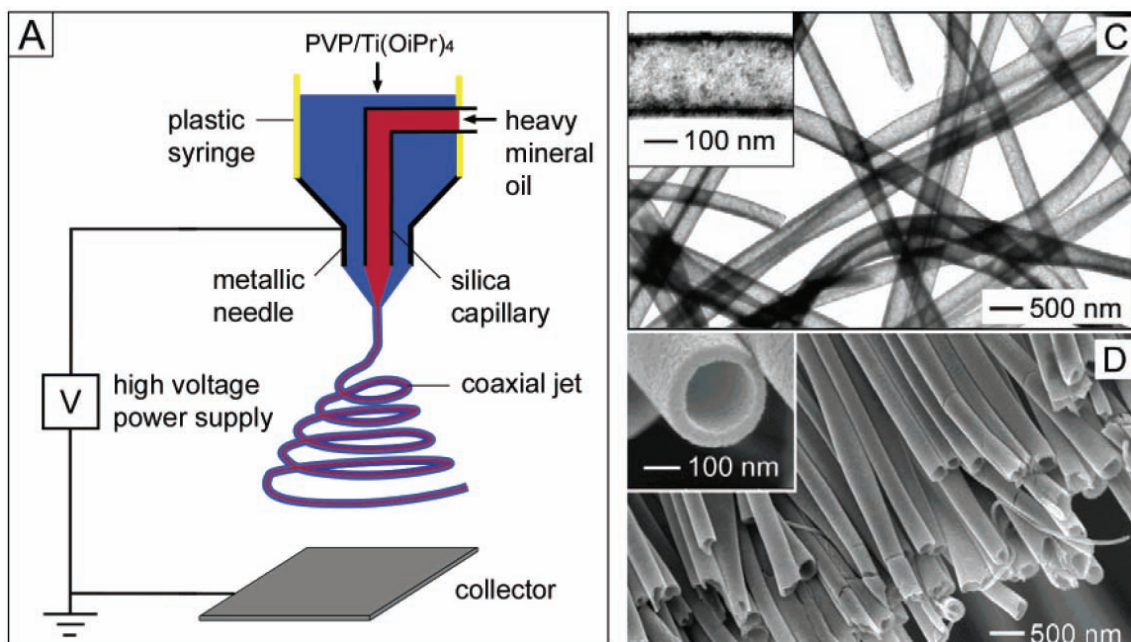


Figure 4-3: Coaxial electrospinning setup: A) scheme, C) TEM and D) SEM of hollow TiO₂ nanotubes prepared from PVP/sol-gel precursor [131]

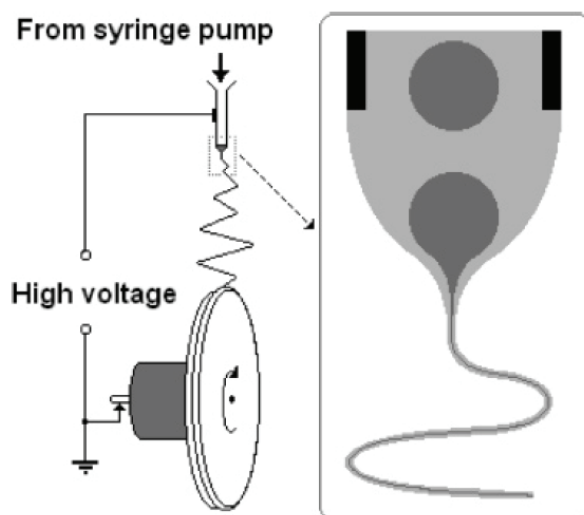


Figure 4-4: Principle of emulsion electrospinning [91]

In contrast, the spinning solution of Ru-DMF complex⁴³ with PVP in methanol or ethanol is a perfect solution and no phase separation is observed over time or even upon drying. Furthermore, only homogeneous compact fibers can be noticed in TEM up to 300°C. Therefore, the composition of the fibers seems rather homogeneous⁴⁴ throughout the cross section (see Figure 4-5).

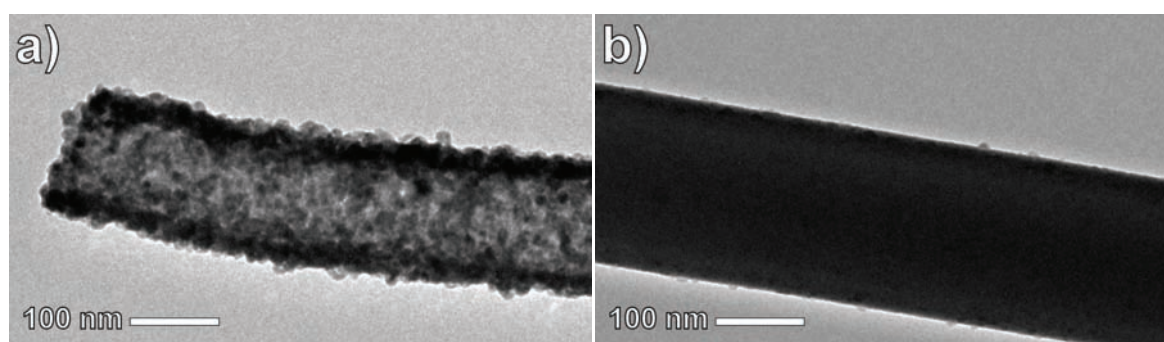


Figure 4-5: Comparison (TEM) of RuO₂ nanofiber after 1 h at a) 450°C and b) 250°C with the spinning polymer still present

⁴³ Obtained by heating RuCl₃·H₂O to 125°C in DMF.

⁴⁴ At least, there is no distinct core-shell morphology, a gradual shift from a (hydr)oxide-rich shell to a polymer-rich core cannot be excluded from TEM.

Apparently, the relative humidity has a major influence on the formation of the tubes. A low humidity is beneficial to electrospinning in general, as at humidities above 40% water can condense on the fibers and the evaporation of the solvents is slowed down, ultimately leading to poor spinning with a break-up of the fibers. For the formation of the nanotubes, a relative humidity below 20% seems necessary, as otherwise the tubular morphology is less pronounced. Moreover, the addition of 1 wt% of water to the spinning solution results in completely dense fibers (Figure 4-6).

Therefore, a mechanism can be proposed as follows:

The Ru-DMF complex is rather stable and soluble up to 5 wt% in PVP-DMF-MeOH with a lower ratio of Ru complex to PVP giving better-defined tubes. During electrospinning homogeneous nanofibers of the complex in PVP are obtained. Upon exposure to humidity or heat the complex is transformed into ruthenium hydroxide or RuO_2 on the surface of the fibers, while the concentration of Ru in the core is decreasing, leading to a radial concentration profile in the fibers with the Ru concentration decreasing towards a polymer-rich center. Moreover, PVP is known to crosslink under UV or thermal treatment into an insoluble cross-linked PVP [133] that might also lead to a polymer-rich core and an oxide-rich shell of the fibers. Upon calcination the oxide forms a stable shell, while the polymer is completely decomposed leaving behind the nanotubes.

Actually, the PVP seems to play a crucial role, as other polymers like polyvinylbutyral (PVB) or polyethylene oxide (PEO) only form highly porous fibers upon calcination (see Figure 4-7).

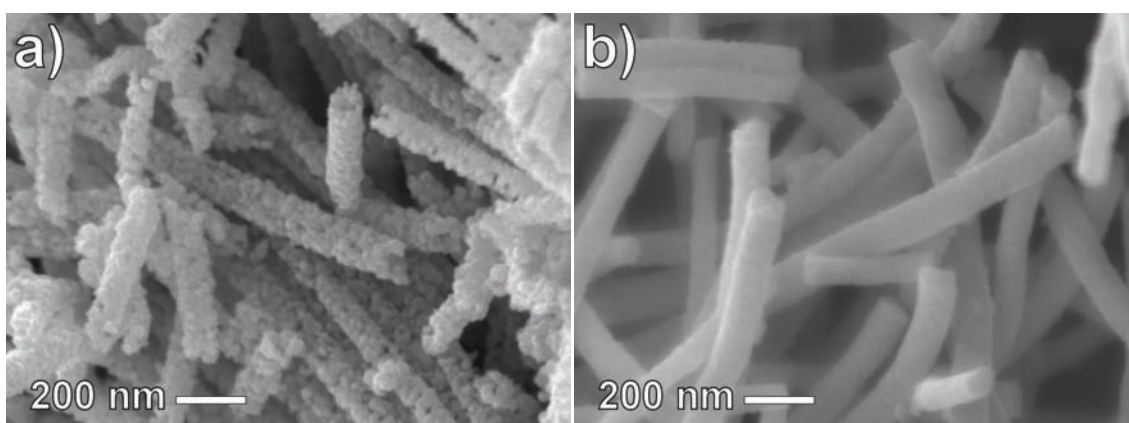


Figure 4-6: Comparison of RuO_2 electrospun from PVP a) at relative humidity of 40% and b) with 1 wt% H_2O

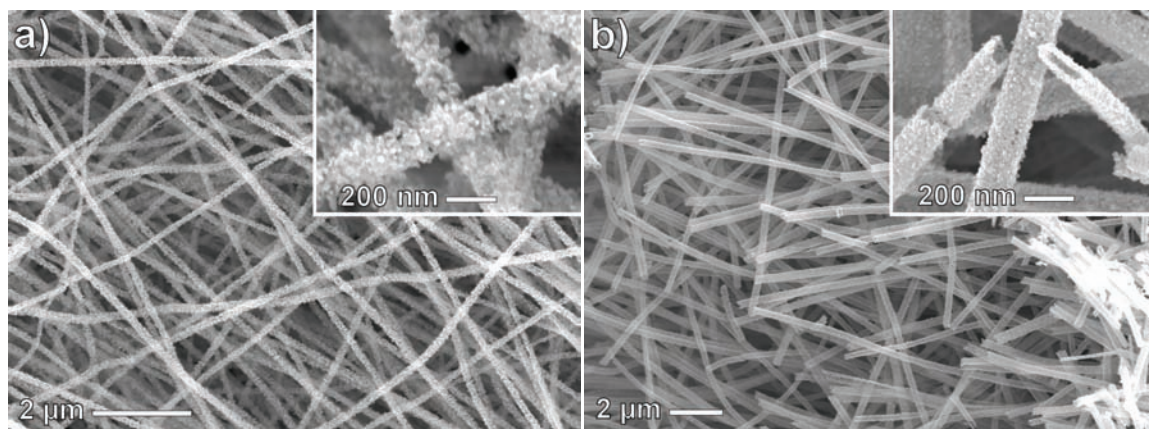


Figure 4-7: Comparison of RuO₂ electrospun from a) PVB and b) PVP

The formation of the nanotubes will be further investigated in the next section, especially elucidating the role of PVP and DMF and the new preparation method will be generalized to other oxides.

4.4 Extension to Other Oxides and First Mechanistic Insights

To gain more insight into the formation mechanism, it was attempted to generalize the hollow nanotubes to other oxides and to understand the interplay of the components. The same method only resulted in compact nanofibers for SiO₂ and TiO₂, whereas nanotubes of Co₂O₃, NiO, and especially Fe₂O₃ could be prepared.

The higher charge density is the main difference between Ti⁴⁺ or Si⁴⁺ and the di- and trivalent cations that lead to the hollow oxide nanotubes. Although the preparation is non-aqueous, the hydrolysis by ambient humidity can play a significant role. Even in acid solution the hydrolysis equilibrium



is much further on the right side for tetravalent cations that form hydroxides and oxohydroxides more readily, ultimately leading to condensation through ololation and oxolation [45]. For example, electrospun SiO₂ fibers are hydrolyzed and condensed by an ambient humidity above 10% to become insoluble. In contrast, up to medium pH-values divalent and most trivalent cations are known to form stable aqueous solutions with aqua complexes M(H₂O)_n rather than hydroxides. Replacing the aqua ligands with DMF produces complexes that are even more stable against condensation, whereas for tetravalent cations bidentate ligands like acetylacetonate are necessary to significantly slow down condensation [45].

Similarly to RuCl₃·H₂O as precursor for the RuO₂ tubes, the precursors for the cobalt, nickel and iron oxides were hydrated nitrates and chlorides, more specifically Co(NO₃)₃·6H₂O, NiCl₂·6H₂O, and Fe(NO₃)₃·9H₂O that were heated to 125°C in DMF to remove most water (see Figure 4-8).

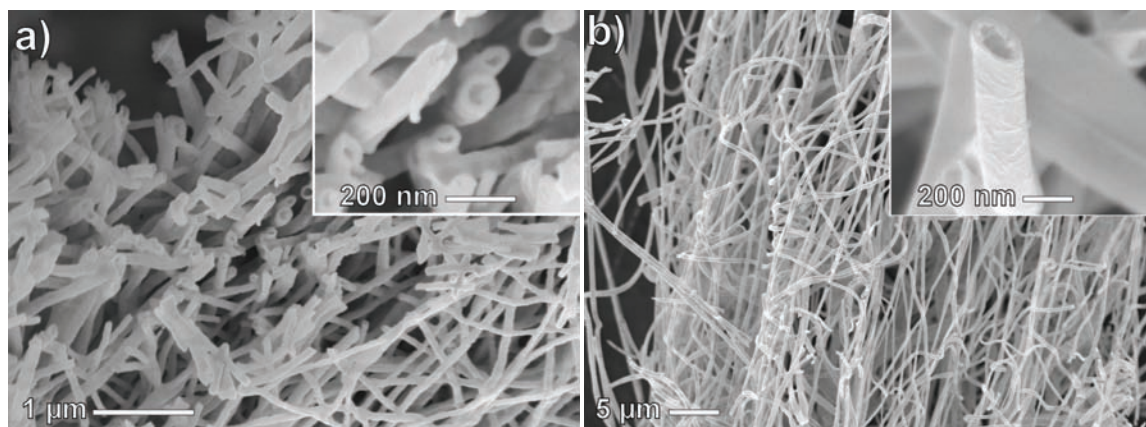


Figure 4-8: Nanotubes of a) Co₂O₃ and b) NiO obtained after calcination at 425°C from PVP and the corresponding DMF complexes

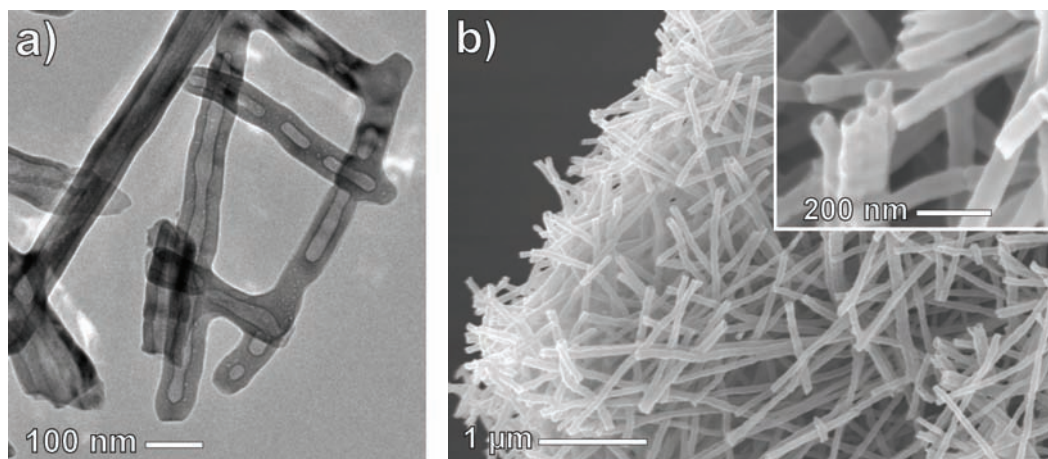


Figure 4-9: a) TEM and b) SEM images of nanotubes Fe_2O_3 obtained after calcination at 425°C from PVP and the iron-DMF complex prepared from $\text{Fe}(\text{NO}_3)_3 \cdot 9\text{H}_2\text{O}$

The nanotubes possess a diameter around 100-200 nm and as they are prepared from highly hydrated precursors (compared to $\text{RuCl}_3 \cdot \text{H}_2\text{O}$), it is likely that the electrospinning solution still contains some water even after heating at 125°C . Therefore, the nanotubes are not perfectly developed and contain some compact sections as can be seen in Figure 4-9.

Using anhydrous FeCl_3 as precursor and an even lower Fe to PVP ratio, well-defined nanotubes with a diameter of 150-200 nm and a wall thickness of 20-25 nm are obtained (see Figure 4-10).

The mechanism of the proposed self-templating process is further elucidated by these results confirming that the carrier polymer acts as template during calcination and that the oxide forms as a rough layer on the surface of the fibers. In contrast, the as-spun composite fibers of smaller diameter possess a smooth surface before calcination. Moreover, the inner surfaces of the tubes

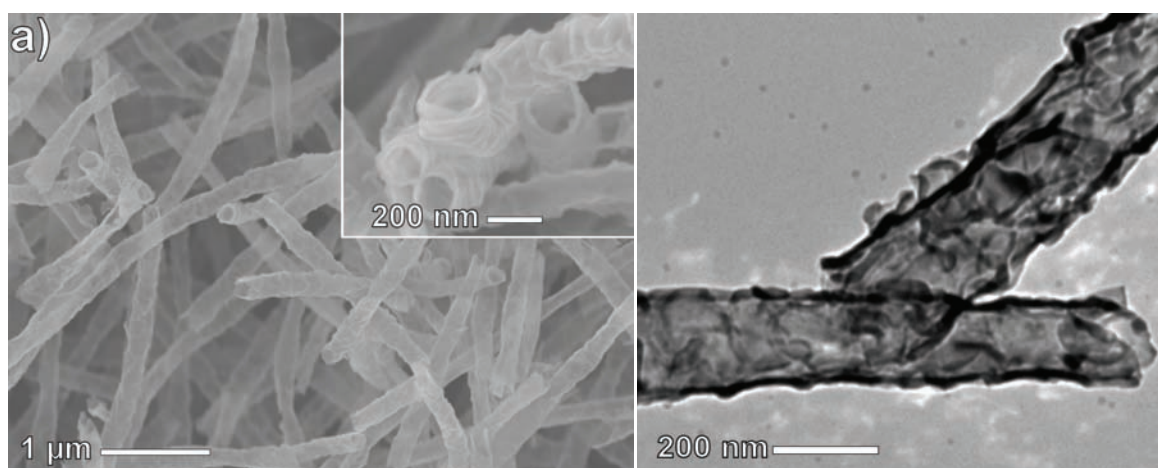


Figure 4-10: Nanotubes of Fe_2O_3 from PVP- FeCl_3 a) SEM and b) TEM

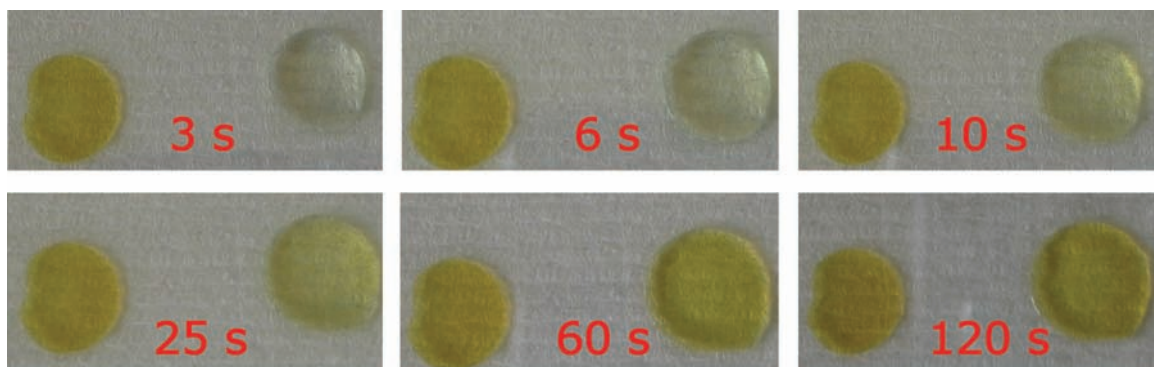


Figure 4-11: Evolution of Fe-PVP-DMF spinning solution after 1 day in a sealed vial (clear solution) when exposed to humid air (the left drop has been under air for 5 min)

are remarkably smooth.

In addition to the reasons mentioned before, the tube formation might also be influenced by the redox chemistry of the metal cations. Ru(III) has to be oxidized to form RuO_2 and also the Fe(III) species that possesses a yellow color, transforms into Fe(II) under Ar atmosphere or in a sealed container. This is evidenced by a slow color change from yellow to transparent for the spinning solution containing Fe(III), PVP and DMF. Upon exposure to humid air the transparent solution quickly regains its yellow color (see Figure 4-11).

However, no significant difference in electrospinning was found between transparent and yellow solutions, as the re-oxidation by oxygen occurs predominantly at the surface which is greatly enlarged during spinning, thus accelerating the oxidation.

4.5 Relevant Literature and Proposed Mechanism

As mentioned before, nanotubes prepared by coaxial electrospinning have been reported in the literature, but also in some single-nozzle systems tube formation was observed at least temporarily. By using highly concentrated solution of hydrophobic PS (polystyrene) in DMF, evaporation leads to solid polymer skins on the electrospun jet. As the solvent further evaporates through this skin, the polymer is deposited and could potentially form a tube. However, as shown in Figure 4-12 insufficient mechanical stability of the polymeric skin usually leads to the collapse of the tube and nanoribbons or wrinkled fibers are obtained [134], [16].

A point worth mentioning is the fact that the PS nanoribbons are only obtained at low humidity, whereas at higher humidity a significant amount of water is incorporated into the electrospinning jet and the smooth fibers contain pools of water leading to some porosity⁴⁵ [134], [135].

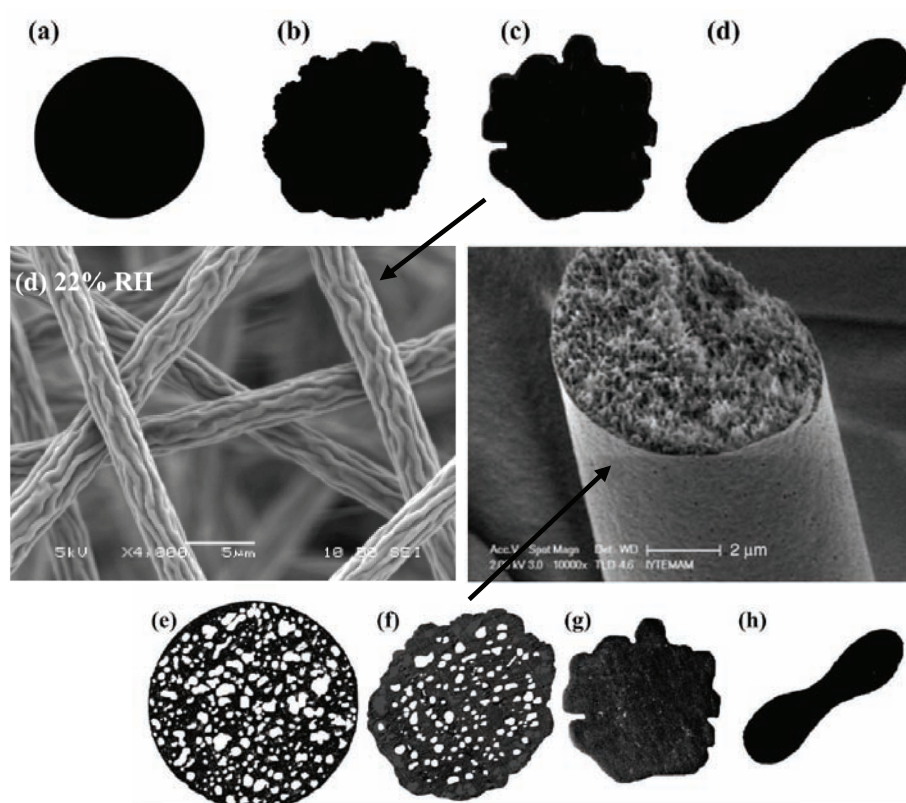


Figure 4-12: Morphology formation in hydrophobic PS electrospun at low humidity, i.e. 22% (a-d) leading to wrinkled fibers and nanoribbons, and at higher humidity, i.e. 35% (e-f) [134], [135]

⁴⁵ Demir et al. focus on the water incorporation [135], whereas Pai et al. show how low-temperature annealing can smoothen the wrinkled and porous nanofibers [134].

Therefore, it is not surprising that compact fibers are found at high humidity for the PVP-based systems, as the water is absorbed in the hydrophilic PVP and leads to hydrolysis and condensation within the fibers.

The formation of a solid skin layer seems quite universal in electrospinning jets, as whenever the rate of evaporation of the solvent at the surface exceeds the solvent's diffusion rate into that surface layer, solidification of the spinning polymer should occur [136]. In the fiber, a gradient in the concentration of polymer develops with a polymer-rich skin. Theoretically, tubes should occur especially when the diameter is well below 1 μm . In practice, for pure polymer systems the low mechanical stability often leads to the coalescence of the porosity or tubular morphology. However, in systems with metal precursors the morphology might be stabilized by the formation of hydroxides and oxides. Some attempts were made with reactive sol-gel precursors like $\text{Ti}(\text{OBU})_4$ and in chapter 3.2 it was already shown how TiO_2 skins can form on PS-PVP nanofibers inducing some porosity, but not the formation of nanotubes. Although condensation takes place this chemical sol-gel reaction is too slow to solidify a tubular morphology and the observed porosity results from the PS that does not mix with neither PVP nor Ti precursor and therefore acts as a template.

In the case of the PVP-DMF system, the rapid development of stabilizing hydroxides or oxides in the skin during electrospinning is even less likely, therefore a physical process must occur during solvent evaporation.

Although FeCl_3 and PVP are both well soluble in EtOH, a precipitation occurs when a drop of diluted FeCl_3 in EtOH⁴⁶ is added to a solution of PVP in EtOH, i.e. Fe^{3+} ions precipitate PVP in EtOH. As can be seen in Figure 4-13, the drop quickly develops a skin (i.e. an Fe-PVP complex insoluble in EtOH) separating the iron-rich core from the polymer-rich surroundings.



Figure 4-13: A drop of 10 wt% FeCl_3 in EtOH (left) and of 30 wt% FeCl_3 in DMF (right): a) after dropping, b) after mixing and c) after addition of more EtOH (left) or two of drops of DMF (right) and mixing

⁴⁶ More precisely $\text{Fe}(\text{OEt})_{3-x}\text{Cl}_x$ due to partial ligand exchange.

Obviously, it is not possible to electrospin this system and neither mixing nor diluting with more EtOH dissolves the skin.

In contrast, DMF is a good solvent for FeCl_3 and PVP and no Fe-PVP complex precipitates when Fe^{3+} in DMF is added to PVP in EtOH. Only upon mixing with excess EtOH some precipitate is formed, but can easily be re-dissolved by adding two more drops of DMF (see Figure 4-13 b and c). The precipitate is a Fe^{3+} -PVP complex for which EtOH obviously is not a good solvent, whereas DMF can dissolve the complex, possibly by forming a more stable Fe-DMF complex.

The chemical structures of DMF and PVP, more precisely the pyrrolidone moiety, are quite similar and both molecules possess a strong dipole moment with a negative partial charge on the amide oxygen and can act as complexing ligand (see Figure 4-14). In addition to being a carrier polymer in electrospinning, PVP of lower molecular weight therefore is a well-known stabilizing agent for nanoparticles [137], [138].

Similarly, PVP-complexes insoluble in EtOH can be prepared from many di- and trivalent metal cations like Ni^{2+} and $\text{Co}^{2+/3+}$ with trivalent cations forming more stable complexes⁴⁷.

Thus, the following refined mechanism can be proposed:

Initially, Fe^{3+} and PVP are dissolved homogeneously in EtOH and DMF. During electrospinning the solvents quickly evaporate⁴⁸ at the surface of the emerging fiber and a skin forms. However, with increasing concentration of Fe^{3+} and PVP near the surface of the fiber, a precipitate of Fe-PVP will form even before the fiber fully solidifies. As shown in Figure 4-13 and the respective discussion, the Fe-PVP precipitate is rather stable and can enclose a solution of lower concentration of Fe^{3+} or PVP. Therefore, a core-shell/skin morphology can develop inside the fibers

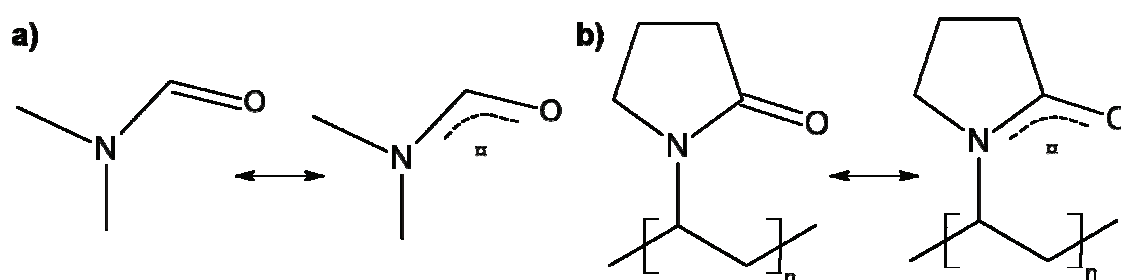


Figure 4-14: Chemical structures with delocalization for a) DMF and b) PVP

⁴⁷ The complex constant of M^{3+} like Fe^{3+} is 10-fold higher than for M^{2+} like Co^{2+} allowing to separate mixtures by dialysis against distilled water [139].

⁴⁸ The different boiling points of DMF (150°C) and EtOH (79°C) might initially lead to enrichment in DMF, but ultimately a skin solidifies on the fiber.

with a polymer-rich core, as the Fe-DMF migrates towards the surface. Upon calcination the iron-rich skin transforms into the Fe_2O_3 shell, while the polymer-rich core acts as a template before it is decomposed, resulting in hollow nanotubes. These observations and assumptions are summarized in Figure 4-15 and taken together provide a reasonable explanation for the nanotubes formation.

It would be highly desirable to further support the proposed mechanism by additional experimental data, such as a cross-sectional TEM image of fibers as-prepared and after different thermal treatments. However, direct proof of the radial gradient in polymer/Fe concentration could not be obtained due to experimental difficulties⁴⁹.

In conclusion, a novel self-templating approach was found to produce hollow nanotubes from solutions of PVP and metal cations $\text{Me}^{2+/3+}$ in EtOH/DMF. The proposed mechanism involves the formation of a solid polymeric skin upon solvent evaporation as postulated for many concentrated polymer solutions. The purely polymeric nanotubes are not sufficiently stable and collapse to form nanoribbons and -belts. In contrast, the metal cations stabilize the tubular structure by forming insoluble Me-PVP precipitates especially near the surface. Upon calcination the oxide-rich shell transforms into hollow nanotubes.

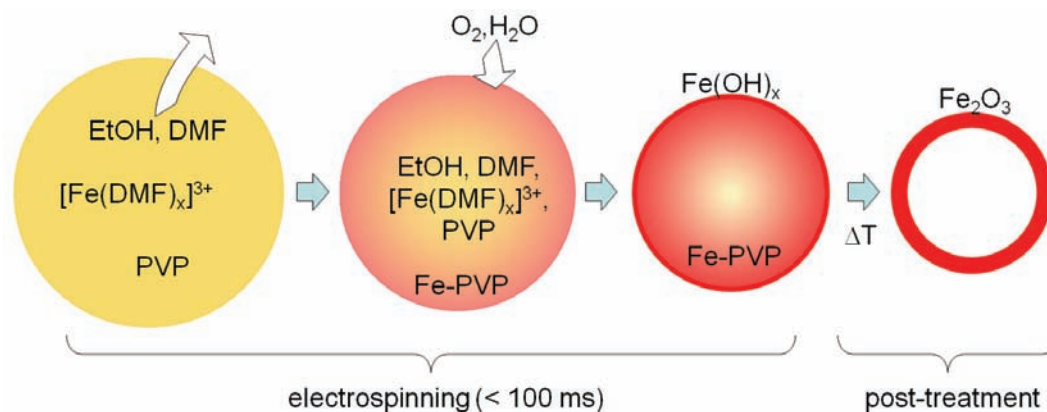


Figure 4-15: Proposed mechanism of tube formation: A homogeneous electrospinning jet dries and a solid Fe-PVP complex precipitates to stabilize the skin that later transforms into iron hydroxide and upon calcination to iron oxide

⁴⁹ The as-prepared hybrid Fe-PVP nanofibers could not be cut or broken at ambient temperature as the polymer is too flexible. Under liquid nitrogen the fibers could be broken, but no internal morphology could be observed. However, the as-prepared fibers are very sensitive to moisture and even when removing the liquid nitrogen under reduced pressure in an exsiccator (10 mbar), condensation of some humidity on the fibers could not be excluded.

In fact, low humidity during electrospinning and stabilization of the fibers at 80°C was found to help tube formation, whereas spinning and storage under high humidity led to compact fibers.

Although more investigations are necessary to further understand the nanotube formation, this approach might prove useful in the preparation of continuous tubular nanostructures in a single nozzle setup, that can be scaled up more easily than co-capillary electrospinning setups [140].

4.6 Crystal Phase Control in TiO₂:Ru Nanofibers

As already discussed above and in chapter 3, electrospinning involves rapid drying and solidification of the emerging nanofibers, i.e. physical processes that are usually much faster than the chemical sol-gel processes that might occur when the precursors react with ambient humidity and oxygen. The hybrid nanofibers can be considered as solidified solution in which further reaction of the precursors is prevented or at least slowed down by the polymeric matrix providing a confinement on the nanoscale [25]. Especially for systems with several precursors this confinement can be exploited to produce a hierarchical nanorods-on-nanofiber morphology when single-crystal V₂O₅ nanorods grow on a TiO₂ fiber after the polymer is decomposed and the miscibility of the crystallizing V₂O₅ and TiO₂ is too low. Interestingly, the remaining TiO₂ crystallizes as rutile already at low temperature (425°C), whereas usually anatase modification is obtained for electrospun titania nanofibers [90] and can only be converted to rutile by thermal treatment at 600°C for 6 h [141]. Even if the recrystallization does not destroy the fibers, the surface area is usually drastically decreased.

As will be discussed below, several works on modifying the crystalline phase of titania by doping with other transition metals can be found in the literature, with Ru_xTi_{1-x}O₂ constituting an interesting system for electrochemical and catalytic purposes. Whereas TiO₂ can crystallize as anatase, brookite or rutile and via sol-gel processes predominantly anatase is obtained, RuO₂ only forms a tetragonal rutile-type phase. Therefore it was found that doping TiO₂ with increasing amounts of Ru can influence the crystallization and directly leads to the rutile phase⁵⁰. Although the detailed mechanism is not known, it can be assumed that the presence of Ru^{3+/4+} in the amorphous state prevents the formation of anatase crystallites that are usually obtained under kinetic control⁵¹ and facilitate the crystallization to rutile. In sol-gel derived systems of Ru_xTi_{1-x}O₂ an appreciable amount of Ru ($x = 0.15-0.3$ depending on the conditions) is needed to achieve such phase control, i.e. obtaining phase-pure rutile [142]. The presence of acetylacetonate as complexing ligand seems to slow down fast hydrolysis and prevent anatase formation.

Ru doped TiO₂ nanofibers were also prepared with 4-7 at% Ru [143], yet no phase control was reported with a mixture of anatase, rutile and RuO₂ being observed at 600°C. Upon further heating the fibers transformed to rutile at 800°C only, before giving rutile and RuO₂ at 1000°C (the XRD in the reference is probably misinterpreted to metallic Ru). As the amount of Ru doping was

⁵⁰ A solid solution of Ru⁴⁺ in rutile TiO₂.

⁵¹ In acid aqueous solution Ti⁴⁺ can be hydrolyzed and converted to crystalline nanoparticles of either anatase, brookite and rutile. Under kinetic conditions, i.e. fast hydrolysis and condensation, only anatase is obtained, whereas highly acidic conditions (pH < 1) prevent the formation of anatase crystallites and allow thermodynamic control to yield rutile [45].

too low and the preparation involved hydrated precursors and a pre-hydrolyzation step, the presence of anatase should be expected.

If the doping with Ru was sufficient to yield the rutile phase only, it should be possible to prepare nanofibers of RuO₂ on rutile-TiO₂ with the same exceptional stability and interesting catalytic properties, as reported for the Deacon-type Sumitomo process (catalytic oxidation of HCl with O₂) [130] (see discussion in chapter 3.6).

Therefore, nanofibers with increasing content of ruthenium from 2-50 at% were prepared and analyzed by XRD. As can be seen in Figure 4-16, the phase composition shifts from anatase to rutile from 2-10 at% Ru, whereas at higher Ru content RuO₂ is observed as separate phase. This is consistent with reports that the limit for a solid solution in Ru_xTi_{1-x}O₂ is about $x = 0.1$ [142]. Below $x = 0.1$ anatase-TiO₂ is present as well, whereas at $x = 0.5$ RuO₂ can be found as additional phase.

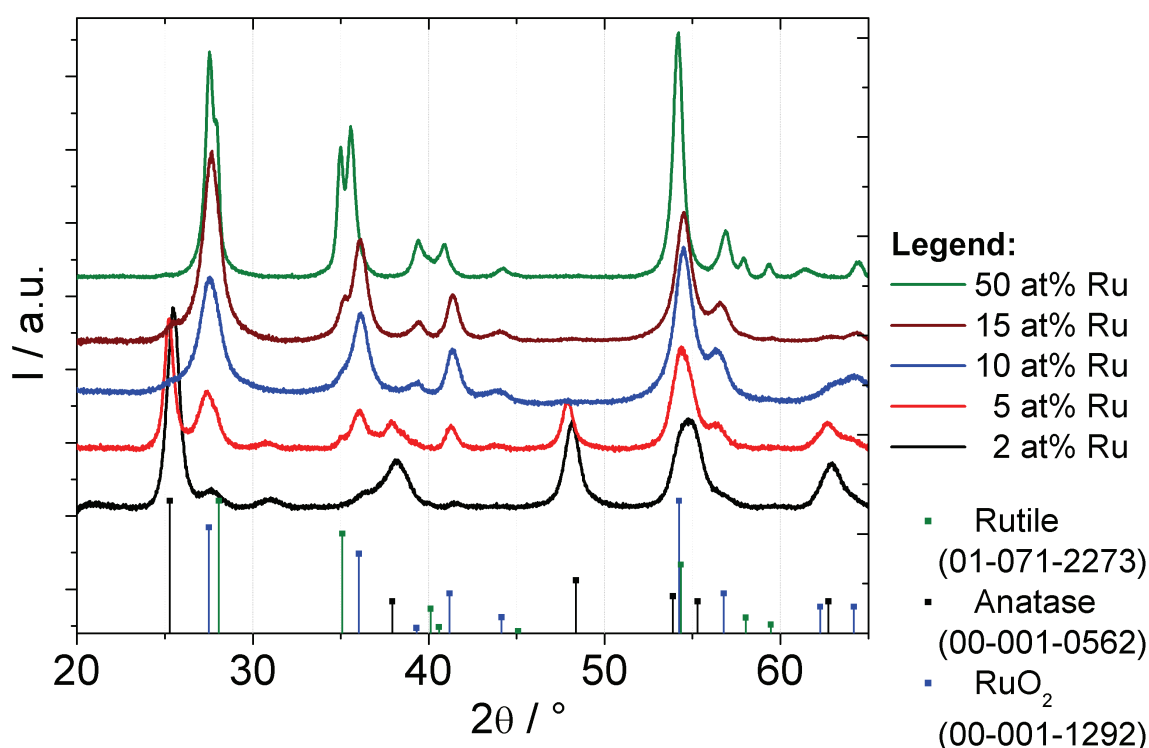


Figure 4-16: XRD of Ru_xTi_{1-x}O₂ nanofibers after calcination at 475°C with JCPDS references for Rutile, Anatase and RuO₂

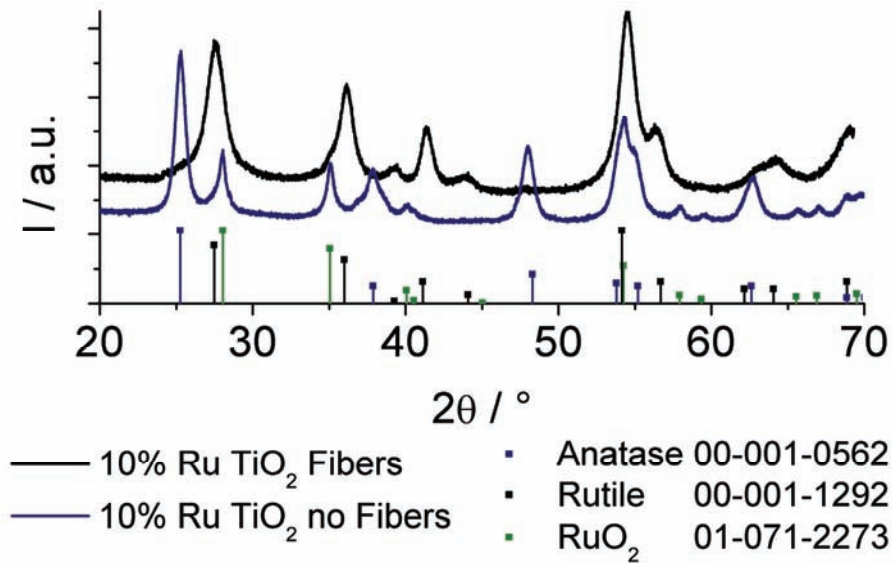


Figure 4-17: XRD of Ru_{0.1}Ti_{0.9}O₂ as fibers and dried after calcination at 475°C

More interestingly, the confinement and homogeneous distribution of the precursors in the nanofibers also play an important role. If one simply dries the solution for $x = 0.1$ instead of electrospinning it, the product contains anatase as well and the XRD resembles the one electrospun for $x = 0.05$ (see Figure 4-17). A Rietveld analysis of the XRD data reveals that RuO₂ is present as a separate phase with 6.2 wt% or 3.7 at%⁵². This means that a significantly lower amount of the ruthenium is available for the rutile-type TiO₂:Ru phase and therefore anatase-type TiO₂ forms as well.

The following table summarizes the results of a Rietveld analysis.

Table 4-1: Rietveld analysis (at%) of TiO₂:Ru systems at 475°C

preparation	Ru nominal*	RuO ₂	anatase	rutile [#]
dried	15	5,7	63,2	31,1
dried	10	3,8	75,4	20,8
dried	5	0,5	80,6	19,0
electrospun	50	31,1	0,0	68,9
electrospun	15	0,1	0,2	99,7
electrospun	10	0,1	0,1	99,8
electrospun	5	0,2	48,7	51,2
electrospun	2	0,1	86,5	13,4

* as weighed in

[#] Ru_xTi_{1-x}O₂

⁵² Taking into account the formula weights of RuO₂ (133.07 g/mol) and TiO₂ (79.866 g/mol).

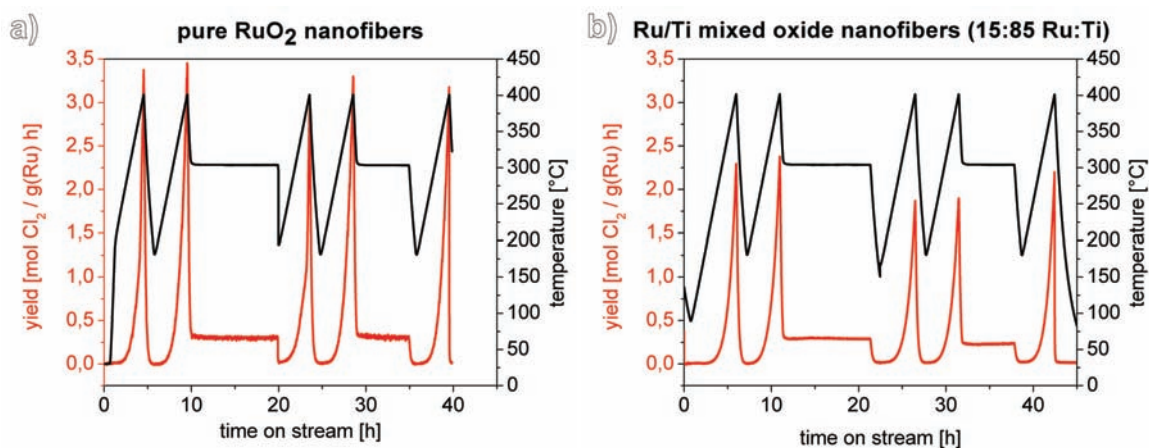


Figure 4-18: Yield in HCl oxidation as function of temperature: Comparison of a) RuO₂ nanotubes and b) Ru_{0.15}Ti_{0.85}O₂ nanofibers (The experiments were conducted by C.Kanzler)

The rutile-type nanofibers with the composition Ru_{0.15}Ti_{0.85}O₂ were tested as catalyst in HCl oxidation and their activity based on Ru content was only slightly lower than for pure RuO₂ nanofibers (see Figure 4-18). This finding is remarkable, taking into account that the surface area of the mixed oxide fibers is approx. 10-15% lower than for the pure RuO₂ nanotubes and that only 15% of the surface atoms should be Ru atoms.

Therefore, these mixed Ru_xTi_{1-x}O₂ systems still merit further investigation, especially regarding their stability at temperatures higher than 300°C, where they might prove more stable than pure RuO₂ systems⁵³. These investigations are currently carried out by our collaborators.

In conclusion, the fast drying during electrospinning at low humidity allows to obtain homogeneously distributed precursors that are stabilized against hydrolysis by the polymer matrix. Thus, phase control of TiO₂ to rutile at low temperature is possible by doping with ruthenium and as expected the TiO₂:Ru nanofibers show a high activity and good stability in corrosive environments.

⁵³ The observed 16% decrease in activity (0.29 to 0.24 mol Cl₂/g Ru) between the 300°C plateaux might be attributed to several effects, such as a migration of Ru atoms from the surface to the bulk.

Chapter 5 – Summary and Conclusion

5.1 Summary

Over the last decade, the preparation of nanofibers by electrospinning has been demonstrated for various materials, yet the application of these fibers has been mostly limited to the use in filtration, where especially polymeric nanofibers are already employed successfully.

The aim of this work was to create new types of nanofibrous morphologies via electrospinning and to study the relationship of their structure to their properties, as well as their functionality in complex composite architectures. Many systems like catalysts, solar cells and electrochromic devices can possibly benefit from the addition of nanofibers, as especially hybrid and inorganic fibers possess a wide range of useful properties, such as intrinsic porosity and high conductivity.

Accordingly, electrospinning TCO nanofibers allowed preparing a three-dimensional macroporous electrode that could be used for electrodeposition of metal oxides and the electrochromic Prussian Blue. In these composite systems, the well-distributed conducting nanofibers form conductive pathways in a less or non-conductive matrix and thereby lower the system's resistivity. This approach was demonstrated for ITO and ATO nanofibers that were embedded in mesoporous titania films and tested as dye-sensitized solar cells. Although higher currents could be obtained, the overall performance could not be improved significantly, as the voltage and fill factor were lowered by the presence of the TCO nanofibers. It was concluded that the titania matrix becomes sufficiently conductive under illumination, thus reducing the need for additional conductive pathways. In contrast, the TCO fibers proved highly useful to endow conductivity to polymer films. This novel application was patented in cooperation with BASF SE.

The preparation of ATO nanofibers was significantly improved by using preformed nanoparticles to ensure the optimal stoichiometry in the fibers. The influence of the particles' crystallinity on the sintering and the conductivity of the fibers was investigated and semi-crystalline nanoparticles were found optimal for this application, as they combine the correct stoichiometry with sufficient sintering potential.

Higher intrinsic conductivities could only be obtained in metallic nanofibers that could be prepared using the appropriate precursors and additives. The exceptional stability of Pt nanofibers against oxidation makes them well-suited for the use in composite electrodes and for electrodeposition, but only first steps were taken to evaluate their potential.

The nanoparticulate approach from the ATO fibers was then further extended to other oxides, especially TiO_2 , enabling the preparation of highly porous nanofibers that possess significantly higher surface areas than compact nanofibers. The crystallinity of such nanoparticles and the accompanying photocatalytic activity allowed to decompose the spinning polymer and “sinter” the nanofibers at room temperature using UV light, as demonstrated for thermally unstable $\text{TiO}_2(\text{B})$ particles.

These nanofiber mats possess a hierarchical morphology combining a high specific surface area with a good accessibility, making the fiber mats an interesting system for (photo)catalysis and as catalyst support (via the addition of metal nanoparticles or sol-gel precursors).

In addition to oxide nanoparticles, metal organic framework (MOF) nanoparticles could be incorporated into hybrid nanofibers endowing them with specific surface areas up to $550 \text{ m}^2/\text{g}$.

To complement the study of nanoparticles as building blocks for nanofibers, electrospinning of molecular precursors has been revisited as well. By preparing suitable precursors and using appropriate additives and co-solvents, sol-gel derived fibers could be produced for the first time for some binary and complex oxides, most notably for RuO_2 . The catalytic performance of the nanofibers in gas phase oxidations was found to be similar to RuO_2 nanopowders, but the well-defined fibrous morphology facilitates the study of stability and possible sintering processes.

Finally, hollow nanotubes of several oxides (RuO_2 , Fe_2O_3 and Co_2O_3) could be prepared for the first time without a co-capillary setup. The parameters of the tube formation have been analyzed and an underlying mechanism could be proposed, based on the insolubility of a cation-polymer complex that forms a stable skin on the electrospinning jet.

5.2 Outlook

While the results of the TCO nanofibers in oxide matrices led to the conclusion that these nanofibers do not improve the conductivity sufficiently to enhance the overall performance of the system, embedding the nanofibers into polymers resulted in transparent conducting (or at least antistatic) films even at very low nanofiber loadings. These films might prove very interesting for electronic devices or as antistatic packaging, because they can be made transparent or colored if pigments are added⁵⁴.

Similarly, the metallic nanofibers can endow conductivity where transparency is dispensable, and additionally they might prove more useful than the TCO fibers in composite electrodes. For example, Pt nanofibers could replace the commonly used Pt paste of solid oxide fuel cells (SOFC). As the reaction only takes place at the triple phase boundary (TPB) of Pt, oxide and gas phase, the current Pt coating is a trade-off between sufficient conductivity and porosity, as most of the electrode's surface is covered. The Pt nanofibers with a diameter of 50-75 nm are highly conductive and would significantly enlarge the TPB. First experiments already showed higher exchange currents, and even if the fibers tend to break up above 600°C, their thermal stability can certainly be improved by increasing the diameter or by doping with Re or Rh.

Apart from applications as electrodes, it is definitely worthwhile to further evaluate the nanofibers for gas-phase catalysis, especially for the study of reactions where the transport is diffusion-limited. Especially mixtures of nanoparticles and sol-gel precursors should be of interest, as the electrospinning allows for a homogeneous distribution of the components in a well-defined morphology. A prototypical system might be sol-gel-derived RuO₂ on preformed TiO₂ nanoparticles (preferably rutile for phase coherency and improved stability), offering a higher surface area than pure RuO₂ and an excellent dispersion of the expensive RuO₂, thereby also being an interesting system for industrial catalysis.

Even without the availability of rutile TiO₂ nanoparticles, the defined structure of the nanofibers can be useful in model catalysis. In this case, compact sol-gel-derived fibers with smooth surfaces are even more suitable. For example, RuO₂ and Ru_xTi_{1-x}O₂ might prove to be good model systems to study the catalyst's stability under harsh reaction conditions and to correlate morphological evolutions to changes in catalytic performance.

⁵⁴ In contrast, the addition of carbon nanofibers always results in black films.

Chapter 6 – Appendices

6.1 Experimental details

6.1.1 Chemicals

All chemicals were used as-received and without further purification.

Table 6-1: Solvents

Name	Abbr. ¹	CAS No.	Purity	Supplier
Methanol	MeOH	67-56-1	≥ 99 %	Sigma-Aldrich
Ethanol (absolute)	EtOH	64-17-5	≥ 98 %	Sigma-Aldrich
Isopropanol	i-PrOH	67-63-0	≥ 99 %	Sigma-Aldrich
Dichloromethane	CH ₂ Cl ₂	75-09-2	≥ 99 %	Sigma-Aldrich
Trichloromethane	CHCl ₃	67-66-3	≥ 99 %	Carl Roth
Benzyl alcohol	BzOH	100-51-6	≥ 99 %	Sigma-Aldrich
Diethyl ether	Et ₂ O	60-29-7	≥ 99 %	Sigma-Aldrich
N,N-Dimethylformamide	DMF	68-12-2	≥ 99 %	Sigma-Aldrich
Acetone		67-64-1	≥ 98.5 %	Sigma-Aldrich
Diethylene glycol	DEG	111-46-6	≥ 98 %	Sigma-Aldrich
Diethylamine	Et ₂ NH	109-89-7	≥ 99.5 %	Sigma-Aldrich
Acetic acid	AcOH	76-05-1	≥ 98.5 %	VWR
Hydrochloric acid	HCl	7647-01-0	≥ 98 %	Sigma-Aldrich
Formic acid		64-18-6	≥ 98 %	Sigma-Aldrich

¹: Abbreviation or chemical formula

Table 6-2: Precursors

Name	Formula	CAS No.	Purity	Supplier
Indium (III) acetylacetonate	In(acac) ₃	14405-45-9	≥ 99.9 %	Sigma-Aldrich
Tin(IV) chloride	SnCl ₄	7646-78-8	≥ 99 %	Sigma-Aldrich
Tin(II) fluoride	SnF ₂	7783-47-3	≥ 98 %	Sigma-Aldrich
Zinc(II) acetate dihydrate	Zn(OAc) ₂ ·2H ₂ O	5970-45-6	≥ 99 %	Sigma-Aldrich
Zinc(II) chloride	ZnCl ₂	7646-85-7	≥ 98 %	Sigma-Aldrich
Aluminum(III) chloride	AlCl ₃	7446-70-0	≥ 98 %	Sigma-Aldrich
Antimony (III) chloride	SbCl ₃	10025-91-9	≥ 99 %	Sigma-Aldrich
Ruthenium (III) chloride hydrate	RuCl ₃ ·H ₂ O	14898-67-0	≥ 99 %	ABCR
Ruthenium (III) acetylacetonate	Ru(acac) ₃	14284-93-6	≥ 97 %	ABCR
Titanium (IV) chloride	TiCl ₄	7550-45-0	≥ 99 %	Sigma-Aldrich
Titanium (III) chloride	TiCl ₃	7705-07-9	≥ 97 %	Sigma-Aldrich
Titanium (IV) isopropoxide	Ti(iPrO) ₄	546-68-9	≥ 97 %	Sigma-Aldrich
Potassium hexacyanoferrate (III)	K ₃ [Fe(CN) ₆]	13746-66-2	≥ 99 %	VWR
Potassium hexacyanoferrate (II) trihydrate	K ₄ [Fe(CN) ₆] · 3H ₂ O	14459-95-1	≥ 98.5 %	VWR
Palladium (II) acetate	Pd(OAc) ₂	3375-31-3	≥ 99.5 %	Heraeus
Platinum (II) nitrate	Pt(NO ₃) ₂	18496-40-7	≥ 99.5 %	Heraeus
Platinum (II) acetylacetonate	Pt(acac) ₂	15170-57-7	≥ 99.5 %	Heraeus

Table 6-3: Polymers

Name	Abbr. ¹	CAS No.	M _w ²	Supplier
Polyvinylpyrrolidone	PVP	9003-39-8	1300000	Sigma-Aldrich
Polyvinylbutyral	PVB	63148-65-2	70000	Kuray
Polyethyleneoxide	PEO	25322-68-3	400000	Sigma-Aldrich
Polyisobutylene-block-ethylene oxide	PIB	n.a.		BASF

¹: Abbreviation

²: Weight-average molecular weight

6.1.2 Characterization techniques

Scanning electron microscope (SEM)

For the morphological studies the high resolution SEM LEO Gemini 982 (Carl Zeiss MicroImaging GmbH, Goettingen, Germany) was used. It is equipped with a field emission cathode allowing low acceleration voltages (typically 2-10 kV were applied) and is equipped with several detectors for secondary electrons emitted from the sample. For this work, the inlens detector that works best at high magnifications was most suitable. Non-conducting samples were sputter-coated on a Scancoat instrument (BOC EDWARDS GmbH, Kirchheim, Germany) with thin layers of Platinum.

The SEM is coupled with an EDX (energy dispersive X-Ray spectroscopy) system from Oxford Instruments (Abingdon, United Kingdom) allowing elemental analysis of the microscopic samples. The principle relies on exciting core electrons with the highly energetic electron beam (acceleration voltages ≥ 15 kV) and analyzing the X-Ray radiation emitted when the core level is filled again. By comparing the obtained spectrum with a standard, elements in the sample can be identified and quantified. However, especially the quantification strongly depends on the calibration with the standard and was therefore interpreted with care.

Transmission electron microscope (TEM)

For microstructure investigations at higher magnifications, bright-field images were recorded on the transmission electron microscope CM30-ST (Philips Electron Optics, Eindhoven, Netherlands) operated at 300 kV and a point resolution of 0.4 nm.

X-Ray Diffraction (XRD)

WAXS (Wide-Angle X-Ray Scattering) experiments in θ - 2θ geometry were performed using an X'Pert PRO diffractometer (Panalytical, Almelo, Netherlands) with Cu K_{α} radiation of $\lambda = 0.154$ nm and slit of $1/2 - 1/4$ inch.

SAXS (Small-Angle X-Ray Scattering) measurements were carried out on the same instrument with a $1/16$ inch slit.

Gas physisorption

The gas physisorption measurements were mainly conducted on an AUTOSORB-1 and -6 from Quantachrome (Boynton Beach, USA) with nitrogen as adsorbate at 77K. The software supports the standard reduction algorithms and the BET (Brunauer-Emmett-Teller) method was used to quantify the surface area. It extends Langmuir theory for adsorbate monolayers to multilayer formation on the sample (which is a suitable physisorption model for non-microporous materials) and calculates the surface area from the cross section of the adsorbate on the surface. Although the obtained results do not represent absolute values, a relative comparison especially of similar samples is definitely permissible.

Further measurements with CO₂ were performed with a Rubotherm Magnetic Suspension Balance (Rubotherm GmbH, Bochum, Germany) at the Institute for Nonclassical Chemistry at the University of Leipzig.

Conductivity measurements

A Keithley 2000 multimeter (Keithley Instruments GmbH, Germering, Germany) was used to measure conductivities in 2- and 4-point probe mode. The samples were contacted via gold-plated electrode tips with a distance of 1.5 mm from one another and with built-in springs to push the tip to the surface. Alternatively, conducting silver paste was applied to the sample (especially in the case of nanofiber mats) in a defined pattern (1 cm stripes 1 cm apart) and the resistance was metered in 2-point mode.

As can be seen from the following figure, 4-point probe measurements are not sensitive to additional resistances from the lead wires or contact resistances, as the very small sense current is separated from the source current that is forced through the sample.

In practice, it was found that using silver paste effectively reduced contact resistances and that the samples' resistance was usually high enough ($> 100 \text{ Ohms}$) to neglect the contributions from lead wires etc. ($\sim 500 \text{ mOhms}$).

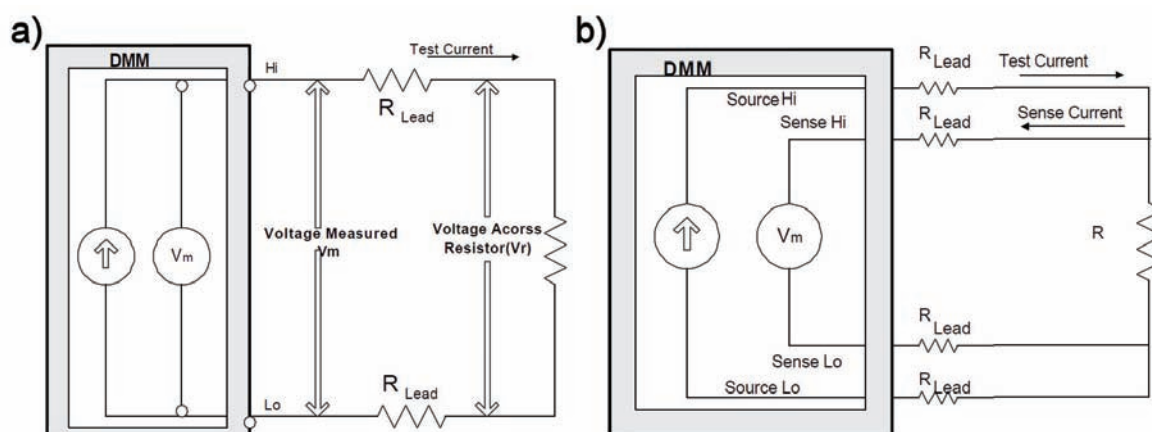


Figure 6-1: Circuit diagram* of conductivity measurements in a) 2-point and b) 4-point mode

* Figure from the Keithley 2000 Manual, 2003

Profilometry

The film thickness was measured with a profilometer (Alpha-Step IQ from KLA-Tencor, Dresden, Germany).

Electrochemical setup

Electrochemical measurements and electrodepositions were performed using an Autolab 12 potentiostat/galvanostat (Metrohm Autolab B.V., Utrecht, Netherlands) with a Platinum wire as counter electrode and a Silver wire or TCO slide as pseudo-reference electrode.

UV/VIS

Absorbance spectra and absorbance measurements were recorded on a UVIKON XS spectrophotometer (Kontron AG, Eching, Germany)

6.1.3 Electrospinning setup

As mentioned in the introduction, a basic electrospinning setup consists of a high-voltage power supply and dosage unit for the spinning solution.

For this work an electrospinning setup was built from a Spellman CZE1000R high-voltage power supply (0-30 kV, 300 μ A) connected to the spinning tip and a FUG 7-3500 (0-3.5 kV, 2 mA) high-voltage power supply connected to the collector. One or two KDS 100 syringe pumps (KDS Scientific Inc., Holliston, USA) were employed to deliver the solution at a constant rate (0.2-2 ml/h) through a metallic needle. For safety reasons and to provide a homogeneous electric field, the needle was clipped and deburred prior to use.

The whole setup was placed in a chamber in which the relative humidity could be controlled from 5-80% by purging with dry or moist air. A glove allowed to exchange samples without opening the chamber.

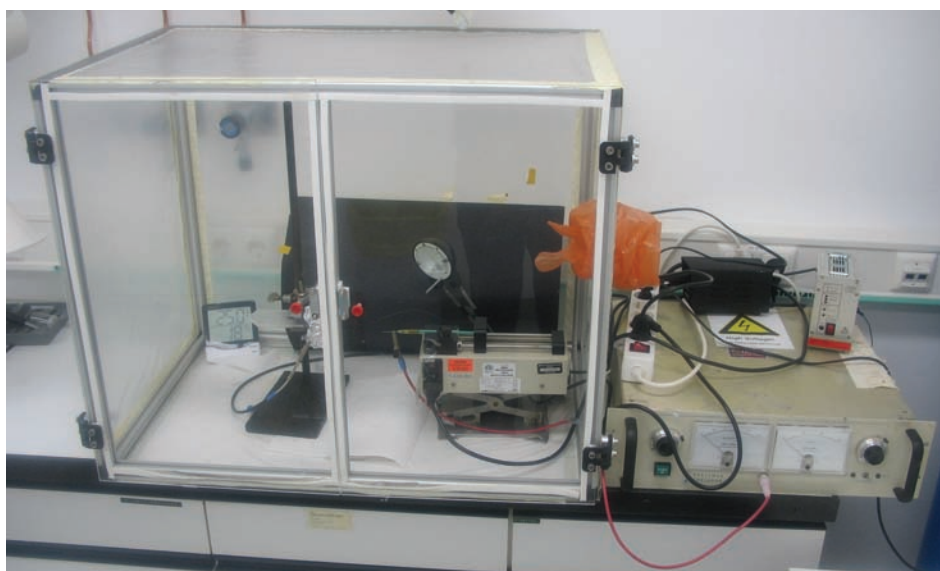


Figure 6-2: Digital image of the electrospinning setup

6.1.4 ITO nanofibers

The spinning solution was prepared by dissolving 500 mg $\text{In}(\text{acac})_3$ in 1 g acetone, heating until a clear solution was obtained, then 500 mg MeOH and 40 mg SnCl_4 (12.5 at%) were added.

To this precursor solution, 650 mg of the polymer solution of 15 %wt PVP in MeOH were added and the resulting solution was vigorously mixed, before being loaded into a 1 mL plastic syringe (Omnifix F from B.Braun, Melsungen, Germany).

This solution was fed at a rate of 0.4 ml/h and electrospun at 1kV/cm (7 kV, 7cm distance between tip and collector) and a relative humidity of 30-35%.

The fiber mats were collected on aluminum foil, silicon wafers, normal and FTO-coated glass slides and calcined at 550°C for 10 min.

During calcination, a lateral shrinkage of 15-20% was observed that led to delamination of the fiber mats from the substrate, especially for thick mats. To reduce this unwanted behavior, the substrates were dip-coated in a 1 wt% PVP solution in EtOH to produce a polymer film with a thickness of 500-800 nm. This film melts during calcination and the fibers that are floating on the polymer melt can shrink with less or without rupture.

6.1.5 ATO nanoparticle synthesis and ATO nanofibers

Several attempts of using sol-gel precursors to obtain ATO ($\text{SnO}_2\text{:Sb}$) only led to tin oxide fibers with high resistances ($> 1\text{M}\Omega/\text{cm}$), probably due to an imperfect stoichiometry. The synthesis of a nanoparticle dispersion effectively circumvented the problem:

A precursor solution is prepared from 0.2 mL conc. HCl, 980 mg SnCl_4 and 65 mg SbCl_3 (7.5 at%) in 12 g EtOH. This solution is added dropwise to 2.5 g of an aqueous solution of NH_3 (20 wt%) under vigorous stirring. A white slurry containing preformed ATO nanoparticles is obtained, from which the nanoparticles can be separated by repeated centrifugation and washing with H_2O until some yellowish nanoparticles remain in the supernatant solution.

By using ultrasonic agitation dispersion with up to 20 wt% of ATO in 4:1 mixture of H_2O and diethylamine could be prepared.

In a typical electrospinning experiment, 0.5 g of ATO nanoparticles dispersion and 125 mg ethanol were added to 625 mg of a solution of PVP, poly(vinyl pyrrolidone) ($M_w \approx 1,300,000$), in methanol (12 wt%).

This solution was fed through a metallic needle by a syringe pump (KDS scientific) at the rate of 0.4 ml/h. The needle was placed at a distance of 6.5 cm from the aluminum foil that served as collector and a voltage of 5 kV was applied to produce a non-woven mat.

6.1.6 FTO, AZO and IZO nanofibers

Similarly to the ATO nanofibers, it was not possible to produce well-conducting FTO ($\text{SnO}_2\text{:F}$), AZO (ZnO:Al) or IZO (ZnO:In) fibers from sol-gel precursors.

Yet, the precipitation in NH_3 did not lead to the desired nanoparticles either, as the fluoride anion F^- does not co-precipitate into the hydroxide/oxide matrix. Furthermore, ZnO does not form in ammonia solution (rather $[\text{Zn}(\text{NH}_3)_6]^{2+}$ is obtained), but IZO and AZO nanoparticles could only be obtained via a microwave synthesis in DEG (diethylene glycol) as proposed by Feldmann et al [144]. This polyol synthesis at 200°C takes advantage of the high boiling point and the chelating properties of DEG to produce particles that are crystalline and well-conducting (IZO: $\sim 1 \text{ Ohm}\cdot\text{cm}$, AZO was less conducting) without further thermal treatment.

It was possible to synthesize IZO nanoparticles by heating 1000.9 mg $\text{Zn}(\text{OAc})_2\cdot 2 \text{ H}_2\text{O}$ and 50.9 mg InCl_3 in 50 mL DEG and 1 mL H_2O to 200°C in an MLS rotaprep 1500 laboratory microwave oven (MLS GmbH, Leutkirch, Germany). The bluish nanoparticles were recovered by

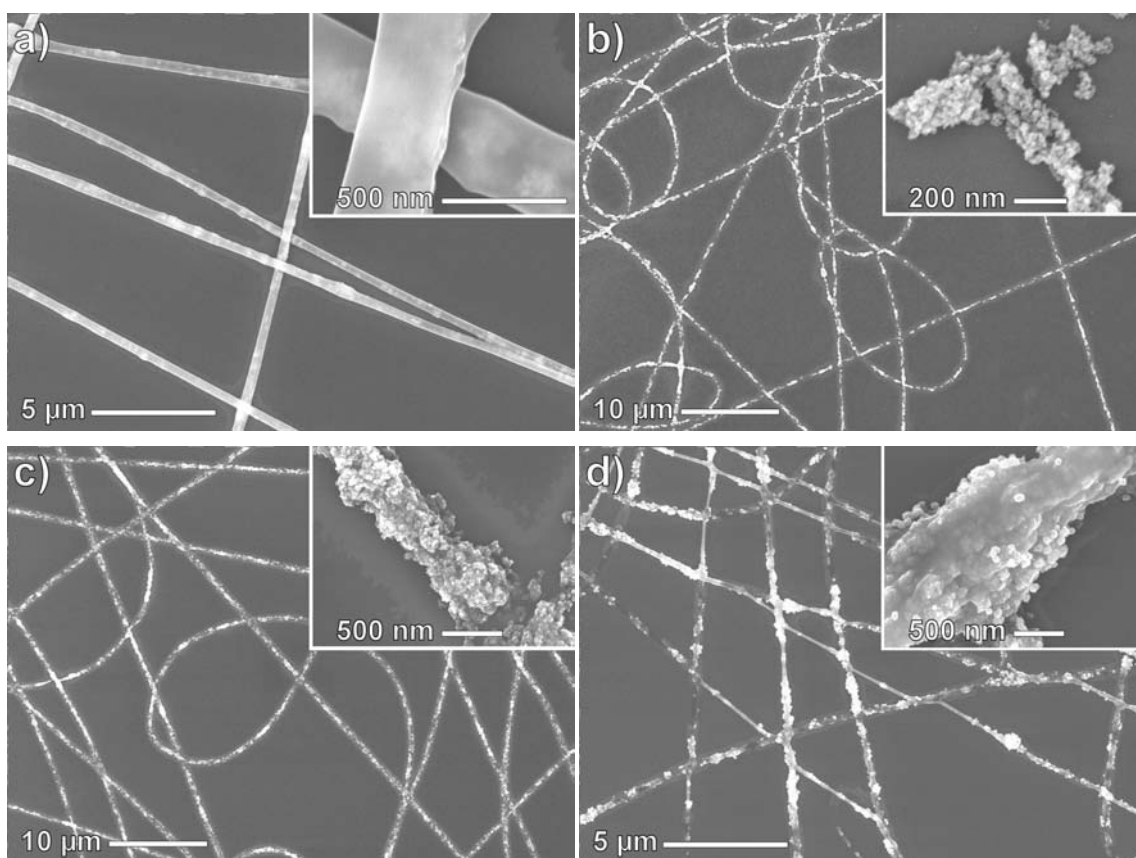


Figure 6-3: SEM images of nanofibers: a) IZO nanoparticles in PVP, b) after calcination at 550°C , c) with 5% ZnCl_2 and d) with 10% ZnCl_2

centrifugation and used to obtain a dispersion of 10 wt% in ethanol. 250 mg of this dispersion were mixed with 200 mg of a 10 wt% PVP in MeOH solution and electrospinning was carried out with the following parameters:

Voltage:	5 kV
Distance:	7 cm
Feed rate:	0.3 ml/h

The resulting fibers were calcined at 550°C for 10 min, but no conductivity was observed. SEM images show that the crystalline nanoparticles did not sinter together properly and were present as individual nanoparticles. Therefore, 5 and 10 at% of ZnCl₂ were added with respect to the Zn content, resulting in fibers that were more continuous, but the resistance was still very high (100 kOhm/cm). Obviously, there is a trade-off between adding ZnO to sinter the particles together and the lower conductivity of the pure ZnO phase.

However, by improving the nanoparticles' synthesis, i.e. using shorter times and lower temperatures, it should be possible to obtain partially amorphous particles and thereby improve the conductivity of the resulting fibers.

6.1.7 Spray pyrolysis of ATO and FTO

As will be pointed out in the next section, the thermodynamic stability of the different TCO materials varies due to their structure and composition.

In order to form the desired phase with the correct stoichiometry, sol-gel processes are not the most suitable choice and the best conductivities are usually observed by gas-phase deposition techniques. In order to evaluate the various TCO materials, spray pyrolysis onto glass substrates was employed with excellent results (usually the resistivity was only one order of magnitude higher than reported in the literature).

The setup consisted of a Schott SLK hotplate with glass-ceramic panel (Schott AG, Mainz, Germany) and an airbrush gun (OBI GmbH, Wermelskirchen, Germany) that was loaded with a precursor (1-2 wt%) solution in ethanol. A compressor and a valve with meter flow were used to adjust the pressure to 5-50 mbar.

By applying a very thin layer of ATO or FTO, the conductivity of nanofiber mats could be improved, as individual fibers were contacted with one another and the conducting substrate.

Thereby, highly conducting fibrous electrodes could be obtained that were used as substrates for electrodeposition.

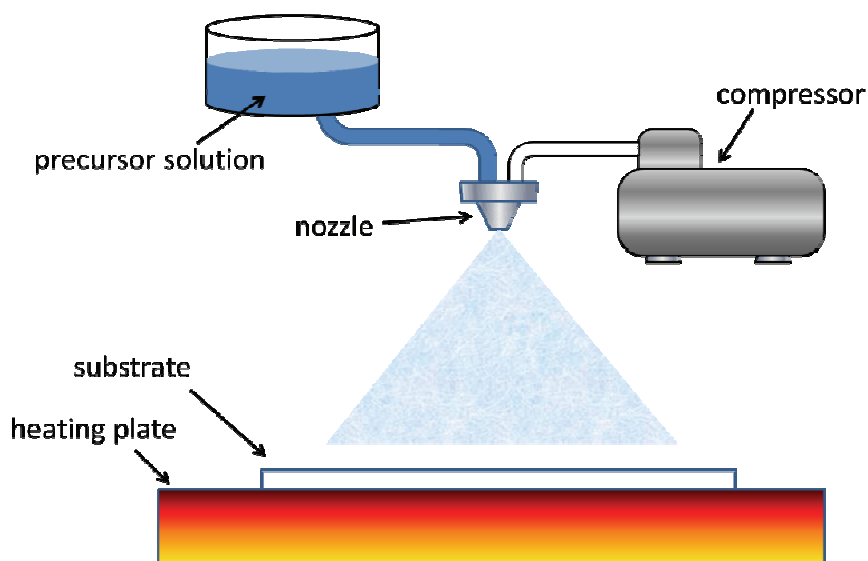


Figure 6-4: Basic setup of thin film deposition by spray pyrolysis

6.1.8 Comparison of the TCO materials

Whereas sputtering and vapor deposition techniques produce thin films of all TCO materials, only ITO can be reproducibly prepared as sol-gel derived films and fibers.

The following table shows the lattice energies of the various TCO materials and the ionic radii of their constituents. Without doping, the oxides of indium, tin and zinc are wide-band gap semi-conductors and the corresponding thin films possess a good transparency, but only a low conductivity. By doping with cations additional acceptor levels are created near the valence band, whereas anions with lower charge provide donor levels near the conduction band. To replace an ion of the host lattice with a foreign ion, the ionic radii must be similar.

Ideally, the lattice energy of the constituting oxides should also match, otherwise it is thermodynamically more favorable to form two distinct phases rather than the doped TCO phase.

Table 6-4: Comparison of TCO materials [145]

TCO	ITO			ATO			FTO			MZO			
Formula	In ₂ O ₃ :Sn			SnO ₂ :Sb			SnO ₂ :F			ZnO:M			
Lattice energies of the oxides		$\Delta H_G / \text{kJ mol}^{-1}$	eV / atom		$\Delta H_G / \text{kJ mol}^{-1}$	eV / atom		$\Delta H_G / \text{kJ mol}^{-1}$	eV / atom		$\Delta H_G / \text{kJ mol}^{-1}$	eV / atom	
		In ₂ O ₃	924	4.8	SnO ₂	581	6.0	SnO ₂	581	6.0	ZnO	347	3.6
		SnO ₂	581	6.0	Sb ₂ O ₅	978	5.1	F ⁻ does not co-precipitate, HF is volatile			Al ₂ O ₃	1676	8.7
											Ga ₂ O ₃	1104	5.7
										In ₂ O ₃	924	4.8	
Ionic radii (10 ⁻¹⁰ m)	In ³⁺	0.81		Sn ⁴⁺	0.71		O ²⁻	1.36		Zn ²⁺	0.74		
	Sn ⁴⁺	0.71		Sb ⁵⁺	0.62		F ⁻	1.28		Al ³⁺	0.51		
										Ga ³⁺	0.62		
										In ³⁺	0.81		

In the case of ITO (and ATO to a lesser extent) the conditions are fulfilled and the desired phase is obtained rather easily.

For AZO, the radii do not match and it is more favorable to form the very stable aluminum oxide, therefore AZO can only be prepared by vapor techniques or at high temperature. Doping zinc oxide is less difficult with Ga^{3+} or In^{3+} , as confirmed experimentally for the polyol synthesis. For slower sol-gel processes like dip-coating or the pyrolysis of electrospun nanofibers, it is unlikely to generate the correct crystalline phase.

Similarly, doping with F^- is not possible in normal sol-gel processes, as fluoride will not co-precipitate with the hydroxides and HF might escape during calcination.

6.1.9 Pt and Pd nanofibers

After the promising results with $\text{In}(\text{acac})_3$ as precursor for ITO nanofibers, it was attempted to use $\text{Pt}(\text{acac})_2$ for Pt nanofibers. Accordingly, 33 mg $\text{Pt}(\text{acac})_2$ in 350 mg DCM were added to 150 mg of a solution of 12 wt% PVP in MeOH and successfully electrospun at 1 kV/cm. However, after thermal treatment in both air or nitrogen, no fiber was formed, as probably most of the $\text{Pt}(\text{acac})_3$ sublimated.

Using the more ionic $\text{Pt}(\text{NO}_3)_2$ was not possible, as the conductivity of the solution was too high to allow electrospinning.

These problems were comparable to those with $\text{Ru}(\text{acac})_3$ [see Chapter 6.1.17], therefore 30 mg of $\text{Pt}(\text{NO}_3)_2$ were similarly dissolved in 300 mg DMF and refluxed at 125 °C for 15 min to form a Pt-DMF complex. The recipe could be improved by adding 35 mg AcOH before refluxing.

The solution was then diluted with 150 mg of MeOH and 350 mg of 12 wt% PVP in MeOH.

Electrospinning could be carried out at a feed rate of 0.25ml/h, a voltage of 3.5 kV and a distance of 6-7 cm.

Surprisingly, the nanofibers could be converted to pure Pt via a thermal treatment of 10 min at 400°C in air and a reduction in N_2 or Ar did not improve the conductivity. It is assumed that the polymer aids in reducing the Platinum and is decomposed in this reaction at a rather low temperature.

For Palladium nanofibers, 40 mg of $\text{Pd}(\text{OAc})_2$ could be used in 50 mg DMF and 250 mg of MeOH in the above recipe without refluxing. However, to obtain metallic fibers, the as-spun fibers must be stabilized in air at 350°C for 15 min, before reducing in $\text{H}_2(10\%)/\text{N}_2$ at 400°C for 30 min.

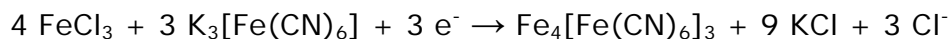
6.1.10 Electrodeposition of Prussian Blue and TiO₂

For the electrodeposition of Prussian Blue, Fe^{III}₄[Fe^{II}(CN)₆]₃, the following solution was used (recipe adopted from the literature [146]):

- 5 mL of 0.05 M HCl
- 10 mL of 0.05 M K₃[Fe(CN)₆]
- 10 mL of 0.05 M FeCl₃ * 6H₂O

The above solution must be prepared freshly (the respective stock solutions could be used for several weeks) and could be used for some hours. Afterwards precipitates of Prussian Blue formed.

The substrate (FTO and glass slides with ITO, ATO and Pt nanofibers) was immersed in the solution and a reduction current of ca. 40 mA/cm² vs. Pt electrode was passed through this 2-electrode system (the potential should be -300 to -500mV). The growth rate was about 500 nm/min and Prussian Blue was formed according to the following reaction:



After the electrodeposition was completed, the electrode was carefully washed with H₂O and EtOH.

As the conductivity of Prussian Blue is sufficient (fast oxidation and reduction of films of several micrometers), the purpose of the electrodeposition was only to prove that the fibrous electrodes were suitable for electrodeposition onto the fibers.

A detailed study of the electrochromic behavior was therefore not carried out, although the charge efficiency might be improved by the presence of especially the metallic nanofibers.

6.1.11 TiO₂ nanoparticle synthesis

The amorphous TiO₂ nanoparticles were synthesized after the following recipe:

- 3.43 g TiCl₄ was dissolved in 10 g EtOH
- 480 mg 1,3-propanediol in 42 g Benzyl alcohol were added

The mixture was stirred at 80°C for 8 h, before precipitating it in 120 g Et₂O. The precipitate was collected by centrifugation at 5500 rpm and washed once with Et₂O. By adding MeOH the nanoparticles were redispersed to a concentration of 7-8 wt%.

With H₂O the nanoparticles dispersed much better, but the dispersion gelled within several hours to days. This indicates that these amorphous nanoparticles were rather partially condensed Ti(IV) complexes than particles.

Using DMF instead of H₂O, concentrations up to 20 wt% could be obtained without any gelation.

To obtain more crystalline nanoparticles, a variation of the synthesis⁵⁵ was carried out at 110°C for 2 h.

To further improve the crystallinity and obtain larger nanoparticles, the EtOH to dissolve the TiCl₄ was replaced with toluene, preventing the formation of Ti(OEt)₂Cl₂ and increasing the reactivity towards the oxide.

Especially for nanoparticles synthesized at 110°C it was found that the addition of up to 25 wt% of DMF greatly helped to form stable and highly concentrated dispersions.

⁵⁵ Proposed by Christoph Weidmann.

6.1.12 TiO₂ nanofibers

In a typical electrospinning experiment, 500 mg of a solution of 12 wt% PVP (MW = 1,300,000) in methanol were added to 600-1500 mg of the TiO₂ nanoparticle dispersion and mixed thoroughly. If necessary, 100 mg DMF were added and the solution was concentrated under reduced pressure to yield a final concentration of 4 wt% of PVP. Alternatively, DMF was already used as co-solvent for the dispersions.

The spinning solution was fed through the metallic needle to produce a non-woven mat with these parameters:

Voltage:	7 kV
Distance:	6-8 cm
Feed rate:	0.35 ml/h

The relative humidity could be in the range from 5-40% without major effects on fiber quality.

The nanofibers were calcined at 550°C for 30 min (with a ramp of 10°C/min).

6.1.13 UV treatment of TiO₂ nanofibers

Another possibility to remove the spinning polymer from the nanofibers with crystalline TiO₂, was to irradiate a fiber mat for several hours with UV-C light (200–290 nm, 343 mW cm⁻²) from a UV-F 250 B (Hartmann Feinwerkbau GmbH, Obermoerlen, Germany). During irradiation, the samples were kept at a constant temperature of 25 °C by cooling the supporting tray with a thermostat.

Typically, the treatment was carried out for 2h at a distance of 10 cm, leading to a complete decomposition of the spinning polymer and a sintering of the TiO₂ fibers. When using amorphous nanoparticles or sol-gel derived TiO₂ the conversion was much slower and even after 24h, most of the fibers dissolved in H₂O.

6.1.14 TiO₂(B) nanoparticles and nanofibers

These nanoparticles were kindly provided by S. Sallard.

Briefly, 400 mg C₁₆mimCl and 600 mg C₄mimBF₄ were mixed at 95 °C in a flask before 0.2 mL TiCl₄ was slowly added. After 5 min, 0.45 mL water was added dropwise and stirring was continued for 14 h. The temperature was then decreased to 80 °C and 10 mL of ethanol were used to extract the ILs. After another 8 h, the suspension was cooled down to room temperature, centrifuged and washed once with ethanol.

To functionalize the nanoparticles for electrospinning the wet powder was redispersed in 10 mL ethanol with 200 mg 1,3-propanediol. This suspension was stirred at 80 °C for 8 h and then cooled down to room temperature. After precipitation with diethyl ether, the particles were collected by centrifugation and redispersed in methanol/dimethylformamide (DMF) (90:10 weight %) to get a suspension with a concentration of around 7–10 wt% TiO₂(B).

For the electrospinning, the 380 mg of the TiO₂(B) dispersion were mixed with 130 mg DMF and 160 mg of 12 wt% PVP in EtOH. The dispersion was concentrated under vacuum (45 mbar) to half of the volume. Then the dispersion was mixed with 81 mg EtOH, 8 mg AcOH and 12 mg Ti(OBu)₄ as sol-gel derived “glue” to help sinter the particles together.

The electrospinning was operated as follows:

Voltage: 7 kV
Distance: 8-10 cm
Feed rate: 0.3 ml/h
Relative humidity: < 40%

A non-woven mat was collected for up to 5 min on a silicon wafer (resulting in a layer with 3-4 μm thickness, thicker layers did not allow the UV light to pass through) and the polymer was removed by UV-C irradiation (200–290 nm, 343 mW cm⁻²) for five hours.

6.1.15 SiO₂ nanofibers

Most of the properties of the oxide nanofibers presented in this work result from their crystallinity, e.g. the photocatalytic properties of anatase TiO₂ and TiO₂(B) or the conductivity of the TCO fibers. However, crystalline metal oxides are brittle and even if it is reasonable to assume that nanofibers are more flexible than a similar thin film, the fibers may still break when subjected to mechanical deformations (bending and stretching)⁵⁶. Typically, a strain of only 1-2% can be tolerated before breaking of the oxide fibers [148].

It was found that the non-woven nanofiber mats were quite stable and even self-supporting as free-standing structures and subjecting them to a gas flow for gas phase catalysis did not break any fibers. However, when immersed into solution and especially under agitation (e.g. a stirred solution) the fibers were slowly broken and small fragments were washed out from the non-woven mat. This problem was found to some extent during electrodepositions where the conductivity of the nanofiber structure decreased, but most pronounced during photocatalysis where the catalyst was slowly washed out. Although this might have even increase the photocatalytic performance, it became more complicated to remove the catalyst from the solution.

Applying a thin layer of polymeric nanofibers effectively retained all fragments, but this approach was not suitable for photocatalysis, as the polymer would also be degraded.

An alternative was found in SiO₂ nanofibers that do not crystallize and show remarkable mechanical strength and flexibility.

A solution of Si(OEt)₄ was prehydrolyzed under acidic conditions to form oligomeric SiO₂, i.e. 2000 mg Si(OEt)₄ and 370 mg of 1M HCl was added to a solution of 230 mg H₂O and 1000 mg EtOH and stirred at 70°C for 45 min. The resulting solution needed to be kept at 5°C and was stable for 3-4 weeks.

500 mg of this solution and 100 mg DMF were added to 400 mg of a solution of 12 wt% PVP in EtOH and electrospinning was carried out with the following parameters:

Voltage: 6 kV
Distance: 7 cm
Feed rate: 0.3 ml/h
Relative humidity: 20-40%

⁵⁶ In contrast, polymeric or hybrid nanofibers were shown to be extremely flexible, tolerating high deformations and strain up to 70-80% [147].

The nanofibers further hydrolyzed after spinning upon contact to ambient moisture. This process took 10-60 min depending on the relative humidity and was accompanied by a marked increase in tensile strength⁵⁷.

Applying a thin layer (500-800 nm) of SiO₂ nanofibers proved very useful for photocatalysis of titania fibers and electrodeposition on fibrous ATO electrodes.

⁵⁷ The increase in tensile strength was outside the scope of this work and was therefore not quantified. Directly after spinning, the fiber mat could be easily stretched with tweezers, after 60 min the stiffness was comparable to a thick polymer film.

6.1.16 ZIF-8 nanoparticles and nanofibers

The colloidal suspensions of ZIF-8 nanoparticles in methanol were kindly provided by J. Cravillon. Briefly, a solution of $\text{Zn}(\text{NO}_3)_2 \cdot 6\text{H}_2\text{O}$ (2.933 g) and 2-methylimidazole (6.489 g) in 200 mL methanol was stirred at room temperature for 1 h, before separating the resulting nanocrystals by centrifugation. The ZIF-8 nanoparticles were then redispersed in fresh methanol by vortex mixing and ultrasonic agitation, and a part of the solution was dried at 80°C under reduced pressure to determine the concentration to be 3.5-4.5 wt% of ZIF-8. In a typical electrospinning experiment, 500 mg of a solution of 12 wt% PVP in methanol were added to 400-2000 mg of the ZIF-8 dispersion and mixed thoroughly. The solution was diluted or concentrated under reduced pressure to yield a final concentration of 3.5 wt% of PVP. This solution was electrospun at a voltage of 5 kV and a distance of 6-8 cm at a rate of 0.35 ml/h. It was necessary to keep the relative humidity below 40%.

The nanofibers were obtained as non-woven mats and were stable up to 60% relative humidity air, but sensitive to water.

Similarly to PVP, it was possible to electrospin the ZIF-8 nanoparticles from PEO and PS with the following parameters:

- a) PEO (MW = 300,000) 2.5 wt% in H_2O

3 wt% ZIF-8 nanoparticles

Voltage: 6 kV

Distance: 5-6 cm

Feed rate: 0.45 ml/h

Relative humidity: < 20%

- b) PS (MW = 240,000), 8 wt% in 4:1:1 THF (tetrahydrofurane) : toluene : methanol

(via solvent exchange, i.e. after adding toluene the solution was evaporated under reduced pressure)

~ 2.5 wt% ZIF-8 nanoparticles

0.2 wt% tetrabutylammoniumperchlorate

Voltage: 5 kV

Distance: 6 cm

Feed rate: 0.65 ml/h

Relative humidity: < 20%

Measurement of adsorption kinetics

A method was developed for measuring adsorption kinetics on a Quantachrome Autosorb-1 instrument operated in manual mode. This instrument possesses a manifold with calibrated volume separated from the measurement cell by a magnetic valve. Both manifold and measurement cell are equipped with pressures gauges. Sorption kinetics are determined by setting a defined nitrogen pressure in the manifold with subsequent expansion into the evacuated sample cell cooled to 77K. The sample cell pressure during the adsorption process was recorded every 250 ms until equilibrium was reached.

We were aware that especially at the beginning of this experiment, the adsorption was superimposed by transport effects into the cell and therefore we focused on the evolution of pressure near the equilibrium and the time to attain equilibrium. We adjusted the initial manifold pressure to obtain the same final pressure (4 torr) corresponding to the equivalent characteristic point in the adsorption isotherm for all samples irrespective of ZIF-8 content.

The evolution of pressure was reproducibly recorded in this manner and showed significant differences among the various polymers which were used to identify PVP to be the best carrier polymers for the desired application. Nevertheless, the exact interpretation on a molecular scale was obviously more difficult, as no model exists and the contributions from the superimposed processes are hard to separate.

6.1.17 RuO₂ nanotubes and Ru_xTi_{1-x}O₂ nanofibers

Similarly to the case of Pt(acac)₂ [see chapter 6.1.9], it was possible to electrospin nanofibers containing Ru(acac)₃, but no RuO₂ fibers were obtained after calcination, as most of the precursor sublimated.

Using RuCl₃ · H₂O as precursor led to electropray rather than to electrospinning, as the conductivity of spinning solution was too high.

To decrease its conductivity, a solution of 50-90 mg (0.22-0.4 mmol) RuCl₃ · H₂O was refluxed in 200 mg DMF at 125 °C to produce a Ru-DMF complex and HCl gas was expelled. By adding 20 mg AcOH before refluxing, it was possible to increase the release of the HCl.

Then 300 mg ethanol and 200 mg of 12 wt% polyvinylpyrrolidone in methanol were added and mixed vigorously. After calcination at 475°C for 30 min (ramp of 5 °C/min) hollow nanotubes were observed, especially if low amounts of precursor were used.

Adding 25 mg H₂O or using polyvinylbutyral (PVB, Mowital® B60 H) as spinning polymer resulted in compact nanofibers instead of nanotubes.

The electrospinning parameters were as follows:

Voltage: 5 kV
Distance: 6 cm
Feed rate: 0.3 ml/h
Relative humidity: < 25%

The Ru_xTi_{1-x}O₂ nanofibers could be prepared by adding the appropriate amount of Ti(OiPr)₄ after refluxing. In case of $x < 0.2$ it was also possible to use RuCl₃ · H₂O as precursor without refluxing.

6.1.18 Fe₂O₃ nanofibers and nanotubes

After initially using Fe(NO₃)₃ · x H₂O to prepare a Fe-DMF complex, it was observed that the resulting nanotubes were better developed if anhydrous FeCl₃ was employed as precursor.

In a typical experiment, 50 mg FeCl₃ were refluxed in 250 mg DMF at 125 °C for 15 min, before adding 500 mg EtOH and 1200 mg 12 wt% PVP in EtOH.

When left in a sealed container, the yellow solution turned colorless (which did not affect the spinning).

The electrospinning parameters were as follows:

Voltage:	4.5 kV
Distance:	6 cm
Feed rate:	0.55 ml/h
Relative humidity:	< 20%

Directly after electrospinning, the composite fibers were stabilized at 125°C for 30 min, before heating them to 425°C for 60 min (rate of 5°C min).

The obtained nanotubes were of bright red color.

Increasing the amount of iron precursor or adding water to the recipe resulted in compact nanofibers.

Furthermore, it was possible to substitute a fraction of the iron precursor with RuCl₃ · H₂O to prepare mixed Ru_xFe_yO_z nanotubes, but their structure was not investigated in detail.

6.1.19 NiO and Co₂O₃ nanotubes

Similarly to Fe₂O₃, nanotubes of NiO and Co₂O₃ could be obtained from PVP nanofibers containing the respective DMF complexes.

Most work was focused on the iron oxide nanotubes and the analogue nickel and cobalt oxides have only been prepared from the respective nitrates. The higher water content led to the formation of less defined tubes. However, it should be possible to improve the results by using anhydrous precursor.

75 mg Ni(NO₃)₂ · x H₂O were refluxed in 250 mg DMF at 125 °C for 15 min, before adding 500 mg EtOH and 1200 mg 12 wt% PVP in EtOH.

The electrospinning parameters were as follows:

Voltage:	4.5 kV
Distance:	6 cm
Feed rate:	0.45 ml/h
Relative humidity:	< 20%

Directly after electrospinning, the composite fibers were stabilized at 125°C for 30 min, before heating them to 425°C for 60 min (rate of 5°C min).

Similarly, Co₂O₃ nanotubes could be prepared from 70 mg Co(NO₃)₂ · x H₂O.

6.2 Abbreviations and Glossary

AcOH	Acetic acid	PEO	Polyethylene oxide
ATO	Antimony Tin Oxide	PVB	Polyvinylbutyral
AZO	Aluminum Zinc Oxide	PVP	Polyvinylpyrrolidone
CHCl ₃	Chloroform	RH	relative humidity
DCM	Dichlormethane	RhB	Rhodamin B
DMF	Dimethylformamide	SAXS	Small-angle X-Ray scattering
DSSC	Dye-sensitized solar cell	SEM	scanning electron microscope
Et ₂ O	Diethylether	TCO	Transparent Conducting Oxide
EtOH	Ethanol	TEM	tunneling electron microscope
FTO	Fluorine Tin Oxide	TiO ₂	Titanium dioxide
h	hour(s)	vol%	volume percent
H ₂ O	Water	WAXS	Wide-angle X-Ray scattering
iPrOH	Isopropanol	wt%	weight percent
ITO	Indium Tin Oxide	XRD	X-Ray diffraction
IZO	Indium Zinc Oxide	ZIF	Zeolitic imidazolate framework
MeOH	Methanol		
min	minute(s)		
MOF	Metal Organic Framework		
M _w	Weight average of molecular weight		
NP	nanoparticle		

6.3 References

- [1] R. Feynman, "There's plenty of room at the bottom," *Eng. Sci.*, vol. 23, no. 5, pp. 269-283, 1960.
- [2] S. Becht, S. Ernst, R. Bappert and C. Feldmann, "Nanomaterialien zum Anfassen. Do-it-yourself !," *Chemie in unserer Zeit*, vol. 44, no. 1, pp. 14-23, 2010.
- [3] A. Greiner and J. Wendorff, "Electrospinning: A Fascinating Method for the Preparation of Ultrathin Fibers," *Angewandte Chemie International Edition*, vol. 46, no. 30, pp. 5670-5703, 2007.
- [4] C. E. Bakis et al., "Fiber-Reinforced Polymer Composites for Construction - State-of-the-Art Review," *Journal of Composites for Construction*, vol. 6, no. 2, pp. 73-87, 2002.
- [5] M. M. Bergshoef and G. J. Vancso, "Transparent Nanocomposites with Ultrathin, Electrospun Nylon-4,6 Fiber Reinforcement," *Advanced Materials*, vol. 11, no. 16, pp. 1362-1365, 1999.
- [6] J. Sandler, J. Kirk, I. Kinloch, M. Shaffer and A. Windle, "Ultra-low electrical percolation threshold in carbon-nanotube-epoxy composites," *Polymer*, vol. 44, no. 19, pp. 5893-5899, Sep. 2003.
- [7] J. Cooley, "Apparatus for electrically dispersing fluids," U.S. Patent 692631, 10-Jun-1899.
- [8] A. Formhals, "Verfahren und Vorrichtung zur Herstellung von kuenstlichen Fasern," German Patent 584801, 12-Aug-1929.
- [9] A. Formhals, "Process and Apparatus for preparing artificial threads," U.S. Patent 1975504, 12-May-1930.
- [10] G. Taylor, "Electrically Driven Jets," *Proceedings of the Royal Society of London. A. Mathematical and Physical Sciences*, vol. 313, no. 1515, pp. 453 -475, Dec. 1969.
- [11] D. H. Reneker and A. L. Yarin, "Electrospinning jets and polymer nanofibers," *Polymer*, vol. 49, no. 10, pp. 2387-2425, 2008.
- [12] D. Li and Y. Xia, "Electrospinning of Nanofibers: Reinventing the Wheel?," *Advanced Materials*, vol. 16, no. 14, pp. 1151-1170, 2004.
- [13] J. Gatford, "Diagramm of the electrospinning process," The New Zealand Institute for Plant and Food Research Ltd, 2008.
- [14] A. Holzmeister, M. Rudisile, A. Greiner and J. H. Wendorff, "Structurally and chemically heterogeneous nanofibrous nonwovens via electrospinning," *European Polymer Journal*, vol. 43, no. 12, pp. 4859-4867, Dec. 2007.

- [15] H. Fong, I. Chun and D. H. Reneker, "Beaded nanofibers formed during electrospinning," *Polymer*, vol. 40, no. 16, pp. 4585-4592, Jul. 1999.
- [16] S. Koombhongse, W. Liu and D. H. Reneker, "Flat polymer ribbons and other shapes by electrospinning," *Journal of Polymer Science Part B: Polymer Physics*, vol. 39, no. 21, pp. 2598-2606, 2001.
- [17] R. A. Caruso, J. H. Schattka and A. Greiner, "Titanium Dioxide Tubes from Sol-Gel Coating of Electrospun Polymer Fibers," *Advanced Materials*, vol. 13, no. 20, p. 1577, 2001.
- [18] D. Li and Y. Xia, "Fabrication of Titania Nanofibers by Electrospinning," *Nano Letters*, vol. 3, no. 4, pp. 555-560, Apr. 2003.
- [19] D. Li and Y. Xia, "Direct Fabrication of Composite and Ceramic Hollow Nanofibers by Electrospinning," *Nano Letters*, vol. 4, no. 5, pp. 933-938, Mai. 2004.
- [20] K. Sawicka, A. Prasad and P. Gouma, "Metal Oxide Nanowires for Use in Chemical Sensing Applications," *Sensor Letters*, vol. 3, no. 1, pp. 31-35, 2005.
- [21] S. Madhugiri, B. Sun, P. G. Smirniotis, J. P. Ferraris, K. J. Balkus, "Electrospun mesoporous titanium dioxide fibers," *Microporous and Mesoporous Materials*, vol. 69, no. 1, pp. 77-83, Apr. 2004.
- [22] K. Onozuka et al., "Electrospinning processed nanofibrous TiO₂ membranes for photovoltaic applications," *Nanotechnology*, vol. 17, no. 4, pp. 1026-1031, 2006.
- [23] N. Yu, C. Shao, Y. Liu, H. Guan and X. Yang, "Nanofibers of LiMn₂O₄ by electrospinning," *Journal of Colloid and Interface Science*, vol. 285, no. 1, pp. 163-166, May. 2005.
- [24] J. Yuh, L. Perez, W. Sigmund and J. Nino, "Electrospinning of complex oxide nanofibers," *Physica E: Low-dimensional Systems and Nanostructures*, vol. 37, no. 1, pp. 254-259, 2007.
- [25] R. Ostermann, D. Li, Y. Yin, J. T. McCann and Y. Xia, "V₂O₅ Nanorods on TiO₂ Nanofibers: A New Class of Hierarchical Nanostructures Enabled by Electrospinning and Calcination," *Nano Letters*, vol. 6, no. 6, pp. 1297-1302, Jun. 2006.
- [26] T. Minami, "Transparent conducting oxide semiconductors for transparent electrodes," *Semiconductor Science and Technology*, vol. 20, no. 4, pp. S35-S44, 2005.
- [27] P. P. Edwards, A. Porch, M. O. Jones, D. V. Morgan and R. M. Perks, "Basic materials physics of transparent conducting oxides," *Dalton Transactions*, no. 19, pp. 2995-3002, 2004.
- [28] C. G. Granqvist, "Transparent conductive electrodes for electrochromic devices: A review," *Applied Physics A: Materials Science & Processing*, vol. 57, no. 1, pp. 19-24, Jul. 1993.
- [29] E. Fortunato, D. Ginley, H. Hosono and D. C. Paine, "Transparent conducting oxides for photovoltaics," *MRS BULLETIN*, vol. 32, no. 3, pp. 242-247, 2007.

- [30] S. Chappel, L. Grinis, A. Ofir and A. Zaban, "Extending the Current Collector into the Nanoporous Matrix of Dye Sensitized Electrodes," *The Journal of Physical Chemistry B*, vol. 109, no. 5, pp. 1643-1647, Feb. 2005.
- [31] L. Grinis, A. Ofir, S. Dor, S. Yahav and A. Zaban, "Collector-Shell Mesoporous Electrodes for Dye Sensitized Solar Cells," *ISRAEL JOURNAL OF CHEMISTRY*, vol. 48, no. 3, pp. 269-275, 2008.
- [32] E. Joanni et al., "Dye-sensitized solar cell architecture based on indium-tin oxide nanowires coated with titanium dioxide," *Scripta Materialia*, vol. 57, no. 3, pp. 277 - 280, 2007.
- [33] D. Fattakhova-Rohlfing et al., "Transparent Conducting Films of Indium Tin Oxide with 3D Mesopore Architecture," *Advanced Materials*, vol. 18, no. 22, pp. 2980-2983, 2006.
- [34] T. T. Emons, J. Li and L. F. Nazar, "Synthesis and Characterization of Mesoporous Indium Tin Oxide Possessing an Electronically Conductive Framework," *Journal of the American Chemical Society*, vol. 124, no. 29, pp. 8516-8517, Jul. 2002.
- [35] X. Zhang, Y. Man, J. Wang, C. Liu and W. Wu, "Synthesis of 3D ordered macroporous indium tin oxide using polymer colloidal crystal template," *Science in China Series E: Technological Sciences*, vol. 49, no. 5, pp. 537-546, 2006.
- [36] H. Wang et al., "Three-dimensional electrodes for dye-sensitized solar cells: synthesis of indium-tin-oxide nanowire arrays and ITO/TiO₂ core-shell nanowire arrays by electrophoretic deposition," *Nanotechnology*, vol. 20, no. 5, p. 055601, 2009.
- [37] S. Shah and A. Revzin, "Patterning Cells on Optically Transparent Indium Tin Oxide Electrodes," *Journal of Visualized Experiments : JoVE*, no. 7.
- [38] H. Bisht, H. Eun, A. Mehrtens and M. A. Aegerter, "Comparison of spray pyrolyzed FTO, ATO and ITO coatings for flat and bent glass substrates," *Thin Solid Films*, vol. 351, no. 1, pp. 109-114, Aug. 1999.
- [39] H. Kim et al., "Effect of aluminum doping on zinc oxide thin films grown by pulsed laser deposition for organic light-emitting devices," *Thin Solid Films*, vol. 377, pp. 798-802, 2000.
- [40] A. Suzuki, T. Matsushita, T. Aoki, A. Mori and M. Okuda, "Highly conducting transparent indium tin oxide films prepared by pulsed laser deposition," *Thin Solid Films*, vol. 411, no. 1, pp. 23-27, 2002.
- [41] C. Goebbert, R. Nonninger, M. A. Aegerter and H. Schmidt, "Wet chemical deposition of ATO and ITO coatings using crystalline nanoparticles redispersable in solutions," *THIN SOLID FILMS*, vol. 351, no. 1, pp. 79-84, Aug. 1999.
- [42] E. Shanthi, V. Dutta, A. Banerjee and K. L. Chopra, "Electrical and optical properties of undoped and antimony-doped tin oxide films," *Journal of Applied Physics*, vol. 51, no. 12, pp. 6243-6251, 1980.

- [43] S. Kang, X. Wu, Z. Cui and J. Mu, "Effect of Erbium Dopant on Conductivity of Antimony-Doped Tin Oxide (ATO) Nanoparticles," *Journal of Dispersion Science and Technology*, vol. 28, no. 6, p. 869, 2007.
- [44] R. Ostermann, M. Rudolph, D. Schlettwein and B. M. Smarsly, "Novel Nanostructured Photoelectrodes - Electrodeposition of metal oxides onto transparent conducting oxide nanofibers," *Mater. Res. Soc. Symp. Proc.*, vol. 1211, pp. R07-03, 2010.
- [45] J. Jolivet, *Metal Oxide Chemistry and Synthesis: From Solution to Solid State*, 1st ed. Wiley, 2000.
- [46] L. Kavan, B. O'Regan, A. Kay and M. Graetzel, "Preparation of TiO₂ (anatase) films on electrodes by anodic oxidative hydrolysis of TiCl₃," *Journal of electroanalytical chemistry*, vol. 346, no. 1, pp. 291-307, Mar. 1993.
- [47] K. Wessels, A. Feldhoff, M. Wark, J. Rathousky and T. Oekermann, "Low-temperature preparation of crystalline nanoporous TiO₂ films by surfactant-assisted anodic electrodeposition," *ELECTROCHEMICAL AND SOLID STATE LETTERS*, vol. 9, no. 6, pp. C93-C96, 2006.
- [48] M. Y. Song, D. K. Kim, K. J. Ihn, S. M. Jo and D. Y. Kim, "Electrospun TiO₂ electrodes for dye-sensitized solar cells," *Nanotechnology*, vol. 15, no. 12, pp. 1861-1865, 2004.
- [49] J. B. Baxter and E. S. Aydil, "Nanowire-based dye-sensitized solar cells," *Applied Physics Letters*, vol. 86, no. 5, pp. 053114-3, Jan. 2005.
- [50] S. K. Deb, "Photoconductivity and photoluminescence in amorphous titanium dioxide," *Solid State Communications*, vol. 11, no. 5, pp. 713-715, Sep. 1972.
- [51] J. Nelson, A. M. Eppler and I. M. Ballard, "Photoconductivity and charge trapping in porous nanocrystalline titanium dioxide," *Journal of Photochemistry and Photobiology A: Chemistry*, vol. 148, no. 1, pp. 25-31, 2002.
- [52] A. M. Eppler, I. M. Ballard and J. Nelson, "Charge transport in porous nanocrystalline titanium dioxide," *Physica E: Low-dimensional Systems and Nanostructures*, vol. 14, no. 1, pp. 197-202, 2002.
- [53] P. E. de Jongh and D. Vanmaekelbergh, "Trap-Limited Electronic Transport in Assemblies of Nanometer-Size TiO₂ Particles," *Physical Review Letters*, vol. 77, no. 16, p. 3427, 1996.
- [54] R. Solarska, J. Augustynski and K. Sayama, "Viewing nanocrystalline TiO₂ photoelectrodes as three-dimensional electrodes: Effect of the electrolyte upon the photocurrent efficiency," *Electrochimica Acta*, vol. 52, no. 2, pp. 694-703, 2006.
- [55] J. Bisquert, D. Cahen, G. Hodes, S. Ruhle and A. Zaban, "Physical Chemical Principles of Photovoltaic Conversion with Nanoparticulate, Mesoporous Dye-Sensitized Solar Cells," *The Journal of Physical Chemistry B*, vol. 108, no. 24, pp. 8106-8118, Jun. 2004.

- [56] R. Solarska, I. Rutkowska and J. Augustynski, "Unusual photoelectrochemical behaviour of nanocrystalline TiO₂ films," *Inorganica Chimica Acta*, vol. 361, no. 3, pp. 792-797, Feb. 2008.
- [57] D. Vollath, *Nanomaterials: An Introduction to Synthesis, Properties and Applications*, 1st ed. Wiley-VCH Verlag GmbH & Co. KGaA, 2008.
- [58] J. K. W. Sandler, J. E. Kirk, I. A. Kinloch, M. S. P. Shaffer and A. H. Windle, "Ultra-low electrical percolation threshold in carbon-nanotube-epoxy composites," *Polymer*, vol. 44, no. 19, pp. 5893-5899, Sep. 2003.
- [59] E. Hecht, *Optics*, 4th ed. Pearson, 2003.
- [60] G. W. Becker, D. Braun, H. Gausepohl and R. Gellert, *Kunststoffhandbuch, 11 Bde. in 17 Tl.-Bdn., Bd.4, Polystyrol*. Hanser Fachbuch, 1995.
- [61] D. C. Giancoli, *Physics for Scientists & Engineers with Modern Physics*, 4th ed. Prentice Hall, 2008.
- [62] E. Shanthi, "Electrical and optical properties of tin oxide films doped with F and (Sb+F)," *Journal of Applied Physics*, vol. 53, no. 3, p. 1615, 1982.
- [63] A. Thess et al., "Crystalline Ropes of Metallic Carbon Nanotubes," *Science*, vol. 273, no. 5274, pp. 483-487, Jul. 1996.
- [64] W. D. Ryden, A. W. Lawson and C. C. Sartain, "Electrical Transport Properties of IrO₂ and RuO₂," *Physical Review B*, vol. 1, no. 4, p. 1494, Feb. 1970.
- [65] S. Zhao, B. Guo, G. Han and Y. Tian, "Metallization of electrospun polyacrylonitrile fibers by gold," *Materials Letters*, vol. 62, no. 21, pp. 3751-3753, 2008.
- [66] M. Jin et al., "Large-scale fabrication of Ag nanoparticles in PVP nanofibres and net-like silver nanofibre films by electrospinning," *Nanotechnology*, vol. 18, no. 7, p. 075605, 2007.
- [67] M. Bognitzki et al., "Preparation of Sub-micrometer Copper Fibers via Electrospinning," *Advanced Materials*, vol. 18, no. 18, pp. 2384-2386, 2006.
- [68] N. A. M. Barakat, B. Kim and H. Y. Kim, "Production of Smooth and Pure Nickel Metal Nanofibers by the Electrospinning Technique: Nanofibers Possess Splendid Magnetic Properties," *The Journal of Physical Chemistry C*, vol. 113, no. 2, pp. 531-536, Jan. 2009.
- [69] M. Graeser, M. Bognitzki, W. Massa, C. Pietzonka, A. Greiner and J. Wendorff, "Magnetically Anisotropic Cobalt and Iron Nanofibers via Electrospinning," *Advanced Materials*, vol. 19, no. 23, pp. 4244-4247, 2007.
- [70] H. Guan, C. Shao, B. Chen, J. Gong and X. Yang, "A novel method for making CuO superfine fibres via an electrospinning technique," *Inorganic Chemistry Communications*, vol. 6, no. 11, pp. 1409-1411, 2003.
- [71] H. Wu, D. Lin and W. Pan, "Fabrication, assembly and electrical characterization of CuO nanofibers," *Applied Physics Letters*, vol. 89, no. 13, p. 133125, 2006.

- [72] W. Wang, L. Zhang, S. Tong, X. Li and W. Song, "Three-dimensional network films of electrospun copper oxide nanofibers for glucose determination," *Biosensors and Bioelectronics*, vol. 25, no. 4, pp. 708-714, 2009.
- [73] J. Shui and J. C. M. Li, "Platinum Nanowires Produced by Electrospinning," *Nano Letters*, vol. 9, no. 4, pp. 1307-1314, 2009.
- [74] R. Gentsch, B. Boysen, A. Lanckenau and H. G. Börner, "Single-Step Electrospinning of Bimodal Fiber Meshes for Ease of Cellular Infiltration," *Macromolecular Rapid Communications*, vol. 31, no. 1, pp. 59-64, 2010.
- [75] F. Schuth, "Engineered Porous Catalytic Materials," *Annual Review of Materials Research*, vol. 35, no. 1, pp. 209-238, 2005.
- [76] C. Yu, "Recent advances in the synthesis of non-siliceous mesoporous materials," *Current Opinion in Solid State and Materials Science*, vol. 7, no. 3, pp. 191-197, 2003.
- [77] M. E. Davis, "Ordered porous materials for emerging applications," *Nature*, vol. 417, no. 6891, pp. 813-821, Jun. 2002.
- [78] B. Smarsly and M. Antonietti, "Block Copolymer Assemblies as Templates for the Generation of Mesoporous Inorganic Materials and Crystalline Films," *European Journal of Inorganic Chemistry*, vol. 2006, no. 6, pp. 1111-1119, 2006.
- [79] C. J. Brinker, Y. Lu, A. Sellinger and H. Fan, "Evaporation-Induced Self-Assembly: Nanostructures Made Easy," *Advanced Materials*, vol. 11, no. 7, pp. 579-585, 1999.
- [80] M. Choi, K. Na, J. Kim, Y. Sakamoto, O. Terasaki and R. Ryoo, "Stable single-unit-cell nanosheets of zeolite MFI as active and long-lived catalysts," *Nature*, vol. 461, no. 7261, pp. 246-249, 2009.
- [81] K. Egeblad, C. H. Christensen, M. Kustova and C. H. Christensen, "Templating Mesoporous Zeolites," *Chemistry of Materials*, vol. 20, no. 3, pp. 946-960, Feb. 2008.
- [82] O. Sel, A. Brandt, D. Wallacher, M. Thommes and B. Smarsly, "Pore Hierarchy in Mesoporous Silicas Evidenced by In-Situ SANS during Nitrogen Physisorption," *Langmuir*, vol. 23, no. 9, pp. 4724-4727, Apr. 2007.
- [83] S. Mascotto et al., "Analysis of Microporosity in Ordered Mesoporous Hierarchically Structured Silica by Combining Physisorption With in Situ Small-Angle Scattering (SAXS and SANS)," *Langmuir*, vol. 25, no. 21, pp. 12670-12681, Nov. 2009.
- [84] K. Nakanishi and N. Soga, "Phase separation in silica sol-gel system containing polyacrylic acid I. Gel formation behavior and effect of solvent composition," *Journal of Non-Crystalline Solids*, vol. 139, pp. 1-13, 1992.
- [85] D. Lubda, K. Cabrera, K. Nakanishi and H. Minakuchi, "Monolithic HPLC Silica Columns," *Journal of Sol-Gel Science and Technology*, vol. 23, no. 2, pp. 185-187, Feb. 2002.
- [86] J. Bear, *Dynamics of Fluids in Porous Media*. Dover Publications, 1988.

- [87] M. Macías, A. Chacko, J. P. Ferraris, K. J. Balkus, "Electrospun mesoporous metal oxide fibers," *Microporous and Mesoporous Materials*, vol. 86, no. 1, pp. 1-13, Nov. 2005.
- [88] K. Nakanishi and N. Soga, "Phase Separation in Gelling Silica-Organic Polymer Solution: Systems Containing Poly(sodium styrenesulfonate)," *Journal of the American Ceramic Society*, vol. 74, no. 10, pp. 2518-2530, 1991.
- [89] K. Nakanishi and N. Tanaka, "Sol-Gel with Phase Separation. Hierarchically Porous Materials Optimized for High-Performance Liquid Chromatography Separations," *Accounts of Chemical Research*, vol. 40, no. 9, pp. 863-873, 2007.
- [90] D. Li and Y. Xia, "Fabrication of Titania Nanofibers by Electrospinning," *Nano Letters*, vol. 3, no. 4, pp. 555-560, Apr. 2003.
- [91] A. V. Bazilevsky, A. L. Yarin and C. M. Megaridis, "Co-Electrospinning of Core-Shell Fibers Using a Single-Nozzle Technique," *Langmuir*, vol. 23, no. 5, pp. 2311-2314, Feb. 2007.
- [92] M. Niederberger, M. H. Bartl and G. D. Stucky, "Benzyl Alcohol and Transition Metal Chlorides as a Versatile Reaction System for the Nonaqueous and Low-Temperature Synthesis of Crystalline Nano-Objects with Controlled Dimensionality," *Journal of the American Chemical Society*, vol. 124, no. 46, pp. 13642-13643, Nov. 2002.
- [93] M. Niederberger, M. H. Bartl and G. D. Stucky, "Benzyl Alcohol and Titanium Tetrachloride - A Versatile Reaction System for the Nonaqueous and Low-Temperature Preparation of Crystalline and Luminescent Titania Nanoparticles," *Chemistry of Materials*, vol. 14, no. 10, pp. 4364-4370, 2002.
- [94] M. Kanehata, B. Ding and S. Shiratori, "Nanoporous ultra-high specific surface inorganic fibres," *Nanotechnology*, vol. 18, no. 31, p. 315602, 2007.
- [95] W. Stöber, A. Fink and E. Bohn, "Controlled growth of monodisperse silica spheres in the micron size range," *Journal of Colloid and Interface Science*, vol. 26, no. 1, pp. 62-69, Jan. 1968.
- [96] K. Nozawa et al., "Smart Control of Monodisperse Stöber Silica Particles: Effect of Reactant Addition Rate on Growth Process," *Langmuir*, vol. 21, no. 4, pp. 1516-1523, Feb. 2005.
- [97] D. Fattakhova-Rohlfing, J. M. Szeifert, Q. Yu, V. Kalousek, J. Rathouský and T. Bein, "Low-Temperature Synthesis of Mesoporous Titania-Silica Films with Pre-Formed Anatase Nanocrystals," *Chemistry of Materials*, vol. 21, no. 12, pp. 2410-2417, Jun. 2009.
- [98] C. Wessel et al., "Ionic-Liquid Synthesis Route of TiO₂(B) Nanoparticles for Functionalized Materials," *Chemistry - A European Journal*, vol. 17, no. 3, pp. 775-779, 2011.
- [99] D. Reyes-Coronado, G. Rodríguez-Gattorno, M. E. Espinosa-Pesqueira, C. Cab, R. de Coss and G. Oskam, "Phase-pure TiO₂ nanoparticles: anatase, brookite and rutile," *Nanotechnology*, vol. 19, no. 14, p. 145605, 2008.

- [100] A. Fujishima and K. Honda, "Electrochemical Photolysis of Water at a Semiconductor Electrode," *Nature*, vol. 238, no. 5358, pp. 37-38, 1972.
- [101] M. R. Hoffmann, S. T. Martin, W. Choi and D. W. Bahnemann, "Environmental Applications of Semiconductor Photocatalysis," *Chemical Reviews*, vol. 95, no. 1, pp. 69-96, Jan. 1995.
- [102] D. Zhang, T. Yoshida, T. Oekermann, K. Furuta and H. Minoura, "Room-Temperature Synthesis of Porous Nanoparticulate TiO₂ Films for Flexible Dye-Sensitized Solar Cells," *Advanced Functional Materials*, vol. 16, no. 9, pp. 1228-1234, 2006.
- [103] S. Zhan, D. Chen, X. Jiao and C. Tao, "Long TiO₂ Hollow Fibers with Mesoporous Walls: Sol-Gel Combined Electrospun Fabrication and Photocatalytic Properties," *The Journal of Physical Chemistry B*, vol. 110, no. 23, pp. 11199-11204, Jun. 2006.
- [104] D. Yang et al., "An Efficient Photocatalyst Structure: TiO₂(B) Nanofibers with a Shell of Anatase Nanocrystals," *Journal of the American Chemical Society*, vol. 131, no. 49, pp. 17885-17893, 2009.
- [105] Y. Wang, K. Jacobi, W. Schöne and G. Ertl, "Catalytic Oxidation of Ammonia on RuO₂(110) Surfaces: Mechanism and Selectivity," *The Journal of Physical Chemistry B*, vol. 109, no. 16, pp. 7883-7893, Apr. 2005.
- [106] A. Seitsonen et al., "Reaction mechanism of ammonia oxidation over RuO₂(1 1 0): A combined theory/experiment approach," *Surface Science*, vol. 603, no. 18, pp. L113-L116, Sep. 2009.
- [107] T. Teranishi and M. Miyake, "Size Control of Palladium Nanoparticles and Their Crystal Structures," *Chemistry of Materials*, vol. 10, no. 2, pp. 594-600, Feb. 1998.
- [108] R. Ostermann, J. Cravillon, C. Weidmann, M. Wiebcke and B. M. Smarsly, "Metal-organic framework nanofibers via electrospinning," *Chemical Communications*, vol. 47, no. 1, p. 442, 2011.
- [109] Z. Qi, H. Yu, Y. Chen and M. Zhu, "Highly porous fibers prepared by electrospinning a ternary system of nonsolvent/solvent/poly(l-lactic acid)," *Materials Letters*, vol. 63, no. 3, pp. 415-418, Feb. 2009.
- [110] M. Bognitzki et al., "Nanostructured Fibers via Electrospinning," *Advanced Materials*, vol. 13, no. 1, pp. 70-72, 2001.
- [111] M. Bognitzki et al., "Preparation of fibers with nanoscaled morphologies: Electrospinning of polymer blends," *Polymer Engineering & Science*, vol. 41, no. 6, pp. 982-989, 2001.
- [112] J. T. McCann, M. Marquez and Y. Xia, "Highly Porous Fibers by Electrospinning into a Cryogenic Liquid," *Journal of the American Chemical Society*, vol. 128, no. 5, pp. 1436-1437, Feb. 2006.
- [113] A. Gupta, C. D. Saquing, M. Afshari, A. E. Tonelli, S. A. Khan and R. Kotek, "Porous Nylon-6 Fibers via a Novel Salt-Induced Electrospinning Method," *Macromolecules*, vol. 42, no. 3, pp. 709-715, Feb. 2009.

- [114] T. v. Graberg, A. Thomas, A. Greiner, M. Antonietti and J. Weber, "Electrospun Silica - Polybenzimidazole Nanocomposite Fibers," *Macromolecular Materials and Engineering*, vol. 293, no. 10, pp. 815-819, 2008.
- [115] Z. Zhang, X. Li, C. Wang, S. Fu, Y. Liu and C. Shao, "Polyacrylonitrile and Carbon Nanofibers with Controllable Nanoporous Structures by Electrospinning," *Macromolecular Materials and Engineering*, vol. 294, no. 10, pp. 673-678, 2009.
- [116] N. B. McKeown, S. Hanif, K. Msayib, C. E. Tattershall and P. M. Budd, "Porphyrin-based nanoporous network polymers," *Chemical Communications*, no. 23, pp. 2782-2783, 2002.
- [117] P. M. Budd et al., "Solution-Processed, Organophilic Membrane Derived from a Polymer of Intrinsic Microporosity," *Advanced Materials*, vol. 16, no. 5, pp. 456-459, 2004.
- [118] N. B. McKeown et al., "Towards Polymer-Based Hydrogen Storage Materials: Engineering Ultramicroporous Cavities within Polymers of Intrinsic Microporosity¹³," *Angewandte Chemie International Edition*, vol. 45, no. 11, pp. 1804-1807, 2006.
- [119] G. Ferey, "Hybrid porous solids: past, present, future," *Chemical Society Reviews*, vol. 37, no. 1, pp. 191-214, 2008.
- [120] A. Phan, C. J. Doonan, F. J. Uribe-Romo, C. B. Knobler, M. O'Keeffe and O. M. Yaghi, "Synthesis, Structure, and Carbon Dioxide Capture Properties of Zeolitic Imidazolate Frameworks," *Accounts of Chemical Research*, vol. 43, no. 1, pp. 58-67, Jan. 2010.
- [121] J. Cravillon, S. Muenzer, S. Lohmeier, A. Feldhoff, K. Huber and M. Wiebcke, "Rapid Room-Temperature Synthesis and Characterization of Nanocrystals of a Prototypical Zeolitic Imidazolate Framework," *Chemistry of Materials*, vol. 21, no. 8, pp. 1410-1412, Apr. 2009.
- [122] K. S. Park et al., "Exceptional chemical and thermal stability of zeolitic imidazolate frameworks," *Proceedings of the National Academy of Sciences*, vol. 103, no. 27, pp. 10186-10191, Jul. 2006.
- [123] C. E. Powell and G. G. Qiao, "Polymeric CO₂/N₂ gas separation membranes for the capture of carbon dioxide from power plant flue gases," *Journal of Membrane Science*, vol. 279, no. 1, pp. 1-49, Aug. 2006.
- [124] K. Müller, J. F. Quinn, A. P. R. Johnston, M. Becker, A. Greiner and F. Caruso, "Polyelectrolyte Functionalization of Electrospun Fibers," *Chemistry of Materials*, vol. 18, no. 9, pp. 2397-2403, 2006.
- [125] I. Chorkendorff and J. W. Niemantsverdriet, *Concepts of Modern Catalysis and Kinetics*, 2nd ed. Wiley-VCH Verlag GmbH & Co. KGaA, 2007.
- [126] G. Ertl, H. Knözinger, F. Schüth and J. Weitkamp, *Handbook of Heterogeneous Catalysis, 8 Volumes*, 2nd ed. Wiley-VCH, 2008.
- [127] O. Nilsen, A. Kjekshus and H. Fjellvåg, "Reconstruction and loss of platinum catalyst during oxidation of ammonia," *Applied Catalysis A: General*, vol. 207, no. 1, pp. 43-54, Feb. 2001.

- [128] R. J. Judd et al., "Syntheses and Crystal and Molecular Structures of the Hexakis(N,N-dimethylformamide) Complexes of Ruthenium(II) and Ruthenium(III)," *Inorganic Chemistry*, vol. 34, no. 20, pp. 5080-5083, 1995.
- [129] F. Allen, "Chemical Classics: Henry Deacon," *Chemistry in Action*, vol. 68, p. 25, 2002.
- [130] I. Kiyoshi et al., "The Development of Improved Hydrogen Chloride Oxidation Process," *Sumitomo Kagaku*, vol. 2004, no. 1, pp. 4-12, 2004.
- [131] D. Li and Y. Xia, "Direct Fabrication of Composite and Ceramic Hollow Nanofibers by Electrospinning," *Nano Letters*, vol. 4, no. 5, pp. 933-938, 2004.
- [132] Z. Sun, E. Zussman, A. Yarin, J. Wendorff and A. Greiner, "Compound Core-Shell Polymer Nanofibers by Co-Electrospinning," *Advanced Materials*, vol. 15, no. 22, pp. 1929-1932, 2003.
- [133] L. C. Lopérgolo, A. B. Lugão and L. H. Catalani, "Direct UV photocrosslinking of poly(N-vinyl-2-pyrrolidone) (PVP) to produce hydrogels," *Polymer*, vol. 44, no. 20, pp. 6217-6222, Sep. 2003.
- [134] C. Pai, M. C. Boyce and G. C. Rutledge, "Morphology of Porous and Wrinkled Fibers of Polystyrene Electrospun from Dimethylformamide," *Macromolecules*, vol. 42, no. 6, pp. 2102-2114, 2009.
- [135] M. M. Demir, "Investigation on glassy skin formation of porous polystyrene fibers electrospun from DMF," *eXPRESS Polymer Letters*, vol. 4, no. 1, pp. 2-8, 2009.
- [136] A. J. Guenther, S. Khombhongse, W. Liu, P. Dayal, D. H. Reneker and T. Kyu, "Dynamics of Hollow Nanofiber Formation During Solidification Subjected to Solvent Evaporation," *Macromolecular Theory and Simulations*, vol. 15, no. 1, pp. 87-93, 2006.
- [137] H. H. Huang et al., "Photochemical Formation of Silver Nanoparticles in Poly(N-vinylpyrrolidone)," *Langmuir*, vol. 12, no. 4, pp. 909-912, Jan. 1996.
- [138] Y. Sun and Y. Xia, "Shape-Controlled Synthesis of Gold and Silver Nanoparticles," *Science*, vol. 298, no. 5601, pp. 2176-2179, 2002.
- [139] S. Lahiri and S. Sarkar, "Separation of iron and cobalt using ^{59}Fe and ^{60}Co by dialysis of polyvinylpyrrolidone-metal complexes: A greener approach," *Applied Radiation and Isotopes*, vol. 65, no. 4, pp. 387-391, 2007.
- [140] Y. YAMASHITA, "Current State of Nanofiber Produced by Electrospinning and Prospects for Mass Production," *Journal of Textile Engineering*, vol. 54, no. 6, pp. 199-205, 2008.
- [141] J. Y. Park and S. S. Kim, "Effects of processing parameters on the synthesis of TiO_2 nanofibers by electrospinning," *Metals and Materials International*, vol. 15, no. 1, pp. 95-99, 2009.

- [142] M. T. Colomer, M. J. Velasco and J. R. Jurado, "Synthesis and thermal evolution of TiO₂-RuO₂ xerogels," *Journal of Sol-Gel Science and Technology*, vol. 39, no. 3, pp. 211-222, 2006.
- [143] P. Viswanathamurthi, N. Bhattarai, C. Kim, H. Kim and D. Lee, "Ruthenium doped TiO₂ fibers by electrospinning," *Inorganic Chemistry Communications*, vol. 7, no. 5, pp. 679-682, May. 2004.
- [144] E. Hammarberg, A. Prodi-Schwab and C. Feldmann, "Microwave-assisted polyol synthesis of aluminium- and indium-doped ZnO nanocrystals," *Journal of Colloid and Interface Science*, vol. 334, no. 1, pp. 29-36, Jun. 2009.
- [145] N. Wiberg, A. F. Holleman and E. Wiberg, *Holleman-Wiberg's Inorganic Chemistry*, 1st ed. Academic Press, 2001.
- [146] J. J. Garcia-Jareno, D. Benito, J. Navarro-Laboulais and F. Vicente, "Electrochemical Behavior of Electrodeposited Prussian Blue Films on ITO Electrode: An Attractive Laboratory Experience," *Journal of Chemical Education*, vol. 75, no. 7, p. 881, Jul. 1998.
- [147] B. Sun, B. Duan and X. Yuan, "Preparation of core/shell PVP/PLA ultrafine fibers by coaxial electrospinning," *Journal of Applied Polymer Science*, vol. 102, no. 1, pp. 39-45, 2006.
- [148] S. Park, G. G. Chase, K. Jeong and H. Y. Kim, "Mechanical properties of titania nanofiber mats fabricated by electrospinning of sol-gel precursor," *Journal of Sol-Gel Science and Technology*, vol. 54, no. 2, pp. 188-194, 2010.

6.4 Table of figures

Figure 1-1:	Examples of the size-dependent properties of nanomaterials: a) Spontaneous combustion of nanometric, pyrophoric iron in air b) CdSe quantum dots: The particle size determines the band gap between valence and conduction bands and thereby the color	1
Figure 1-2:	Packing density of curled fibers as a function of their tortuosity: The fibers are curled with a certain amplitude in the y direction, decreasing this amplitude results in more densely packed fiber mats ...	3
Figure 1-3:	a) Electrical conductivity of epoxy composites with aligned or entangled carbon nanotubes or carbon black as conducting filler b) Digital images of the aligned CNT-epoxy composites with different loadings of carbon nanotubes (CNT)	4
Figure 1-4:	The formation of nanofibers via the electrospinning process	5
Figure 1-5:	Scheme of a bending instability leading to thinning and elongation of the nanofiber and a stroboscopic picture showing several generations of bending instabilities that develop during the electrospinning process	6
Figure 1-6:	Scanning electron microscope (SEM) image of beaded and smooth nanofibers of PEO (polyethylene oxide) electrospun from aqueous solutions of low charge density and a) low (2 wt% PEO) and b) high (4 wt% PEO) viscosity	7
Figure 1-7:	a) Porous PLLA nanofibers electrospun from a solvent mixture ($\text{CH}_2\text{Cl}_2/\text{MeOH}$) resulting in polymer-rich and polymer-poor sections	8
Figure 2-1:	Flat and extended current collector for DSSC	10
Figure 2-2:	Comparison of resistance to electronic transport and diffusion for different electrode geometries: a) compact b) porous and c) porous with nanowires	11
Figure 2-3:	Scheme before and digital image after calcination of a) ITO nanofibers directly on the substrate and b) with a thin layer of the carrier polymer to reduce stress during calcination.....	13
Figure 2-4:	SEM image of an ITO nanofiber mat.....	14
Figure 2-5:	DSSC performance and SEM image of the first electrode composed of ITO nanofibers and mesoporous TiO_2	14
Figure 2-6:	SEM image of ITO nanofiber mat coated a) once and b) twice with mesoporous TiO_2 from nanoparticles.....	15

Figure 2-7:	SEM image of ITO nanofiber mat coated twice with mesoporous TiO ₂ , but scratched off the substrate to reveal the poor contact between ITO fibers and TiO ₂ matrix.....	16
Figure 2-8:	Development of the price of indium (99.99% purity, data from London Metal Exchange as of May, 2010)	17
Figure 2-9:	SEM image of ATO nanofibers prepared from nanoparticles	20
Figure 2-10:	XRD of nanoparticles as-prepared (25°C), after hydrothermal treatment (125°C for 3 h) and thermal treatment (550°C for 30 min). With cassiterite (SnO ₂) reference pattern from the JCPDS (Joint Committee of Powder Diffraction Standards) database.....	21
Figure 2-11:	ATO nanofiber electrode before and after PB electrodeposition: Scheme, SEMs and digital photograph of fiber mat used as electrode .	23
Figure 2-12:	a) Scheme and SEM of ATO nanofibers before and after electrodeposition of TiO ₂ from TiCl ₃	24
Figure 2-13:	SEM image of ATO nanofibers covered with TiO ₂ and results from DSSC photoelectrochemical measurement	25
Figure 2-14:	a) Electrical conductivity of epoxy composites with aligned or entangled carbon nanotubes or carbon black as conducting filler b) Digital images of the aligned CNT-epoxy composites with different loadings of carbon nanotubes (CNT)	28
Figure 2-15:	Digital photograph of ATO nanofiber mats a) in air and b) inside PS, c) of ATO-PS with a laser microscope and d) conductivity measurement.....	30
Figure 2-16:	SEM images of a) Pd and b) Pt nanofibers electrospun from PVP after polymer removal at 450°C	32
Figure 2-17:	Digital image of Pt nanofiber mats of different thickness deposited on glass slides	32
Figure 2-18:	SEM images of a) Prussian Blue deposited on Pt nanofibers and b) Pt nanofibers co-spun with thicker SiO ₂ nanofibers	33
Figure 2-19:	Pt-nanofibers-on-glas-electrode onto which the enzyme glucose oxidase has been electrodeposited in silica: a) AFM image and b) Typical response as electrocatalytic sensor	34
Figure 2-20:	Comparison of the performance of YSZ electrodes in a solid oxide fuel cell (SOFC) made with commercial Pt paste or electrospun Pt nanowires at 400 and 500°C	35
Figure 2-21:	Pt nanowires on YSZ a) as-prepared and b) after 5 h at 600°C	36
Figure 3-1:	Hierarchical structure of porous nanofibers offering high surface area and good accessibility	38

Figure 3-2:	SEM images of a) non-porous SiO ₂ fibers from PVP and b) templated TiO ₂ fibers from PVP-PS after calcination	40
Figure 3-3:	Schematic pathways to compact and porous nanofibers using demixing of polymer and preformed nanoparticles	42
Figure 3-4:	XRD analysis of TiO ₂ nanoparticles as synthesized at 80°C and 110°C	43
Figure 3-5:	SEM images of nanofibers after calcination at 550°C of TiO ₂ nanoparticles synthesized at a) 80°C and b) 110°C	44
Figure 3-6:	SEM images of nanofibers of TiO ₂ nanoparticles synthesized in benzyl alcohol and toluene at 110°C: a) before (with PVP) and b) after calcination at 500°C	45
Figure 3-7:	SEM images of nanofibers after calcination at 500°C: a) sol-gel-derived TiO ₂ and b) commercial nanoparticles dispersion	45
Figure 3-8:	Specific surface area as function of particle diameter compared to obtained results for the nanoparticle-based fibers.	47
Figure 3-9:	XRD analysis of TiO ₂ nanoparticles as synthesized at 110°C before and after calcination at 500°C (with measured background)	47
Figure 3-10:	SEM images of nanofibers from PVP and TiO ₂ nanoparticles synthesized at 110°C in benzyl alcohol/toluene a) after 6 h UV-C exposure and b) after additional washing with H ₂ O	50
Figure 3-11:	SEM images of nanofibers from TiO ₂ (B) nanoparticles a) as-synthesized with PVP and b) after 6 h UV-C exposure.....	51
Figure 3-12:	SEM images of nanofibers from TiO ₂ (B) nanoparticles functionalized with ethylene glycol and with additional 2.5 at% Ti(OiPr) ₄ as "glue" a) with PVP b) after 2 h UV-C exposure	52
Figure 3-13:	Scheme of catalytic nanofibers: a) sol-gel-derived compact fiber with metal nanoparticles inside, b) nanoparticle-based porous fibers with metal nanoparticles, c) nanoparticles surface-coated by adding a sol-gel precursor.....	53
Figure 3-14:	Scheme of fibers with surface-coated nanoparticles by adding of a sol-gel precursor: a,b) as-spun and c) after calcination	54
Figure 3-15:	Porous TiO ₂ Nanofibers prepared from nanoparticles of TiO ₂ (2 h at 110°C) and Pd (1.5 wt%): a) TEM and b) EDX analysis	55
Figure 3-16:	Digital photograph of a "textile" of PVP-ZIF-8 hybrid nanofibers.....	57
Figure 3-17:	SEM (left) and TEM (right) of PVP-ZIF-8 hybrid nanofibers	58
Figure 3-18:	XRD of pure ZIF-8 nanoparticles and ZIF-8 inside PVP or PS.....	58
Figure 3-19:	Nitrogen adsorption isotherms of ZIF-8 nanoparticles in PS and PVP (with different loadings of ZIF-8).....	59
Figure 3-20:	SEM of a) PS-ZIF-8 and b) PEO-ZIF-8 nanofibers.....	60

Figure 3-21: Adsorption kinetics studied as cell pressure over time	61
Figure 3-22: CO ₂ adsorption isotherms of ZIF-8 nanoparticles in PVP and ZIF-8 microparticles.....	62
Figure 3-23: CO ₂ adsorption kinetics of ZIF-8 nanoparticles in PVP and ZIF-8 microparticles.....	62
Figure 4-1: Comparison of RuO ₂ a) commercial nanopowder and b) nanotubes as-prepared with corresponding c) XRD and d) TEM	66
Figure 4-2: Comparison of RuO ₂ nanotubes a) as-prepared at 475°C, b) after NH ₃ oxidation at 673 K for 70 h, c) after HCl oxidation at 573 K for 5.5 h, d) yield in HCl oxidation as function of temperature	68
Figure 4-3: Coaxial electrospinning setup: A) scheme, C) TEM and D) SEM of hollow TiO ₂ nanotubes prepared from PVP/sol-gel precursor	69
Figure 4-4: Principle of emulsion electrospinning.....	70
Figure 4-5: Comparison (TEM) of RuO ₂ nanofiber after 1 h at a) 450°C and b) 250°C with the spinning polymer still present.....	70
Figure 4-6: Comparison of RuO ₂ electrospun from PVP a) at relative humidity of 40% and b) with 1 wt% H ₂ O.....	71
Figure 4-7: Comparison of RuO ₂ electrospun from a) PVB and b) PVP.....	72
Figure 4-8: Nanotubes of a) Co ₂ O ₃ and b) NiO obtained after calcination at 425°C from PVP and the corresponding DMF complexes	73
Figure 4-9: Nanotubes of Fe ₂ O ₃ from PVP-FeCl ₃ a) SEM and b) TEM.....	73
Figure 4-10: a) TEM and b) SEM images of nanotubes Fe ₂ O ₃ obtained after calcination at 425°C from PVP and the iron-DMF complex prepared from Fe(NO ₃) ₃ ·9H ₂ O	74
Figure 4-11: Evolution of Fe-PVP-DMF spinning solution after 1 day in a sealed vial (clear solution) when exposed to humid air (the left drop has been under air for 5 min).....	75
Figure 4-12: Morphology formation in hydrophobic PS electrospun at low humidity (a-d) leading to wrinkled fibers and nanoribbons, and at high humidity (e-f)	76
Figure 4-13: A drop of 10 wt% FeCl ₃ in EtOH and of 30 wt% FeCl ₃ in DMF: a) after dropping, b) after mixing and c) after addition of more EtOH or two drops of DMF and mixing.....	77
Figure 4-14: Chemical structures with delocalization for a) DMF and b) PVP.....	78
Figure 4-15: Proposed mechanism of tube formation: A homogeneous electrospinning jet dries and a solid Fe-PVP complex precipitates to stabilize the skin that later transforms into iron hydroxide and upon calcination to iron oxide.....	79

Figure 4-16: XRD of $\text{Ru}_x\text{Ti}_{1-x}\text{O}_2$ nanofibers after calcination at 475°C with JCPDS references for Rutile, Anatase and RuO_2	82
Figure 4-17: XRD of $\text{Ru}_{0.1}\text{Ti}_{0.9}\text{O}_2$ as fibers and dried after calcination at 475°C	83
Figure 4-18: Yield in HCl oxidation as function of temperature: Comparison of a) RuO_2 nanotubes and b) $\text{Ru}_{0.15}\text{Ti}_{0.85}\text{O}_2$ nanofibers	84
Figure 6-1: Circuit diagram of conductivity measurements in a) 2-point and b) 4-point mode	92
Figure 6-2: Digital image of the electrospinning setup	93
Figure 6-3: SEM images of nanofibers: a) IZO nanoparticles in PVP, b) after calcination at 550°C , c) with 5% ZnCl_2 and d) with 10% ZnCl_2	96
Figure 6-4: Basic setup of thin film deposition by spray pyrolysis	98

6.5 Tables

TABLE 2-1: COMPARISON OF VARIOUS TCO MATERIALS	18
TABLE 2-2: INFLUENCE OF PARTICLE CRYSTALLINITY ON CONDUCTIVITY OF FIBERS AND FILMS	22
TABLE 2-3: COMPARISON OF PHOTOELECTROCHEMICAL MEASUREMENTS:	25
TABLE 2-4: REFRACTIVE INDICES n_D (AT 589 NM AND 0°C)	29
TABLE 2-5: SPECIFIC RESISTIVITIES P AT 20°C	31
TABLE 3-1: SURFACE AREA (ACCORDING TO THE BET MODEL) FOR NANOPARTICLES AND THE RESULTING NANOFIBERS	46
TABLE 3-2: MODIFICATIONS OF TiO_2	49
TABLE 3-3: NH_3 TO NO_x CONVERSION AT 400°C FOR RUO_2 AND $RUO_2@TiO_2$ FIBERS	54
TABLE 3-4: NITROGEN ADSORPTION DATA	59
TABLE 4-1: RIETVELD ANALYSIS (AT%) OF $TiO_2:RU$ SYSTEMS AT 475°C	83
TABLE 6-1: SOLVENTS	88
TABLE 6-2: PRECURSORS	89
TABLE 6-3: POLYMERS	89
TABLE 6-4: COMPARISON OF TCO MATERIALS	99

6.6 Index

A	D
activity	Darcy's law 38
catalytic activity.. 34, 49, 50, 52, 53, 55, 65, 67, 68, 84, 86	Deacon process
adsorbate 58, 61, 91	HCl oxidation 67
adsorption kinetics 61, 109	DSSC
anatase 46, 49, 51, 55, 64, 81, 82, 83, 106	dye sensitized solar cell 10
ATO	dye sensitized solar cells 12, 14, 15, 27
antimony doped tin oxide 15, 18, 19, 20, 21, 23, 24, 25, 26, 27, 29, 31, 40, 41, 85, 86, 95, 96, 98, 99, 100, 102, 107	E
AZO	electrical conductivity 3, 28
aluminum zinc oxide 18	electrodeposition. 15, 23, 24, 25, 26, 34, 85, 98, 102, 107
B	electrospinning 5
band gap 2, 49, 99	exciton 49
BET	F
Brunauer-Emmett-Teller . 45, 46, 47, 55, 58, 59, 67, 91	fill factor 25, 26, 85
block copolymer templates 39, 55	FTO
bottom-up 4	fluorine doped tin oxide. 18, 24, 25, 26, 31, 94, 96, 98, 99, 102
C	H
carbon nanotubes 4, 28, 29, 31	hierarchical pore system 38
Catalysis 65	hollow nanotubes 8, 69, 73, 79, 86, 110
chemisorption 54	hydrothermal synthesis 61
circuit voltage 25	I
coaxial electrospinning 41, 69, 76	ITO
convection 38	indium tin oxide . 10, 12, 13, 14, 15, 17, 18, 19, 20, 23, 31, 49, 85, 94, 99, 100, 101, 102
counter electrode 92	IZO
crystal structure	indium zinc oxide 18, 96, 97
bixbyite 18	
cassiterite 20	
rutile 23	

- M**
- mesoporosity 38, 39
mesoporous TiO₂..... 14, 15, 49
MOF
 metal organic framework 56, 60, 63, 86
monolithic silica..... 37
- N**
- nanomaterials 1, 2
nanoscale architectures 2
nanotechnology 1
nanowires.1, 2, 3, 4, 10, 11, 12, 20, 28, 29, 30, 31, 32, 35,
 135
Niederberger
 Non-aqueous sol-gel process 43
- O**
- Ostwald process 53, 65
- P**
- PB
 Prussian Blue 23
percolation threshold..... 3, 28
Phase Separation..... 40
photocatalyst 49
physisorption..... 54, 91
PIB3000 14
PIM
 Polymer of Intrinsic Microporosity 56
pore volume 42
- R**
- refractive index 29
relative humidity 7, 71, 93, 94, 104, 107, 108, 113
Rietveld analysis 47, 67, 83
rutile 49, 64, 81, 82, 83, 84, 87
- S**
- selectivity
 catalytic selectivity 65
shear forces 69
short circuit photocurrent 25
sol-gel process 18, 38, 40, 41
solid skin
 fiber formation 8, 77
Solidification 40
stability
 deactivation in catalysis 65
Stoeber method
 Silica nanoparticles 44
surface tension 5, 7
- T**
- Taylor cone 5, 7, 69
TCO
 transparent conducting oxide 10, 11, 17, 18, 19, 22,
 28, 30, 85, 87, 92, 98, 99, 106
top-down 4, 5
transparency 28, 29, 30, 87, 99
- U**
- UV-C 50, 104, 105
- Y**
- YSZ
 Yttria-stabilized zirconia 35, 36
- Z**
- ZIF
 Zeolitic imidazolate framework.. 56, 57, 58, 59, 60, 61,
 63, 108, 109

6.7 Acknowledgements

This thesis would not have been possible without the help and assistance of many great people I have had the privilege of getting acquainted with.

In particular, I would like to thank my supervisor Prof. Smarsly for his support, his patience and many fruitful discussions.

Furthermore, I would like to express my gratitude to Prof. Over for suggesting to prepare RuO₂ nanofibers as model catalyst, helpful discussions and being reviewer of this thesis.

I would equally like to thank Prof. Janek for sharing his knowledge and expertise.

I am also indebted to Dr. Serafin and Dr. Rohnke for helping us to a good start at the JLU.

Moreover, I would like to thank all members of the groups of Prof. Smarsly, Prof. Over and Prof. Janek for their help. I am also indebted to the staff of the Institute of Physical Chemistry for their help in constructing and extending experimental setups.

Moreover, I would like to acknowledge the groups of Prof. Schlettwein (JLU Giessen) and Dr. Wiebcke (University of Hannover) for their collaboration.

Furthermore, I like to thank some special people:

- Bernd and Philipp for teaching me table soccer back at the MPI.
- Kirstin, Sébastien and Simone for the good start in Giessen.
- Henrik und Stefan for many sparring-matches at the table soccer and JP for helping me drive them mad!
- All table soccer players for many great matches.
- Christoph and Takeshi as co-midnight-workers and for many discussions on inorganic chemistry and HPLC, respectively.
- My office mates Claas, Till and Jan for the good times and answering the phone in the office and then trying to find me in the labs.
- Mr. Takeshi and Mr. Laem for sharing many evenings in the lab and trying to teach me Japanese and Thai – ARI-GA-TOU!
- All my students for working so hard in the lab.
- (in case I forgot somebody ;-)

I gratefully acknowledge the German National Merit Foundation for my PhD scholarship.

And last, but not least I would like to thank all my friends, but especially my great family and Henni for all the support and love that they have given me over the last years!

**Der Lebenslauf wurde aus der elektronischen
Version der Arbeit entfernt.**

**The curriculum vitae was removed from the
electronic version of the paper.**

Awards / scholarships

- 2009 DAAD (German academic exchange service) travel grant for the MRS Fall Meeting 2009 in Boston
- 2008 Carl-Ziegler travel grant of the German Chemical Society (GDCh) for Eu-CheMS Chemistry Congress
- 2007 3-year-PhD scholarship of the German Merit Foundation (Studienstiftung des Dt. Volkes)
- 2005 "Chemie-Preis 2005" of RWTH Aachen (best pre-diploma in chemistry)
- 2004 3-year-scholarship of Ecole Normale Supérieure (Sélection Internationale)
- 2004 scholarship of the German Merit Foundation (Studienstiftung des Dt. Volkes)
- 2002 scholarship from e-fellows.net
- 2001 Preis des Fonds der Chemischen Industrie für das beste Chemie-Abitur (best A-Levels in Chemistry)
- 1998, 2001 German contest for young scientists (jugend forscht): 1st place in Mathematics/Computer Science in the regional competition

Teaching

- 2010 Instructor at a summer school for talented high school students (Deutsche Schülerakademie)
- 2007- 2010 Teaching assistant in advanced lab courses in physical chemistry
Assistant lecturer in exercise courses (structure determination course), Supervisor of one diploma and three bachelor's theses
- 2002, 2003 Tutor in the pre-university chemistry course
- 1997-2001 Founding and supervising a High School Computer Club, Hemer

Research Experience/Internships

PhD (defense expected in 02/2011)

Justus-Liebig-University of Giessen, Germany (Prof. B.M.Smarsly)

“Design and physico-chemical characterization of nanowires and multicomponent metal oxide films with tailored mesostructure and crystallinity”

Master's thesis (2007)

Max-Planck-Institute for Colloids and Interfaces, Potsdam-Golm, Germany (Prof. M.Antonietti and Dr. B.M.Smarsly): “Mesoporous Metal Oxides Films for Electrochromic Applications”

Undergraduate Research

2006 CEA Grenoble with Prof. Fontcave and Dr. Artero: “Synthesis of structural and functional hydrogenase models ($[\text{Ni}(\text{xbsms})\text{RuCpCH}_3\text{CN}]^+$ and analogues)”

Saint-Gobain Recherche, Aubervilliers / Laboratoire de Chimie de Matière Condensée (Prof. Sanchez), Paris, France : “Mesoporous Alumina Coatings for SiO_2 fibers”

2005 University of Washington, Seattle, USA (Prof. Xia): “Electrospinning of metal oxides nanofibers”

Université Pierre et Marie Curie, Paris, France: 1-month internships with Prof. Jolivet and Prof. Che

2004 Procter & Gamble European Summer Internship at Egham/London, Great Britain

2-month-internship at cognis in Düsseldorf, Germany

Talks/Posters

- MRS conference, Boston, 02.12.2009 (talk)
- 21. Deutsche Zeolith Tagung (German Zeolith Conference), 5.-7.3.2009, in Kiel (talk)
- 2nd EuCheMS Chemistry Congress, 16.-20.9.2008, in Torino (poster)
- International GDCh Conference "Electrochemistry: Crossing Boundaries", 6.-8.10.2008, in Giessen (talk)
- 20. Deutsche Zeolith Tagung (German Zeolith Conference), 5.-7.3.2008, in Halle/Saale (talk and poster)
- 19. Deutsche Zeolith Tagung (German Zeolith Conference), 7.-9.3.2007, in Leipzig (poster)
-

6.9 List of Publications

- [1] R. Ostermann, D. Li, Y. Yin, J. T. McCann, Y. Xia:
'V₂O₅ Nanorods on TiO₂ Nanofibers: A New Class of Hierarchical Nanostructures Enabled by Electrospinning and Calcination', *Nano Letters*, vol. 6, no. 6, pp. 1297-1302, **2006**.
- [2] J. T. McCann, B. Lim, R. Ostermann, M. Rycenga, M. Marquez, Y. Xia:
'Carbon Nanotubes by Electrospinning with a Polyelectrolyte and Vapor Deposition Polymerization', *Nano Letters*, vol. 7, no. 8, pp. 2470-2474, **2007**.
- [3] S. Canaguier, L. Vaccaro, V. Artero, R. Ostermann, J. Pecaut, M. Field, M. Fontecave:
'Cyclopentadienyl Ruthenium-Nickel Catalysts for Biomimetic Hydrogen Evolution: Electrocatalytic Properties and Mechanistic DFT Studies', *Chemistry - A European Journal*, vol. 15, no. 37, pp. 9350-9364, **2009**.
- [4] R. Ostermann, S. Sallard, B. M. Smarsly:
'Mesoporous sandwiches: towards mesoporous multilayer films of crystalline metal oxides', *Physical Chemistry Chemical Physics*, vol. 11, no. 19, pp. 3648-3652, **2009**.
- [5] R. Ostermann, B. M. Smarsly:
'Does mesoporosity enhance thin film properties? A question of electrode material for electrochromism of WO₃', *Nanoscale*, vol. 1, no. 2, pp. 266-270, **2009**.
- [6] K. Brezesinski, R. Ostermann, P. Hartmann, J. Perlich, T. Brezesinski:
'Exceptional Photocatalytic Activity of Ordered Mesoporous β -Bi₂O₃ Thin Films and Electrospun Nanofiber Mats', *Chemistry of Materials*, vol. 22, no. 10, pp. 3079-3085, **2010**.

- [7] R. Ostermann, M. Rudolph, D. Schlettwein, B. M. Smarsly:
'Novel Nanostructured Photoelectrodes - Electrodeposition of metal oxides onto transparent conducting oxide nanofibers', *Mater. Res. Soc. Symp. Proc.*, vol. 1211, pp. R07-03, **2010**.
- [8] C. Wessel, L. Zhao, S. Urban, R. Ostermann, I. Djerj, B. M. Smarsly, L. Chen, Y.S. Hu, S. Sallard:
'Ionic-Liquid Synthesis Route of TiO₂(B) Nanoparticles for Functionalized Materials', *Chemistry - A European Journal*, vol. 17, no. 3, pp. 775-779, **2011**.
- [9] C. Wessel, R. Ostermann, R. Dersch, B. M. Smarsly:
'Formation of Inorganic Nanofibers from Preformed TiO₂ Nanoparticles via Electrospinning', *The Journal of Physical Chemistry C*, vol. 115, no. 2, pp. 362-372, **2011**.
- [10] R. Ostermann, J. Cravillon, C. Weidmann, M. Wiebcke, B. M. Smarsly:
'Metal-organic framework nanofibers', *Chemical Communications*, vol. 47, no. 1, p. 442, **2011**.
- [11] J.P. Hofmann, R. Ostermann, F. Hess, C.H. Kanzler, B. M. Smarsly, H. Over:
'Novel oxide nanofibers for heterogeneous model catalysis', in preparation, **2011**.

Patents

- [1] R. Ostermann, B. M. Smarsly, R. Zieba, A. Traut, F. Major, E. Klimov, L. Pottie: "Verfahren zur Herstellung von Nanofasern", EP 09 175 023.2, **2009**